# Fracture in porous media: phase-field modeling, simulation and experimental validation

Von der
Fakultät Architektur, Bauingenieurwesen und Umweltwissenschaften
der Technischen Universität Carolo-Wilhelmina
zu Braunschweig

zur Erlangung des Grades einer
**Doktor-Ingenieurin (Dr.-Ing.)**
genehmigte

**Dissertation**

von
Tuanny Cajuhi
geboren am 22.10.1989
aus Recife

Eingereicht am: 5. Dezember 2018
Disputation am: 17. Januar 2019

Berichterstatter: Prof. Dr.-Ing. Laura De Lorenzis
Prof. Dr.-Ing. Pietro Lura

2019

*"Contrary to what most people think, making a decision is one of the easiest decisions in the world, as is more than proved by the fact that we make decision upon decision throughout the day, there, however, we run straight into the heart of the matter, for these decisions always come to us afterward with their particular little problems, or, to make ourselves quite clear, with their rough edges needing to be smoothed, the first of these problems being our capacity for sticking to a decision and the second our willingness to follow it through."*

José Saramago, The double

# Kurzfassung

Poröse Medien finden sich in vielen technisch relevanten Materialien wie Schaum- und Zementverbunden sowie in biologischen Geweben wieder. Durch ihre Interaktion von festen und fluiden Phasen sind sie von äußerst komplexer Natur. Diese Wechselwirkung kann durch chemische Reaktionen oder durch Austrocknen geschehen, z.B. während der Härtung von zementartigen Materialien, wenn eine feste Matrix gebildet wird und sich verformt. Risse in porösen Medien bilden sich meistens aufgrund von inneren Heterogenitäten, Selbst- oder Fremdeinschränkungen die eine freie Verformung des Mediums verhindern. Darüber hinaus treten sie auch aufgrund kurz- und langfristiger Austrocknung auf, die durch Volumenänderung verursacht werden. Dieser Prozess ist in der Literatur unter *Schwinden* bekannt. In jungen zementartigen Materialien können diese die Haltbarkeit einer Konstruktion beeinträchtigen. Ziel dieser Arbeit ist es, ein numerisches Model zu entwickeln, das schwindungsinduzierte Risse in porösen Materialien vorhersagen kann. In dieser Arbeit werden poröse Medien in makroskopischer Skala betrachtet, d.h. Poren und Heterogenitäten werden nicht explizit modelliert und stattdessen werden homogenisierte Eigenschaften berücksichtigt. Das poromechanische Modell basiert auf dem effektiven Spannungskonzept. Die Modellierung der Rissbildung geschieht durch ein Phasenfeldmodell des Sprödbruchs. Das Phasenfeld ist über die effektive Spannung und durch die von hydraulischen Variablen abhängige Bruchenergie gekoppelt. Das entwickelte mathematische Modell wird mit der Finite-Elemente-Methode unter Verwendung des TaylorHood-Elementpaares diskretisiert und in der `deal.II`-Bibliothek implementiert. Die *erste Anwendung* des Frameworks befasst sich mit dem Austrocknungsphänomen in Böden. Ein Tonblock wird in verschiedenen Konfigurationen in der 2D-Einstellung getrocknet. Dabei wir eine Sensitivitätsanalyse mit Bezug auf die Variation der Eingangsgrößen durchgeführt. Die numerischen Ergebnisse zeigen eine sehr gute Übereinstimmung mit den Experimenten. Des Weiteren werden die numerischen Aspekte und die Erweiterung der 3D-Einstellung untersucht. Der *zweite Teil* der Arbeit befasst sich mit Rissbildung, die durch Trocknungsschrumpfung in Zementmörtel induziert wird. Um geeignete Eingabedaten für die Kalibrierung des Frameworks zu erhalten und seine unabhängige Validierung zu verfolgen, wird eine Reihe von Experimenten durchgeführt. Die Kalibrierungstests umfassen sowohl mechanische als auch poromechanische Tests, die darauf abzielen, Materialeigenschaften und Randbedingungen zu liefern, wie z.B. Masseverlust (Fluss) Daten für schwindungsinduzierte Rissbildungssimulationen. Zur unabhängigen Validierung werden die Ringtests durchgeführt. Dabei wurde eine gute Übereinstimmung zwischen rechnerischen und experimentellen Ergebnissen gefunden.

# Abstract

Porous media are found in many engineering-relevant materials such as foam and cementitious composites, as well as in biological tissues. They present a complex nature, being composed of both solid and fluid phases, which interact with each other. This interaction can be caused by chemical reactions or due to drying, e.g. during hardening of cement-based materials when the solid matrix is formed and deforms. The presence of inner heterogeneities, self or external restraints prevents the free deformation of the medium and might lead to cracking. Cracks induced by change of volume, or shrinkage, occur due to short- and long-term drying. In cementitious materials at early ages, these can compromise the durability of the construction. Aim of this thesis is to develop a numerical framework able to predict shrinkage-induced cracking in porous materials. In this work, porous media are modeled at the macroscopic scale, in other words pores and heterogeneities are not modeled explicitly and average properties are taken into account instead. The poromechanical framework is based on the effective stress concept. A phase-field model of brittle fracture is utilized to model cracking and coupled to the poromechanical part through the effective stress and through an expression of the fracture energy depending on hydraulic variables. The developed mathematical framework is discretized with the finite element method using the Taylor-Hood element pair and implemented within the `deal.II` library. The *first application* of the framework deals with the desiccation phenomenon in soils. A block of clay is subjected to drying at different configurations in a 2D setting. A sensitivity analysis of the problem with respect to the variation of input quantities is performed. The obtained behavior compares very well with the experimentally observed one. Numerical aspects and the extension to the 3D setting are also investigated. The *second application* deals with cracking induced by drying shrinkage in cementitious mortar. In order to obtain the most appropriate input data for the calibration of the framework and to pursue its independent validation, a set of original experiments is performed. The calibration tests encompass mechanical as well as poromechanical tests, which aim at providing material properties and boundary conditions such as mass loss (flux) data for shrinkage-induced cracking simulations. For independent validation, ring tests are performed. A good agreement between computational and experimental results is found.

# Acknowledgements

This research was performed between October 2015 and September 2018 and made possible by the German Research Foundation (DFG) with the project "Modeling the constitutive evolution of building materials and structures with respect to aging" (GRK-2075). The research has been carried out at the Institute of Applied Mechanics, Technische Universität Braunschweig.

I would like to express my sincere gratitude to my advisor, Prof. Dr.-Ing. Laura De Lorenzis, for the continuous support of my research. The importance she always gives into the detailed theoretical understanding has always inspired me as a young researcher. Thanks for mentoring me and giving me the chance to work with you. Undoubtedly, it helped me learn many things which I am sure will help me in my future endeavors.

I would also like to thank Prof. Dr.-Ing. Pietro Lura, who gave me access to his research facility, also for the intense discussions and motivation during the research. His enthusiasm and passion towards research are simply contagious.

I would like to acknowledge Prof. Dr.-Ing. Manfred Krafczyk and Prof. Dr.-Ing Dinkler for the productive discussions during my research and also for being members of my dissertation committee.

Many thanks to the great and fruitful discussions with Prof. Lorenzo Sanavia and the colleagues at the University of Padova.

One acknowledgments session would not be enough to express how grateful I am to everyone I was able to meet and work together during this time period. Special thanks are given to all my colleagues at the institute for their time and valuable suggestions that helped me tackle problems ranging from hardware management to theoretical understanding. The help from the team at the Swiss Federal Laboratories for Materials Science and Technology during the experimental phase of my work is unforgettable. To mention, the support I received from Dr. Mateusz Wyrzykowski and Dr. Michele Griffa. *Paldies* Nikolajs Toropovs and Janis Justs for helping me to gain insight into the experimental study.

Last but not least, thanks to my family and friends for the motivation and patience during this time.

Braunschweig, December 2018 Tuanny Cajuhi

# Contents

# List of figures

# List of tables

# List of symbols

| | | |
|---|---|---|
| | **Greek symbols** | |
| $\alpha$ | Biot parameter | - |
| $\alpha_{vG}$ | van Genuchten parameter | $\mathrm{m}^{-1}$ |
| $\gamma$ | crack energy density | $\mathrm{N\,m}^{-1}$ |
| $\Gamma$ | boundary of domain $\Omega$ | - |
| $\Gamma_0$ | boundary of domain $\Omega_0$ | - |
| $\Gamma_c, \Gamma_u, \Gamma_p$ | Dirichlet portions of the boundary | - |
| $\Gamma_d, \Gamma_q, \Gamma_t$ | Neumann portions of the boundary | - |
| $\gamma_w$ | specific gravity | $\mathrm{N\,m}^{-3}$ |
| $\boldsymbol{\varepsilon}$ | strain tensor | - |
| $\boldsymbol{\varepsilon}^{dev}$ | deviatoric part of strain tensor | - |
| $\ell$ | length scale parameter | m |
| $\varepsilon_{hom}$ | homogeneous solution | - |
| $\eta$ | residual stiffness | - |
| $\lambda$ | Lamé constant | $\mathrm{N\,m}^{-2}$ |
| $\mu_w$ | dynamic viscosity | $\mathrm{Pa\,s}$ |
| $\nu$ | Poisson's ratio | - |
| $\rho$ | average density | $\mathrm{kg\,m}^{-3}$ |
| $\rho_d$ | dry or bulk density | $\mathrm{kg\,m}^{-3}$ |
| $\rho_s$ | solid density | $\mathrm{kg\,m}^{-3}$ |
| $\rho_w$ | water density | $\mathrm{kg\,m}^{-3}$ |
| $\boldsymbol{\sigma}$ | total Cauchy stress | $\mathrm{N\,m}^{-2}$ |
| $\boldsymbol{\sigma}'$ | generalized effective stress | $\mathrm{N\,m}^{-2}$ |
| $\sigma'_{hom}$ | homogeneous solution stress | $\mathrm{N\,m}^{-2}$ |
| $\sigma_t$ | tensile strength | $\mathrm{N\,m}^{-2}$ |
| $\sigma_\theta$ | circumferential stress | $\mathrm{N\,m}^{-2}$ |
| $\tau$ | instant | s |
| $\varphi$ | pressure head | m |
| $\boldsymbol{\phi}^d, \boldsymbol{\phi}^p, \boldsymbol{\phi}^u$ | shape functions | - |
| $\chi_w$ | contact area of the liquid water | - |
| $\Psi$ | elastic energy | $\mathrm{N\,m}^{-1}$ |
| $\Psi^+$ | active part of the elastic energy | $\mathrm{N\,m}^{-1}$ |
| $\Psi^-$ | non-active part of the elastic energy | $\mathrm{N\,m}^{-1}$ |
| $\Omega$ | arbitrary domain (deformed configuration) | - |
| $\Omega^h$ | discretized domain (deformed configuration) | - |
| $\Omega_0$ | arbitrary domain (undeformed configuration) | - |
| $\Omega_0^h$ | discretized domain (undeformed configuration) | - |
| $\Omega_0^e$ | element domain (undeformed configuration) | - |

| | **Roman symbols** | |
|---|---|---|
| $A$ | surface area | $\mathrm{m}^2$ |
| $a, b, c, d$ | fitting parameters of double exponential function | - |
| $C_s$ | moisture content | $\mathrm{N}^{-1}\,\mathrm{m}^2$ |
| $d$ | phase-field variable | - |
| $\hat{d}$ | nodal phase-field variable | - |
| $\hat{d}^h$ | discretized phase-field variable | - |
| $\mathcal{D}$ | constitutive tensor | $\mathrm{N\,m}^{-2}$ |
| $\mathcal{D}^+$ | positive part of the constitutive tensor | $\mathrm{N\,m}^{-2}$ |
| $\mathcal{D}^-$ | negative part of the constitutive tensor | $\mathrm{N\,m}^{-2}$ |
| $E$ | Young's modulus | $\mathrm{N\,m}^{-2}$ |
| $\mathrm{E}(\mathbf{u}, \Gamma)$ | energy functional | $\mathrm{N\,m}$ |
| $\mathrm{E}_{ell}$ | regularized energy functional | $\mathrm{N\,m}$ |
| $\mathbf{F}_{ext}$ | external forces | $\mathrm{N}$ |
| $\mathbf{F}_{int}$ | internal forces | $\mathrm{N}$ |
| $g$ | magnitude of the gravity vector $\mathbf{g}$ | $\mathrm{m\,s}^{-2}$ |
| $G$ | Lamé constant | $\mathrm{N\,m}^{-2}$ |
| $\mathcal{G}_c$ | fracture energy | $\mathrm{N\,m}^{-1}$ |
| $h$ | mesh size | $\mathrm{m}$ |
| $\mathcal{H}$ | energy history | $\mathrm{N\,m}$ |
| $H \times B \times L$ | height times width times length | $\mathrm{m}^3$ |
| $_i$ | iteration (superscript) | - |
| $_K$ | node index (subscript) | - |
| $k_i$ | intrinsic permeability | $\mathrm{m}^2$ |
| $k_{rw}$ | relative permeability | - |
| $k_w$ | hydraulic conductivity | $\mathrm{m\,s}^{-1}$ |
| $\mathbf{g}$ | gravity acceleration vector | $\mathrm{m\,s}^{-2}$ |
| $K_s$ | bulk modulus of solid phase | $\mathrm{N\,m}^{-2}$ |
| $K_T$ | average bulk modulus of the solid skeleton | $\mathrm{N\,m}^{-2}$ |
| $K_w$ | bulk modulus of water | $\mathrm{N\,m}^{-2}$ |
| $m_{dw}$ | mass of displaced water | $\mathrm{kg}$ |
| $m_{vG}$ | van Genuchten parameter | - |
| $^n$ | time step (superscript) | - |
| $n$ | porosity | - |
| $\mathbf{n}$ | outward normal vector | - |
| $n_e$ | number of elements | - |
| $p$ | average pressure | $\mathrm{N\,m}^{-2}$ |
| $p_a$ | air pressure | $\mathrm{N\,m}^{-2}$ |
| $p_c$ | capillary pressure or matric suction | $\mathrm{N\,m}^{-2}$ |
| $p_w$ | pore water pressure | $\mathrm{N\,m}^{-2}$ |
| $\bar{p}_w$ | pore water pressure (boundary) | $\mathrm{N\,m}^{-2}$ |
| $\hat{p}_w$ | nodal pore water pressure | $\mathrm{N\,m}^{-2}$ |
| $\hat{p}_w^h$ | discretized pore water pressure | $\mathrm{N\,m}^{-2}$ |

| | | |
|---|---|---|
| $p_{w_0}$ | initial value of the pore water pressure | $\mathrm{N\,m^{-2}}$ |
| $p_r w$ | relative pore water pressure | $\mathrm{N\,m^{-2}}$ |
| $\bar{q}$ | imposed flux | $\mathrm{m\,s^{-1}}$ |
| $\mathbf{R}, \Delta\mathbf{R}$ | residual, linearized residual | N |
| $S_e$ | effective saturation | - |
| $S_i$ | volume fraction (saturation of each phase $i$) | - |
| $S_r$ | residual saturation | - |
| $S_w$ | water degree of saturation | - |
| $t, \Delta t$ | time, time increment | s |
| $\bar{t}$ | imposed traction | N |
| $\mathbf{u}$ | displacement | m |
| $\bar{\mathbf{u}}$ | displacement (boundary) | m |
| $\hat{\mathbf{u}}$ | nodal displacement | m |
| $\hat{\mathbf{u}}^h$ | discretized displacement | m |
| $\mathbf{u}_0$ | initial value of the displacement | m |
| $\mathbf{U}$ | global solution vector | - |
| $V$ | bulk volume | $\mathrm{m^3}$ |
| $V_{dw}$ | volume of displaced water | $\mathrm{m^3}$ |
| $V_v$ | volume of pores | $\mathrm{m^3}$ |
| $\mathbf{v}_{ws}$ | relative velocity | $\mathrm{N\,s^{-1}}$ |
| $w$ | water content | % |
| $\mathbf{w}^u, w^p, w^d$ | test functions | - |

**Mathematical operators**

| | |
|---|---|
| $\Delta$ | Laplacian |
| $\nabla\cdot$ | divergence |
| $\nabla^s$ | symmetric gradient |
| tr | trace |
| $< x >_{\pm}$ | $0.5(x \pm \lvert x \rvert)$ |

# List of abbreviations

| | |
|---|---|
| **CTT** | **C**ompact **T**ension **T**est |
| **DIC** | **D**igital **I**mage **C**orrelation |
| **exp** | **exp**erimental |
| **FEM** | **F**inite **E**lement **M**ethod |
| **RH** | **R**elative **H**umidity |
| **num** | **num**erical |

# Part I

# Prologue

# Chapter 1

# Introduction

## 1.1 Motivation

Porous materials find applications in several areas such as environmental geomechanics, civil engineering and biomechanics. Wood, soils, cementitious materials, bones and brain tissues are examples of porous media. The multiphase nature is a common attribute of these materials. They are composed of solid and fluid phases, e.g. air, water vapor, liquid water, etc., which must be in equilibrium with each other. A perturbation of this equilibrium, e.g. when the porous medium loses fluid mass, induces the evolution of moisture gradients. These may create volumetric changes that may lead to crack initiation and evolution when the material is restrained. The restraint of the medium occurs due to the bulk material and to internal restraints such as heterogeneities. Additional, external restraints may also be present, e.g. when dealing with cementitious materials connected to other structural elements or the subgrade. The phenomenon of cracking induced by the change of volume, i.e. *shrinkage*, happens in short- and long-terms and it is extremely relevant when studying the durability of these materials. A better understanding along with the modeling of this type of phenomena can help in the prediction of shrinkage-induced cracks.

## 1.2 Scope and research relevance

The scope of this thesis is the modeling of the coupled phenomena of drying, shrinkage and cracking. Main aims of this work are to (i) mathematically model shrinkage-induced cracking, (ii) develop a suitable numerical framework for the mathematical model, (iii) verify the numerical framework and (iv) calibrate and validate the computational approach with the help of a set of experiments specially designed to feed the input variables and boundary conditions of the framework.

To the best of the author's knowledge, the macroscopic framework developed in this thesis for porous media in general and accounting for variable saturation and cracking has not been reported in the literature before.

The modeling approach based on the phase-field model for brittle fracture, which enables modeling of both crack initiation and propagation within a variational framework without ad-hoc criteria, is coupled to the equations and constitutive laws of porous media mechanics. Furthermore, the framework accounts for the dependency of the elastic properties on hydraulic variables such as the water content.

To highlight the generality of the framework, two materials are tested: a clay-based soil and a cement-based mortar. We thus show that both environmental issues such as desiccation in soils and engineering problems such as shrinkage in cementitious materials can be analyzed with the numerical framework proposed in this thesis.

## 1.3 Outline

The fundamentals of porous media mechanics and cracking phenomenology as well as the related mathematical models reported in the literature are explained and reviewed in Chapter 2. Furthermore, a state of the art review on the mathematical modeling of deformation, drying and cracking processes in porous media and the coupling between them is also reported.

In Chapter 3, the governing equations for modeling shrinkage-induced cracking are derived. First, the general principles for modeling based on continuum mechanics theory are presented. Then the governing equations for porous media mechanics and the phase-field approach for brittle fracture are derived and the coupling between the fields is discussed.

The detailed numerical treatment of the nonlinear, time-dependent problem is discussed in Chapter 4. An outline for the spatial and temporal discretization is shown. The weak form of each equation as well as specific derivations, e.g. derivatives of the hydraulic properties, are reported. Moreover, the algorithmic procedure to solve the coupled problem is discussed.

The first application of the framework and its verification is related to the desiccation of soils in Chapter 5. Compacted clay is the material used for this study. The input data for the numerical tests are obtained from the literature and applied in the two- and three-dimensional setting. Furthermore, the influence of the type of finite element discretization on the numerical solution is analyzed and a sensitivity study with respect to the material properties and boundary conditions is carried out.

For the second application, a cement-based mortar is considered. In order to obtain the necessary original data for the validation of the framework, experiments are carried out. First, we start with the calibration of the mechanical and hygral properties of the

porous material, i.e. with elastic properties, drying and free shrinkage measurements, as discussed in Chapter 6. The second part of the calibration is related to the fracture properties by means of the compact tension test and discussed in Chapter 7. The fracture energy and the length scale parameter are the main variables to calibrate in the phase-field model. The coupled phenomena and cracking risk are studied with the restrained ring test in Chapter 8. In this chapter, the experimental parameters either obtained directly from the set of experiments or calibrated with the numerical model are used for validation of the framework.

Finally, conclusions regarding the numerical formulation, its capabilities and limitations are drawn in Chapter 9. Furthermore, ideas for future work are discussed.

# Chapter 2

# State of the art

This chapter provides a detailed literature review on the fundamentals of the coupled problem of drying, shrinkage and cracking. Furthermore, strategies for the numerical modeling of porous media mechanics and cracking in solids with particular focus on porous media are summarized.

## 2.1 Mechanics of porous media

Porous media are materials formed by a solid skeleton and pores (voids) [41]. They comprise soils, cementitious materials, biological tissues, and many others. In such media, the voids can be filled with fluids such as air, water, oil, etc. and can form an interconnected path through which the fluid can flow.

The behavior of the medium results from the interaction between the fluid and solid phases, e.g. the fluid flow results in moisture gradients that can cause deformation of the solid phase, or the application of a force on the solid matrix can lead to fluid movement. In this work, since we limit ourselves to elastic constitutive behavior, the terms *poromechanics* and *poroelasticity* are interchangeable and denote the coupled problem of deformation and fluid flow in elastic porous media.

Poromechanical phenomena can be described and modeled in different time and spatial scales ranging from the nano- to the macroscale. In pore scale modeling, the pore network is modeled explicitly and flow is studied in detail [27, 162]. This type of modeling approach is used to obtain intrinsic properties that can be later homogenized into effective properties in the macroscopic scale. Macroscopic modeling is commonly used for engineering problems. In this context, continuum mechanics concepts can be used [41].

Terzaghi [148] proposed the concept of *effective stress* in order to express the intrinsic relationship between the solid and fluid phase. This theory was first developed for soils

to describe consolidation problems with application to the foundation of buildings. The modeling addressed the one-dimensional flow and deformation in a *fully saturated* soil, i.e. when the liquid phase ideally occupies the whole pore space [43]. The main idea is that the effective stress balances the total stress and the pore pressure, and can be calculated by a stress-strain (constitutive) relationship.

The theory was further extended by Bishop [19, 20] to account for *partially saturated* conditions. In this context, the hygric macroscopic properties of the medium are expressed as functions of the properties of the fluid phases present in the medium and their respective *saturation degrees*, which quantify the relative amount of each fluid in the porous material, namely their volume fractions $S_i$. Obviously it must be

$$\sum_i S_i = 1,$$

where $i$ denotes the fluid phase, e.g. liquid water $w$, air $a$, oil $o$, and $S_i$ the corresponding degree of saturation. In this thesis, a fully water saturated medium corresponds to $S_w = 1$, i.e. only the water phase is present and ideally occupies (saturates) the whole pore space. The concept of partial or *variable saturation* can be explained by considering an arbitrary domain, e.g. a dam as seen in Fig. 2.1. The wet side of the dam is fully saturated, i.e. the degree of saturation $S_w = 1$ and the water pressure is positive, i.e. compressive. Since in reality there are always more than one phase (liquid, gas) in the pore space, the full degree of saturation is a mathematical idealization to express that the water phase is interconnected and the most present in the pore space. On the free side of the dam, i.e. the side exposed to air, the water fluid phase does not occupy the whole pore space and capillary pressure (or suction) develops. This phenomenon is represented by a variable degree of saturation and a negative water pore pressure, $S_w < 1$ and $p_w < 0$, respectively.

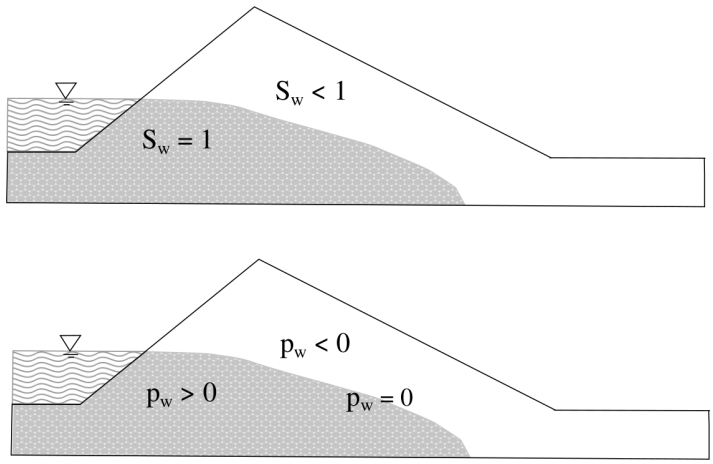


**Figure 2.1:** The pore space near the wet side is ideally interconnected and saturated with liquid phase, i.e. the medium is fully saturated ($S_w = 1$) and the water pressure is positive ($p_w > 0$). On the free side, more phases such as water vapor and liquid water can be present and the degree of saturation changes ($S_w < 1$) inducing the development of capillary pressure ($p_w < 0$).

In the context of variable saturation, the removal of pore fluid from the pore space happens due to environmental changes, e.g. during drying of paint layers, soil dessication and maturing of cement-based materials. These phenomena can lead to changes in the overall bulk volume of the medium [65, 121, 87, 21].

## 2.2 Volume changes and cracking

Due to the multiphase nature of porous media, pore fluid redistribution induces a variation of strains in the solid matrix according to the theory of effective stress [148]. Fluid redistribution is caused e.g. by chemical reactions, wetting, environmental changes, differences in humidity between the ambient and the porous medium. When the fluid is redistributed, changes in the overall volume of the material occur, which is termed *shrinkage* (in case of volume reduction).

In cementitious materials, shrinkage is especially relevant during the early maturing stages [95] when cement hydration, i.e. chemical reactions and binding of water to form hydration products, induces internal, uniform drying. This type of shrinkage is called *autogenous shrinkage*. The deformation of the solid matrix caused by this type of shrinkage is negligible in common mixtures, but needs to be considered in high performance concrete, i.e. concrete with low water-to-cement ratio which self-desiccates due to the low amount of water and fine pore structure [78].

In addition to the internal moisture loss caused by autogenous shrinkage, external moisture loss may also occur. The latter is relevant for all types of concrete mixtures and also for other geomaterials such as soils. Moreover, autogenous deformation is typically very fast, reaching equilibrium in a few weeks or a couple of months at most, while moisture loss to the ambient occurs more slowly and can last for several months or years. The phenomenon of volume change caused by external moisture loss is called *drying shrinkage*. When it occurs, moisture gradients are formed in the medium leading to the development of eigenstresses [21]. Since in this work autogenous shrinkage is not accounted for, the general term *shrinkage* is used to indicate drying shrinkage.

If the medium is able to contract freely, *free shrinkage* occurs. This type of shrinkage denotes unrestrained volume changes, such as in soil curling or simply supported free shrinkage and mass loss experiments in cementitious materials [85, 49].

On the other hand, volume changes are commonly restrained, indicating *restrained shrinkage*. When gradients in moisture content and in shrinkage within the material occur, a part of the specimen resists the contraction of the rest, i.e. acts as *self-restraint*. Additional to that, *internal restraints* may be present in heterogeneous materials such as concrete. Here, the aggregates hinder the free volume change of the medium.

Apart from the self- and internal restraints, a material is never completely free to shrink in reality due to e.g. the existence of friction between the medium and the supports. This indicates the presence of *external restraints*, which are not only caused

by friction but also imposed externally as volumetric limitations, e.g. the vegetation in soils, steel reinforcement bars in reinforced concrete, joints and supports utilized in civil engineering constructions and many others.

During shrinkage, the existing restraints can induce cracking since the medium cannot deform freely and fully release elastic energy. In soils, cracking induced by drying shrinkage is denoted as *desiccation*. Cracks at early-ages in cementitious materials corroborate the importance of the study of shrinkage-induced cracking. These can affect the aesthetics, but especially the durability as they facilitate the transport of harmful chemical substances such as chloride and sulfate ions into the medium. An overview of the factors that might reduce or increase the development of microcracks in common concrete mixtures caused by shrinkage can be found in [21, 23, 22, 24, 77].

Figures 2.2 and 2.3 show two examples of cracking due to shrinkage in a clay-based material and a cementitious material, respectively. In Fig. 2.2, clay is utilized as covering layer on the brick wall, which represents the base and restraint of the coating material. In Fig. 2.3, a cement-based material is utilized in the construction of a barrier. In both cases, environmental changes, e.g. differences in relative humidity and weather change, induce drying of the porous material.

A polygonal crack pattern can be observed on large surfaces exposed to drying. Polygonal patterns are also reported in the literature and are common during drying of thin layers such as after painting [65] and soil desiccation [139, 121, 88]. These cracks propagate perpendicular to the drying surface, along the thickness of the samples.

**Figure 2.2:** House covered with clay layer and subjected to environmental changes such as wetting due to rain, and drying, resulting in polygonal desiccation crack pattern (Photo by T. Cajuhi, Chapada Diamantina, Brazil, 2017).

**Figure 2.3:** Cracks on a concrete barrier subjected to environmental changes, e.g. differences in temperature and relative humidity shrinkage. A polygonal crack pattern is obtained at the upper surface. The cracks propagate perpendicular to the main (larger) drying surface (Photo by T. Cajuhi, Berlin, Germany, 2017).

A schematic representation of cracking due to external restraint is shown in Fig. 2.4. In this example, a block composed of porous material is mechanically restrained at the bottom and fluid is lost through the lateral and upper surfaces.

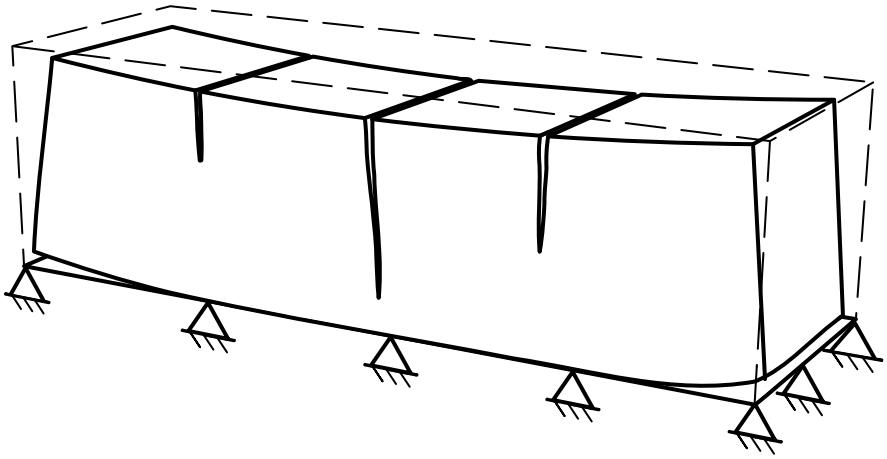

**Figure 2.4:** Schematic representation of a block composed of porous material and subject to drying shrinkage.

In contrast to the polygonal pattern, the cracks due to drying in the example shown in Fig. 2.4 are parallel to each other and perpendicular to the upper drying surface. This pattern was observed experimentally in soils and cement-based materials as reported in [121, 21]. Parallel cracks occur when the dimension of the specimen in the longitudinal direction is much larger than in its other dimensions. The shrinkage-induced cracks

with external restraint may occur throughout the specimen, while internal restraints induce comparably smaller, random cracks [95, 97, 21].

The susceptibility of crack formation as a function of the moisture content is described by Péron [121], who classifies three domains for the degree of saturation of liquid water. The first domain corresponds to full saturation $S_w = 1$, where cracking is unlikely to occur. With the increase of suction and, consequently, a reduction of the saturation, $S_w \approx 1$, the medium is close to the air entry conditions and more susceptible to cracking. The third saturation domain corresponds to lower water saturation degrees at which the air phase is connected.

The investigation of the mechanisms leading to cracking, in particular drying shrinkage, will ultimately lead to a better control of this phenomenon in porous media, especially in soils and cement-based materials.

## 2.3 Modeling strategies

In this section, the mathematical modeling strategies for the isolated problems of poromechanics and cracking are described. Furthermore, an overview of the modeling approaches for the coupled problem of poromechanics and cracking is presented.

### 2.3.1 Poroelasticity

The poromechanical theory is widely used in the modeling of coupled deformation in porous media [41, 168]. This theory is based on the principles of continuum mechanics and its main idea is to superimpose the fluid and solid continua, which form the porous medium, Fig. 2.5. This theory is related to the mixture theory extended with the concept of volume fraction, where the average properties of the porous medium are taken into account, e.g. average density, effective stress and average pressure [168].

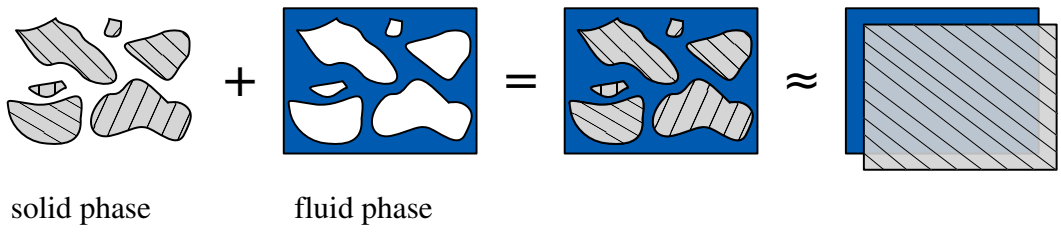


**Figure 2.5:** Continuum mechanics representation of a porous medium. The fluid and solid continua are superimposed and constitute the porous continuum. Its approximation represents the porous solid, described by the average properties of each phase.

In poroelasticity, small reversible deformations of the porous solid are accounted for.

The simplest strategy is similar to a thermomechanical analysis, which was the basis of Terzaghi's work when tackling the consolidation problem [148, 43]. In this approach, the equilibrium equation of the solid phase and the diffusion equation (analogous to the heat equation) are utilized in the modeling of the porous medium. This approach is adopted in recent works, see [144, 142] and references therein. However, this theory has some limitations since it highly idealizes the coupled problem of flow and deformation by considering the deformation only dependent on (and proportional to) the coefficient of diffusion. Furthermore, full degree of saturation is considered.

In order to account for the variation of saturation, poroelastic models are extended, e.g. in [168, 131, 58, 59, 60]. This extension considers the presence of more than one pore fluid phase whose volume fractions vary. For this reason, the balance equations of each fluid phase should be explicitly written. It is worth mentioning that the general poromechanical theory is also known as *theory of porous media* and includes infinitesimal and finite deformations, plasticity, viscoelasticity and thermoelasticity in porous media [41].

The poromechanical theory in the context of variable saturation is further referred to in the current work. A detailed explanation and derivation of the theory is given in Chapter 3.

### 2.3.2 Cracking

Several fracture models have been proposed in the literature. An overview of the most representative strategies in continuum mechanics is provided in the current section. Linear elastic fracture mechanics is concerned with the modeling of crack propagation. In this approach, a flaw, or initial crack, is assumed to be inherent to the material. One of the pioneers of this theory was Griffith [68]. According to Griffith's theory, pre-existing cracks are able to propagate if the energy release rate reaches a critical value.

In discrete modeling approaches, cracks are modeled as a discontinuity. Numerical strategies such as the extended finite element method [120] enrich the description of the displacement field in order to model crack propagation. Furthermore, cohesive zone methods [119] specify an additional constitutive relationship for the cohesive surfaces.

On the other hand, the so called regularized models smear the crack instead of modeling it explicitly. Examples in this context are local and non-local damage mechanics models [79], gradient damage models [125] and thick-level set approaches [109, 18] which prevent spurious localization due to the explicit separation between damaged and undamaged material expressed by a level set. Phase-field models for fracture are part of the family of gradient models and overcome the issue of widening of the crack band width present in gradient enhanced models [45].

The phase-field approach to fracture, which started with the pioneering work of [56] on

the variational formulation of the fracture problem and with its regularized counterpart [31], is recently gaining a lot of attention, see [7] for a review. Its main advantage is the possibility of modeling arbitrarily complicated crack patterns through the solution of partial differential equations. Phase-field models have a variational structure and do not need ad hoc criteria for topological changes in the crack pattern (branching or merging). The state of the material is characterized by the *crack phase-field* (or simply *phase-field*) with values ranging from 0 (intact material) to 1 (fully damaged material). A discrete crack is replaced by the steep variation of the phase-field from 0 to 1 with a characteristic width of the transition zone. The differences in the crack topology among sharp and diffusive models are depicted in Fig. 2.6 for a one-dimensional bar loaded at its ends and cracked at its center. While the sharp crack represents a discontinuity in the medium, the diffusive crack is a smeared representation which does not introduce singularities.

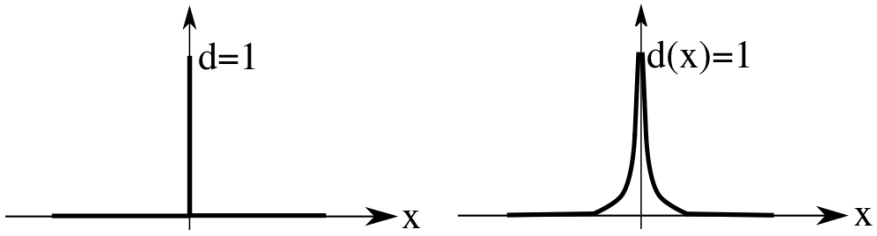


**Figure 2.6:** Sharp (left) and diffusive (right) approximation of the crack topology.

It is important to note that Γ-convergence to the Griffith solution has been proven in the context of phase-field modeling of brittle fracture [100]. A detailed derivation of this model is presented in Chapter 3.

The phase-field approach for modeling fracture finds application in several fields of study: dynamic brittle fracture [32, 32, 75, 134], mixed-mode fracture [90, 158], ductile fracture [4, 8, 6, 28, 46, 102], fracture due to fatigue [5], cohesive fracture [153, 100], fracture in anisotropic materials [40, 25, 92, 147], fracture in plates and shells [82, 6], fracture in thin films [101], fracture coupled with diffusion [159], fracture phenomena in soft biological tissues [70, 71, 129], fracture in highly heterogeneous materials obtained directly from micro computer tomography [117], fracture in fully saturated porous media with application to hydraulic fracture (fracking) [72, 106, 107, 132].

Phase-field models are validated experimentally for purely mechanical cases in [116, 90, 6, 35]. Furthermore, the model has gained interest and has been implemented in industrial softwares [165, 112, 110, 127, 94] as well as combined with other numerical methods [115]. An overview on the numerical implementation and numerical aspects of phase-field models for mechanical problems is shown in [138, 11].

### 2.3.3 Cracking in porous media

Cracking in porous media can be described with different numerical models[1]. The multiphase nature of such materials requires the use of coupled approaches, which are able to take into account the influence of the fluid phase on the solid phase and vice-versa. Examples of such approaches and their use in different applications are given in [140], e.g. alkali-silica chemical reaction inducing cracking in cementitious materials [124, 126], moisture loss in geomaterials as well as aging and drying in wood, drying in cement-based composites and desiccation in soils.

The phenomenon of desiccation has been numerically modeled by several authors [10, 128, 149, 62, 34] mostly aiming at a qualitative analysis of the crack patterns in different specimen types. A review on the physical behavior, experimental setups, and modeling approaches for initially water saturated clayey materials can be found in [84]. In [142, 123], the numerical specimen subjected to drying contains interface elements where a crack can propagate. Each interface is assigned a value of the tensile strength dependent on the current water content. Furthermore, the tensile strength is statistically distributed with a defined average and standard deviation. In this model, crack propagation is restricted to one direction, since the crack path is determined by the location of the interface elements and there are no transverse interface elements. In [123, 74], the strain evolution in drying specimens is modeled using a diffusion like equation with a given shrinkage coefficient. This approach has the advantage of being very simple but limits the coupling between the strain and the pressure developed inside the specimen. The number of cracks is calculated analytically. On the other hand, spring and discrete models for crack propagation are adopted in [114]. Due to the weak coupling between the drying phenomenon and fracture, these models are used to predict failure qualitatively. The extended finite element method has been used to model fluid-driven fracture [37, 130, 120]. This method is of very complex implementation especially in three-dimensional setting.

The complex nature of porous media leads to complex crack patterns originated, e.g. from distributed microcracks due to heterogeneities as well as cracks due to external restraints [140, 49, 21, 23]. Possibly complex crack topologies motivate the use of the phase-field approach. Phase-field modeling of fracture has been recently addressed for porous materials in [106, 107, 72, 166, 132, 53, 73, 151, 108], which however have only focused on the fully saturated case.

The change in saturation must be taken into account when modeling cracking induced by drying, which result from the advancement of pressure gradients. In materials with low permeability such as cementitious composites and soils, higher pressure gradients develop in comparison to more permeable materials [122, 21] and consequently, the variation of the degree of saturation must be taken into account.

The original contribution of this work is a modeling framework to deal with the coupled

[1]Some text passages have been quoted verbatim from [36].

problem of shrinkage-induced cracking in variably saturated porous media.

## 2.4 Summary

The first part of the chapter introduces the mechanics of porous media and its related concepts such as effective stress and degree of saturation. The phenomena of cracking due to volume changes in porous media are highlighted. The main idea is that drying induces shrinkage, which may lead to cracking in porous media in the presence of self-, internal and external restraints.

The second part of the chapter focuses on the modeling approaches in poromechanics and cracking phenomena. The coupled problem of shrinkage-induced cracking in porous media is addressed in Section 2.3.3.

Furthermore, the main terminology adopted in this work is defined:

- *Poromechanics* or *poroelasticity* denote the coupled problem of deformation and fluid flow in elastic porous media.
- *Effective stress*, which balances the stresses in the solid and fluid phases and expresses their intrinsic relationship.
- *Fully saturated* material, where the liquid phase occupies (ideally) the whole pore space.
- *Partially saturated* material with more than one fluid phase occupying the pore space, whose volume fractions can vary (*variable saturation*).
- *Saturation degree*, which quantifies the relative amount of each fluid in the porous material.
- *Shrinkage* denotes, i.e. negative change of volume or contraction. During internal drying *autogenous shrinkage* occurs. When moisture is lost to the ambient, *drying shrinkage* takes place.
- *Free shrinkage* occurs when the medium is able to contract freely, otherwise we have *restrained shrinkage*. When gradients in moisture content and in shrinkage within the material occur, *self-restraint* can take place leading a part of the specimen to resist the contraction of the rest. Furthermore, the material can be restrained due to *internal restraints* such as in heterogeneous materials and due to *external restraints*, which are e.g. caused by friction or imposed externally as volumetric limitations.
- Cracking induced by drying shrinkage in soils is denoted as *desiccation*.

As all available phase-field models for fracture in porous media consider the fully saturated case, the development of a coupled poromechanical-phase-field fracture modeling framework accounting for partially saturated conditions is set as goal in the present work. The phase-field modeling approach is suitable for modeling complex crack patterns due to drying in porous media.

# Part II

# Poromechanical-phase-field framework

# Chapter 3

# Phase-field modeling of fracture in variably saturated porous media

In this chapter, the governing equations of the coupled problem of deformation, drying and cracking are presented. These are three main equations: the equilibrium equation, the mass balance equation of the pore water pressure and the phase-field evolution equation with the displacement of the solid skeleton, the pore water pressure and the crack phase field as unknown fields[1].

## 3.1 Fundamentals

The principles of continuum mechanics theory are applied to model a porous medium at the macroscopic scale. Here, the pores and solid skeleton are not modeled explicitly and average properties are taken into account instead, which result from the homogenization of the phases (refer to Section 2.3.1, Fig. 2.5).

An arbitrary, undeformed domain $\Omega_0$ with boundary $\Gamma_0$ at the initial configuration is loaded/deformed within time. The domain undergoes infinitesimal deformations evolving to the deformed configuration $\Omega$ with boundary $\Gamma = \partial\Omega$ at the current time, Fig. 3.1.

The physics of the body is modeled with balance and constitutive equations as well as the kinematics, which represent an idealization of the problem in study.

In this work, three governing equations constitute the coupled problem of deformation, drying and cracking. The governing equations are described by the evolution of the following independent variables: the displacement vector, the pore water pressure and the crack phase-field. The equations that model the development of each variable are derived in detail in the following sections. Furthermore, the saturation degree varies

[1]Some text passages have been quoted verbatim from [36].

due to the drying.

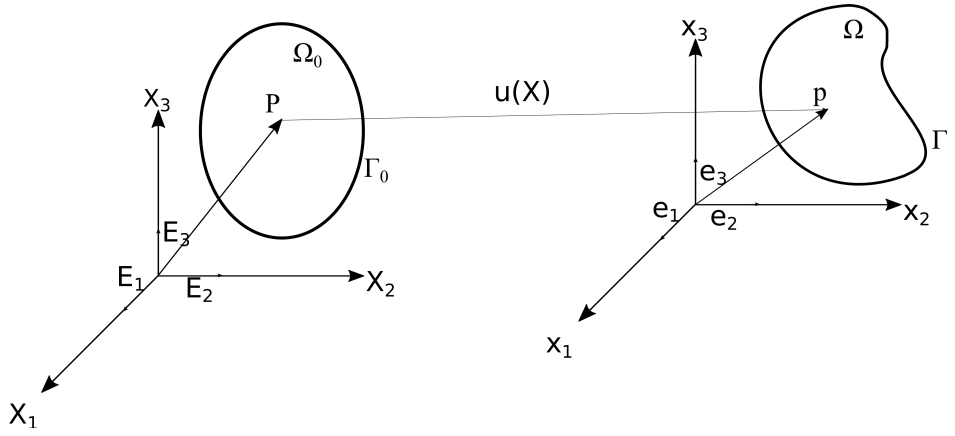


**Figure 3.1:** Arbitrary domain at the initial (undeformed, $\Omega_0$) and current (deformed, $\Omega$) configurations.

## 3.2 Governing equations of the poromechanical problem

The governing equations for a variably saturated porous medium at the macroscopic level are derived. They are based on the isothermal **u**-$p$ formulation for a three-phase material (solid, gas, liquid phases) developed in the geometrically linear setting within the Hybrid Mixture Theory [168, 91]

The variable **u** stands for the displacement vector whereas $p$ is the average pressure between the liquid and gas phases. In this work, the gas phase is composed of air and the gas pressure is kept constant and equal to the atmospheric pressure. Moreover, the air density is neglected following the passive air-phase assumption [168, 136].

The equilibrium equation of the porous medium is expressed in terms of total Cauchy stress tensor $\boldsymbol{\sigma}$ and body forces due to gravity as

$$\nabla \cdot \boldsymbol{\sigma} + \rho \mathbf{g} = \mathbf{0} \tag{3.2.1}$$

where **g** is the gravity acceleration vector and $\rho$ is the total density of the mixture which can be split for the solid and the fluid (water) phase by

$$\rho = \underbrace{(1-n)\rho_s}_{\rho_d} + nS_w\rho_w. \tag{3.2.2}$$

In this equation, $n$ is the porosity, $\rho_s$ is the density of the solid grains, $\rho_d$ is the dry or bulk density, $S_w$ is the liquid water degree of saturation and $\rho_w$ is the liquid water density.

The concept of effective stress $\boldsymbol{\sigma}'$, qualitatively introduced in Chapter 2, is used to express the relationship between the total Cauchy stress tensor and the pressure $p$ acting in the fluid [91, 118, 44] as follows

$$\begin{aligned} \boldsymbol{\sigma} &= \boldsymbol{\sigma}' - \alpha p \mathbf{I} \\ p &= \chi_w p_w + (1-\chi_w) p_a \\ p &\approx \chi_w p_w \approx S_w p_w \end{aligned} \tag{3.2.3}$$

In this equation, the average pressure is split into the contributions from the water pressure $p_w$ and the air pressure $p_a$. Since $p_a$ is assumed at constant atmospheric pressure[2], $p_a = 0$ and the average pressure is approximately $p_w$ multiplied by the parameter $\chi_w$, which stands for the contact area of the liquid water. Its value will be approximated by $S_w$ in further calculations [135]. Moreover, the coupling between the displacement $\mathbf{u}$ and the liquid water pressure $p_w$ is realized through the Biot parameter $\alpha$. This parameter is typically used in poroelasticity [41]. It depends on the average bulk modulus of the solid skeleton $K_T$ and the solid grain bulk modulus $K_s$ through the relation $\alpha = 1 - K_T/K_s$ for isotropic materials. In soils, $\alpha \simeq 1$ due to the near incompressibility (large modulus) of the solid grains in comparison with the solid skeleton [168].

Note that $\boldsymbol{\sigma}'$ is positive in tension and negative in compression, while $p_w$ is positive in compression and negative in tension.

For a partially saturated medium, the concept of capillary pressure $p_c$ (or matric suction) is defined at equilibrium as $p_c = p_a - p_w$ [67]. This equation is simplified to $p_c = -p_{rw}$, where $p_{rw}$ is the water pressure relative to the atmospheric pressure. For simplicity, the latter variable is further called $p_w$.

The effective stress tensor is computed with a constitutive law. Assuming linear elastic material behavior and absence of cracking,

$$\boldsymbol{\sigma}' = \mathcal{D} : \boldsymbol{\varepsilon} \tag{3.2.4}$$

with

$$\boldsymbol{\varepsilon} = \nabla^s \mathbf{u}. \tag{3.2.5}$$

where $\mathcal{D}$ is the constitutive tensor based on the elastic constants $\lambda$ and $G$ (Lamé parameters) and $\boldsymbol{\varepsilon}$ is the infinitesimal strain tensor computed as the symmetric part of the displacement gradient, $\nabla^s \mathbf{u}$.

Substituting Eqs. (3.2.2)-(3.2.4) into (3.2.1) results in

$$\nabla \cdot (\boldsymbol{\sigma}' - \alpha S_w p_w \mathbf{I}) + n S_w \rho_w \mathbf{g} + (1-n)\rho_s \mathbf{g} = \mathbf{0} \tag{3.2.6}$$

[2]The fluid pressures are calculated relatively to the atmospheric pressure according to the monospecies approach [67]

The second equation needed for the modeling of poromechanical processes is the mass balance equation of the liquid water,

$$\underbrace{\nabla \cdot (nS_w \mathbf{v}_{ws})}_{\text{(i)}} + \underbrace{n\frac{S_w}{K_w}\frac{\partial p_w}{\partial t}}_{\text{(ii)}} + \underbrace{C_s \frac{\partial p_w}{\partial t}}_{\text{(iii)}} + \underbrace{S_w \frac{\alpha - n}{K_s}\left(S_w + \frac{C_s}{n}p_w\right)\frac{\partial p_w}{\partial t}}_{\text{(iv)}} + \underbrace{S_w \alpha \frac{\partial \mathrm{tr}(\nabla^s \mathbf{u})}{\partial t}}_{\text{(v)}} = 0 \tag{3.2.7}$$

with $C_s = n\dfrac{\partial S_w}{\partial p_w}$ [168]. This equation contains the rate of water flow (i), where $\mathbf{v}_{ws}$ is the relative velocity of the liquid water with respect to the solid phase, and the accumulation terms (ii-v) in which we can recognize the contribution of the compressive volumetric strain of the liquid water with bulk modulus $K_w$ (ii), the variation of the water storage due to changes in liquid water saturation (iii), the change in volume of the solid phase due to the fluid pressure increase and to the effective stress (iv) and the change of strain with no variation of saturation (v) [168].

There are several possible constitutive equations for the flow of the liquid water such as Darcy's law or Poiseuille's law, among others. Here we assume Darcy's law (laminar flow), which for isotropic materials reads as follows

$$nS_w \mathbf{v}_{ws} = -k_{rw}\frac{k_i \mathbf{I}}{\mu_w}(\nabla p_w - \rho_w \mathbf{g}) \tag{3.2.8}$$

with $k_{rw}$ representing the relative permeability, $k_i$ the intrinsic permeability of the material and $\mu_w$ the dynamic viscosity of the fluid. The intrinsic permeability is expressed in $\mathrm{m}^2$ and is related to the hydraulic conductivity $k_w$ (expressed in m/s) by

$$k_w = k_i \frac{\rho_w g}{\mu_w} \tag{3.2.9}$$

where $g$ is the magnitude of $\mathbf{g}$.

In order to complement the initial boundary value problem constituted by the equilibrium equation Eq. (3.2.6) and the mass balance equation of liquid water Eq. (3.2.7) (combined with equations (3.2.4), (3.2.5) and (3.2.8)), all valid in the domain of interest $\Omega$, the following initial and boundary conditions are introduced

$$\begin{aligned}
p_w &= p_{w0} \quad \text{at} \quad t = 0 \\
\mathbf{u} &= \mathbf{u}_0 \quad \text{at} \quad t = 0 \\
\mathbf{u} &= \bar{\mathbf{u}} \quad \text{on} \quad \Gamma_u \\
\boldsymbol{\sigma} \cdot \mathbf{n} &= \bar{\mathbf{t}} \quad \text{on} \quad \Gamma_t \\
p_w &= \bar{p}_w \quad \text{on} \quad \Gamma_p \\
k_{rw}\frac{k_i \mathbf{I}}{\mu_w}(-\nabla p_w + \rho_w \mathbf{g}) \cdot \mathbf{n} &= \bar{q} \quad \text{on} \quad \Gamma_q
\end{aligned} \tag{3.2.10}$$

where $p_{w0}$ and $\mathbf{u}_0$ are the initial values for the water pressure and displacement fields, $\bar{\mathbf{u}}$ is the imposed displacement, $\mathbf{n}$ is the outward unit normal vector to the surface of the domain, $\bar{\mathbf{t}}$ is the imposed traction vector, $\bar{p}_w$ is the imposed water pressure and $\bar{q}$ is the imposed liquid water flux. $\Gamma_u$ and $\Gamma_t$ are respectively the Dirichlet and Neumann portions of the boundary $\Gamma = \partial\Omega$ associated to the displacement variable $\mathbf{u}$, whereas $\Gamma_p$ and $\Gamma_q$ are respectively the Dirichlet and Neumann portions of $\Gamma$ associated to $p_w$. It is $\Gamma_u \cup \Gamma_t = \Gamma_p \cup \Gamma_q = \Gamma$ and $\Gamma_u \cap \Gamma_t = \Gamma_p \cap \Gamma_q = \emptyset$. We further assume consistency of the initial and boundary conditions, i.e. $\bar{\mathbf{u}} = \mathbf{u}_0$ at time t=0 on $\Gamma_u$ and $\bar{p}_w = p_{w0}$ at t=0 on $\Gamma_p$.

From the physical point of view, the applied pressure boundary condition can be seen as a suction layer imposed on the boundary (if $\bar{p}_w < 0$). This suction layer can be implemented in terms of a constant pressure, e.g. when one accounts for a constant outer relative humidity, or a time-dependent field which affects the moisture distribution. The applied flux can be seen as a wetting boundary condition in case its sign is positive or as a drying flux if its sign is negative. The first induces positive pressure changes in the medium, while the second induces a negative pressure evolution, namely suction or capillary pressure. The two aforementioned boundary conditions, Dirichlet and Neumann, are interchangeable. In other words, an applied pressure can be computed in terms of flux and vice-versa. It can be cumbersome to determine the flux curve experimentally. To overcome this issue, the mass changes within time are determined experimentally and these are computed in terms of flux at the correct unities. In the current framework, the pressure boundary condition is given in $[\mathrm{N\,m^{-2}}]$, while the flux is imposed in $[\mathrm{m\,s^{-1}}]$.

With respect to the mechanical boundary conditions, the applied displacement can be used to drive the medium (displacement-driven path), to enforce symmetry and/or restraint. The degree of restraint can be imposed ideally, i.e. no movement is allowed and the displacements are equal to zero at the specified layer. On the other hand, when a variable degree of restraint is implemented, the applied displacement can vary proportionally to an elastic constant as a spring-like boundary condition. The traction boundary condition is related to the applied force on the medium. Due to softening effects in damaging materials, it is common to impose displacement-driven boundary conditions, since this quantity can be directly measured, e.g. during experiments. In the current framework, imposed displacements are given in [m], while tractions are imposed in [N].

## 3.3 Additional constitutive relations

The multiphase model is completed with additional constitutive equations. In a fully saturated porous medium, both the degree of saturation $S_w$ and the relative permeability $k_{rw}$ assume the value 1, which ideally represents a fully interconnected fluid water phase within the pore network. On the other hand, in a partially (or variably)

saturated porous medium, $S_w$ and $k_{rw}$ can vary and assume values smaller than 1. The variations are governed by changes in the capillary pressure $p_c$ that can be determined experimentally, see more details in Chapter 6. Commonly used functions are given by the van Genuchten model [152],

$$S_w = (1 - S_r) \cdot S_e + S_r \tag{3.3.1}$$

$$S_e = (1 + (\alpha_{vG} \cdot \varphi)^{n_{vG}})^{-m_{vG}} \tag{3.3.2}$$

$$k_{rw} = \sqrt{S_e} \left[1 - \left(1 - S_e^{1/m_{vG}}\right)^{m_{vG}}\right]^2 \tag{3.3.3}$$

with $p_c$ computed from the water pressure head $\varphi = \dfrac{p_c}{\rho_w g} = \dfrac{-p_w}{\rho_w g}$. The saturated state is recovered when $p_c = 0$. Here, $S_e$ is the effective saturation and $S_r$ is the residual saturation, which acts as a limit to the negative pressure determined experimentally on a very dry material. The parameters $\alpha_{vG}$ and $n_{vG}$ represent the air entry value and the rate of drying, respectively. These are the independent parameters in the modeling with the van Genuchten fitting [152] and are obtained from the experimental solid water retention curve (SWRC) or from sorption isotherms. The parameter $m_{vG}$ is computed using the relation $m_{vG} = 1 - 1/n_{vG}$ [152].

## 3.4 Phase-field modeling of brittle fracture in porous media

As follows, the phase-field approach is presented. The coupling to the poromechanical part by means of the effective stress is highlighted. Additionally, the computation of the fracture energy and its dependency on water content and age is discussed.

### 3.4.1 Phase-field model

The main idea and origins of the phase-field model for brittle fracture are discussed in Section 2.3.2. The phase-field formulation is based on the regularization of the variational formulation proposed by [56, 113]. In [56], the free energy functional $\mathrm{E}(\mathbf{u}, \Gamma)$ is minimized

$$\mathrm{E}(\mathbf{u}, \Gamma) = \int_\Omega \psi(\mathbf{u}) \mathrm{d}\Omega + \mathcal{G}_c \int_{\Gamma_d} \mathrm{d}\Gamma_d \tag{3.4.1}$$

where $\psi(\mathbf{u})$ is the stored elastic energy and $\Gamma_d$ is the crack set, or the portion of the boundary associated with the crack ($\Gamma_d \subset \Gamma$). The parameter $\mathcal{G}_c$ has been given different names in the literature: fracture resistance related to the fracture toughness

[86], fracture toughness [7], critical energy release rate [106] and fracture energy [72, 159]. In this work, we will term $\mathcal{G}_c$ fracture energy.

The variational formulation of brittle fracture consisting in the minimization of 3.4.1 is able to overcome the issues of crack initiation, pre-defined crack path and crack jumps along the crack path encountered in Griffith's theory [56]. However this formulation requires specialized numerical tools to be solved since it accounts for any admissible crack set and displacement field, see [31, 30] for a detailed explanation. For this reason, in the phase-field formulation the discrete crack in Eq. (3.4.1) is regularized by the crack phase-field variable $d$ that characterizes the state of the material with values ranging from 0 (intact material) to 1 (fully damaged material) [31]. The following regularized energy functional is obtained

$$\mathrm{E}_\ell(\mathbf{u}, d) = \int_\Omega g(d)\Psi(\mathbf{u}, d)\mathrm{d}\Omega + \mathcal{G}_c \int_\Omega \gamma(d, \nabla d)\mathrm{d}\Omega. \tag{3.4.2}$$

The degradation function $g(d)$ is defined as

$$g(d) = [(1-d)^2 + \eta] \tag{3.4.3}$$

where $\eta$ is a very small residual stiffness used to keep numerical stability in fully cracked conditions [103].

Note that the density of the elastic energy $\Psi(\mathbf{u}, d)$ evolves with the displacement and the crack phase-field variables. The crack energy density is given by

$$\gamma(d, \nabla d) = \frac{1}{2\ell} d^2 + \frac{\ell}{2} |\nabla d|^2. \tag{3.4.4}$$

In this equation, $\ell$ is the crack length scale parameter that is proportional to the width of the transition zone between cracked and intact states.

This type of energy functional with quadratic phase-field variable is classified as *Ambrosio-Tortorelli* (AT)-2 model [3]. For this type of energy, the damage starts immediately with loading. This function is used in the phase-field models of [28, 52, 86, 8, 36]. On the other hand, for the AT-1 type with linear phase-field variable, damage evolution does not start immediately, i.e. the onset of cracking is preceded by an elastic stage. This functional is used, e.g. in [4].

When a monotonic, positive load is applied such as in a simple tension test, i.e. by means of traction to stretch the body, there is an *active* energy contribution. In more complex scenarios such as during compression or shearing, both *active* and *non-active* energy contributions are expected. Since cracking is meant to occur due to an active energy contribution, it is important to differentiate between the energy contributions. The so called active-non-active[3] energy split of the elastic energy was proposed by several authors, we mention here the volumetric-deviatoric split [9], the deviatoric

[3] Also referred in the literature as *positive-negative* energy split.

split [89], the spectral decomposition [103], the combined cleavage-deviatoric split [57] and the crack normal stress based split proposed by [145, 146].

In order to account for the energy split in the energy functional, Eq. (3.4.2) is redefined as

$$\mathrm{E}_\ell(\mathbf{u}, d) = \int_\Omega [g(d)\Psi^+(\mathbf{u}) + \Psi^-(\mathbf{u})]\mathrm{d}\Omega + \mathcal{G}_c \int_\Omega \gamma(d, \nabla d)\mathrm{d}\Omega \tag{3.4.5}$$

where the active part is given by $\Psi^+$ and the non-active part by $\Psi^-$. Note that the degradation function only acts on the active part of the energy. This is meant to prevent cracking under compression and to enforce crack face contact in phase-field models, however it is known not to resolve all the connected issues. The development of an optimal split is still an open issue in the literature.

In one- or two-dimensions, the computation of the splits is straightforward. On the other hand, the task is more cumbersome when implementing, e.g. the spectral decomposition in three-dimensions due to the need to compute eigenvalues and eigenvectors. This is not the case for the volumetric-deviatoric split. In this work, we utilize the volumetric-deviatoric split from Amor et al. [9]. With this split, the energies are calculated as follows [9]:

$$\begin{aligned}
\Psi^+(\mathbf{u}) &= \frac{1}{2}\left(\lambda + \frac{2}{3}G\right)\langle \mathrm{tr}(\boldsymbol{\varepsilon}(\mathbf{u}))\rangle_+^2 + G(\boldsymbol{\varepsilon}(\mathbf{u})^{\mathrm{dev}} : \boldsymbol{\varepsilon}(\mathbf{u})^{\mathrm{dev}}) \\
\Psi^-(\mathbf{u}) &= \frac{1}{2}\left(\lambda + \frac{2}{3}G\right)\langle \mathrm{tr}(\boldsymbol{\varepsilon}(\mathbf{u}))\rangle_-^2
\end{aligned} \tag{3.4.6}$$

where $\langle \mathrm{tr}(\boldsymbol{\varepsilon})\rangle_\pm = \frac{1}{2}\left(\mathrm{tr}(\boldsymbol{\varepsilon}) \pm |\mathrm{tr}(\boldsymbol{\varepsilon})|\right)$ and $\boldsymbol{\varepsilon}^{\mathrm{dev}} = \boldsymbol{\varepsilon} - \frac{1}{\mathrm{dim}}\mathrm{tr}(\boldsymbol{\varepsilon})\mathbf{I}$ is the deviatoric strain tensor in the modeling dimension dim.

### 3.4.2 Coupling to the poromechanical model

The degradation function $g(d)$ realizes the coupling between the phase-field evolution and the mechanical problem. In the present case, where the standard mechanical problem is replaced by a poromechanical formulation, the *first source of coupling* between the poromechanical problem and the fracture problem is obtained through the concept of effective stress. The generalized effective stress is expressed as:

$$\boldsymbol{\sigma}' = g(d)\,\boldsymbol{\sigma}'^{+} + \boldsymbol{\sigma}'^{-} \tag{3.4.7}$$

where

$$\begin{aligned}
\boldsymbol{\sigma}'^{+} &= \frac{\partial \Psi^+(\boldsymbol{\varepsilon})}{\partial \boldsymbol{\varepsilon}} = \left(\lambda + \frac{2}{3}G\right)\langle \mathrm{tr}(\boldsymbol{\varepsilon})\rangle_+ \mathbf{I} + 2G\boldsymbol{\varepsilon}^{dev} \\
\boldsymbol{\sigma}'^{-} &= \frac{\partial \Psi^-(\boldsymbol{\varepsilon})}{\partial \boldsymbol{\varepsilon}} = \left(\lambda + \frac{2}{3}G\right)\langle \mathrm{tr}(\boldsymbol{\varepsilon})\rangle_- \mathbf{I}
\end{aligned} \tag{3.4.8}$$

The constitutive tensor of the solid skeleton is computed corresponding to the stress split,

$$\mathcal{D} = \mathcal{D}^+ + \mathcal{D}^- \tag{3.4.9}$$

with positive and negative parts given by:

$$\begin{aligned} \mathcal{D}^+ &= \frac{\partial \boldsymbol{\sigma}'^+}{\partial \boldsymbol{\varepsilon}} \\ \mathcal{D}^- &= \frac{\partial \boldsymbol{\sigma}'^-}{\partial \boldsymbol{\varepsilon}} \end{aligned} \tag{3.4.10}$$

The necessary condition for minimization of the functional (3.4.5) with respect to $d$ [105, 103] is

$$\frac{\partial \mathrm{E}_\ell}{\partial d} - \nabla \cdot \frac{\partial \mathrm{E}_\ell}{\partial \nabla d} = 0$$

which leads to the phase-field evolution equation

$$\frac{\mathcal{G}_c}{\ell}[d - \ell^2 \, \Delta d] - 2(1-d)\mathcal{H} = 0 \tag{3.4.11}$$

where $\mathcal{H} = \max_{\tau \in [0,t]} \Psi^+(\mathbf{u}, \tau)$ is the maximum energy within the loading history up to the current instant $t = \tau$. The possible Dirichlet constraint for the phase-field on $\Gamma_c$ is $d = \bar{d}$, e.g. $\bar{d} = 1$ for pre-cracked material. The Neumann boundary condition for the phase-field on $\Gamma_d$ is $\nabla d \cdot \mathbf{n} = 0$. The introduction of $\mathcal{H}$ is used to enforce the irreversibility of the phase-field evolution equation within a staggered solution scheme [103], which is discussed in more detail in Chapter 4.

### 3.4.3 Homogeneous solution of the phase-field equation

The homogeneous solution of the phase-field evolution equation enables us to obtain the critical parameters of the approach and to derive important relationships. The analytical solution concentrates on the tensile loading of a bar under homogeneous deformations as discussed in Section 2.3, Fig. 2.6, i.e. positive loading and one-dimensional domain. The homogeneous solution is derived in [29] as

$$d_{hom} = \begin{cases} \left( \dfrac{2\ell E}{\mathcal{G}_c} \varepsilon_{hom}^2 + 1 \right)^{-1} & \text{if } \Psi^+ = \mathcal{H} \\ \left( \dfrac{4\ell}{\mathcal{G}_c} \mathcal{H} + 1 \right)^{-1} & \text{if } \Psi^+ < \mathcal{H} \end{cases}$$

$$\boldsymbol{\sigma}'_{hom} = \begin{cases} \left(\dfrac{2\ell E}{\mathcal{G}_c}\varepsilon_{hom}^2 + 1\right)^{-2} E\varepsilon_{hom} & \text{if } \Psi^+ = \mathcal{H} \\ \left(\dfrac{4\ell}{\mathcal{G}_c}\mathcal{H} + 1\right)^{-2} E\varepsilon_{hom} & \text{if } \Psi^+ < \mathcal{H} \end{cases} .$$

The homogeneous solution is compared to the solution from gradient models in [45]. The analysis shows that phase-field models overcome the issue of broadening of the damaged zones due to their vanishing driving force when the crack is developed, i.e. the derivative of the degradation function vanishes when $d = 1$.

Furthermore, the homogeneous solution can be used to compute the critical stress and critical strain, which in turn relate to the fracture energy as described in the following.

### 3.4.4 Fracture energy

The fracture energy is an important material parameter in the phase-field model of fracture. This quantity can be determined experimentally by direct and indirect tests, e.g. Brazilian test [143], wedge splitting tests [141] and compact tension tests [88]. For porous materials such as clay, the value of $\mathcal{G}_c$ is not uniquely defined in the literature. It is found that it can be a function of the water content of the porous medium [144, 121]. For cement-based materials, the fracture energy is a function of age and degree of hardening [48].

Based on the homogeneous solution of the phase-field problem, the fracture energy is related to the tensile strength $\sigma_t$, Young's modulus $E$ and crack length scale $\ell$ as [29]

$$\sigma_t = \frac{9}{16}\sqrt{\frac{\mathcal{G}_c E}{6\ell}}. \tag{3.4.12}$$

Other solutions for gradient-based damage models to compute the critical stress can be found in [125, 14].

In this work, we follow the approach to compute the fracture energy by keeping the length scale parameter constant and expressing $\sigma_t$ and $E$ as functions of the age $a$ and water content $w = nS_w\rho_w/\rho_d \times 100$. For this reason, $\mathcal{G}_c$ also becomes a function of $a$ and $w$ as follows

$$\mathcal{G}_c(a, w, \ell) = \left(\frac{16}{9}\right)^2 \sigma_t(a, w)^2 \frac{6\ell}{E(a, w)}. \tag{3.4.13}$$

This constitutes the *second source of coupling* between the poromechanical and the fracture problems. From this equation, and with the choice of the functions $\sigma_t(a, w)$ and $E(a, w)$ that will be illustrated in Chapter 5, the fracture energy in e.g. soils

decreases with drying ($w \to 0$) and cracking becomes more likely to occur. This behavior is in agreement with experiments relating the water content and the fracture energy in specimens with variable water content [88].

### *Remarks*

- Note that the influence of the crack on the evolution of hydraulic properties such as the permeability is not taken into account in the current framework and will be the subject of further research. A preliminary study with that respect and experimental results utilizing neutron imaging technique are presented in Appendix A. These show the necessity to account for a strong, two-way coupling between the pressure- and crack-fields.
- In the literature, few works take into account the influence of the crack field on the fluid pressure field. These assume the change of flow regime in the cracked region, e.g. Darcy to Poiseuille, through an empirical relationship [104, 53, 72, 2]. An example of this consideration is shown in [104], where an additional criterion associated with the phase-field evolution is established. Another approach is to define an additional mass balance for the flow inside the crack [163] and let it evolve when a crack develops.

## 3.5 Summary

A mathematical framework for modeling the coupled phenomena of shrinkage, drying and cracking is derived. The modeling is based on the mechanical equilibrium equation, the mass balance equation of the pore water and the phase-field evolution for brittle fracture. The strong form of the problem with unknown fields $\mathbf{u}$-$p_w$-$d$ is defined by Equations (3.2.6), (3.2.7) and (3.4.11), together with the constitutive equations (3.2.8), (3.3.1)-(3.3.3) and (3.4.7)-(3.4.8) and the kinematics (3.2.5).

The sources of coupling between the poromechanical and fracture problems are pointed out:

- The *first source of coupling* is the effective stress.
- The *second source of coupling* is the expression of the fracture energy containing hygral and/or age dependent variables.

Note that a one-way coupling between crack and water pressure fields is defined. First steps are taken to improve this coupling, as shown in Appendix A.

The homogeneous solution of the crack phase-field evolution equation is discussed and rearranged such that the fracture energy can be computed as a function of length scale

parameter, tensile strength and Young's modulus. By accounting for experimentally-observed effects in porous media such as the variation of the elastic modulus and tensile strength with the water content in soils as well as the degree of hardening in cementitious materials, we can compute the fracture energy dependent on these relevant quantities, e.g. $\mathcal{G}_c(w)$ in soils.

The numerical treatment of the framework is discussed in Chapter 4.

# Chapter 4

# Finite element treatment

The numerical treatment of the mathematical model for the coupled problem of deformation, drying and cracking presented in the previous chapter is described. The numerical implementation is based on a mixed formulation with the finite element method.

## 4.1 Weak form

As shown in Chapter 3, the system in study is idealized and mathematically modeled with partial differential equations. Due to the complexity and nonlinear nature of the initial boundary value problem, an exact, analytical solution cannot be obtained. The finite element method is a common technique to deal with the discretization and approximate solution of partial differential equations [13]. As a preliminary step for the finite element treatment, the weak form of the governing equations is sought.

### 4.1.1 Equilibrium equations

The strong form of the equilibrium equations (Eq. (3.2.6)) with Dirichlet and Neumann boundary conditions (Eq. (3.2.10)) reads

$$\begin{aligned} \nabla \cdot \underbrace{(\boldsymbol{\sigma}' - \alpha S_w p_w \mathbf{I})}_{\boldsymbol{\sigma}} + nS_w\rho_w\mathbf{g} + (1-n)\rho_s\mathbf{g} &= \mathbf{0} \quad \text{in } \Omega \\ \mathbf{u} &= \bar{\mathbf{u}} \quad \text{on } \Gamma_u \\ \boldsymbol{\sigma}\cdot\mathbf{n} &= \bar{\mathbf{t}} \quad \text{on } \Gamma_t. \end{aligned}$$

The governing equation is multiplied by the test function $\mathbf{w}^u$ satisfying the homogeneous Dirichlet boundary condition $\mathbf{w}^u = \mathbf{0}$ on $\Gamma_u$ and integrated

$$\int_\Omega \mathbf{w}^u \cdot (\nabla \cdot (\boldsymbol{\sigma}' - \alpha S_w p_w \mathbf{I}) + nS_w\rho_w\mathbf{g} + (1-n)\rho_s\mathbf{g})\,\mathrm{d}\Omega = 0 \tag{4.1.1}$$

The choice of the test function depends on the chosen solution method and is specified in Section 4.2. The bilinear functional integrated over the domain $\Omega$ and the linear functional integrated over the boundary $\Gamma$ are calculated. For a clear overview, the stress term of Eq. (4.1.1) is treated separately:

$$\begin{aligned}
\int_\Omega \mathbf{w}^u \cdot (\nabla \cdot (\boldsymbol{\sigma}' - \alpha S_w p_w \mathbf{I}))\mathrm{d}\Omega &= -\int_\Omega \nabla \mathbf{w}^u : (\boldsymbol{\sigma}' - \alpha S_w p_w \mathbf{I})\mathrm{d}\Omega \\
&\quad + \int_{\Gamma_t} \mathbf{w}^u \cdot (\boldsymbol{\sigma}' - \alpha S_w p_w \mathbf{I}) \cdot \mathbf{n}\, \mathrm{d}\Gamma_t \\
&= -\int_\Omega \nabla \mathbf{w}^u : (g(d)\, \boldsymbol{\sigma}'^{+} + \boldsymbol{\sigma}'^{-})\mathrm{d}\Omega \\
&\quad + \int_\Omega \nabla \mathbf{w}^u : (\alpha S_w p_w \mathbf{I})\mathrm{d}\Omega + \int_{\Gamma_t} \mathbf{w}^u \cdot \boldsymbol{\sigma} \cdot \mathbf{n}\, \mathrm{d}\Gamma_t \\
&= -\int_\Omega \nabla \mathbf{w}^u : (g(d)\, \mathcal{D}^{+} : \nabla^s \mathbf{u} + \mathcal{D}^{-} : \nabla^s \mathbf{u})\mathrm{d}\Omega \\
&\quad + \int_\Omega \nabla \mathbf{w}^u : (\alpha S_w p_w \mathbf{I})\mathrm{d}\Omega + \int_{\Gamma_t} \mathbf{w}^u \cdot \boldsymbol{\sigma} \cdot \mathbf{n}\, \mathrm{d}\Gamma_t
\end{aligned} \tag{4.1.2}$$

Note that the degradation function and the split of the energy are already taken into account in the weak form.

The residual corresponding to the equilibrium equations, $R^u = 0$, is given by

$$\begin{aligned}
R^u &= -\int_\Omega \nabla \mathbf{w}^u : (g(d)\, \mathcal{D}^{+} : \nabla^s \mathbf{u} + \mathcal{D}^{-} : \nabla^s \mathbf{u})\mathrm{d}\Omega \\
&\quad + \int_\Omega \nabla \mathbf{w}^u : (\alpha S_w p_w \mathbf{I})\mathrm{d}\Omega + \int_\Omega \mathbf{w}^u \cdot n S_w \rho_w \mathbf{g}\mathrm{d}\Omega \\
&\quad + \int_\Omega \mathbf{w}^u \cdot (1-n)\rho_s \mathbf{g}\mathrm{d}\Omega + \int_{\Gamma_t} \mathbf{w}^u \cdot \bar{\mathbf{t}}\, \mathrm{d}\Gamma_t.
\end{aligned} \tag{4.1.3}$$

### 4.1.2 Mass balance equation of the liquid water

The strong form of the mass balance equation of the liquid water (Eq. (3.2.7)) complemented with Darcy's law (Eq. (3.2.8)) and the Dirichlet and Neumann boundary conditions (Eq. (3.2.10)) reads

$$\begin{aligned}
\nabla \cdot \left[ -k_{rw} \frac{k_i \mathbf{I}}{\mu_w} (-\nabla p_w + \rho_w \mathbf{g}) \right] + n \frac{S_w}{K_w} \frac{\partial p_w}{\partial t} + C_s \frac{\partial p_w}{\partial t} & \\
+ S_w \frac{\alpha - n}{K_s} \left( S_w + \frac{C_s}{n} p_w \right) \frac{\partial p_w}{\partial t} + S_w \alpha \frac{\partial \mathrm{tr}(\nabla^s \mathbf{u})}{\partial t} &= 0 \quad \text{in} \quad \Omega \\
p_w &= \bar{p}_w \quad \text{on} \quad \Gamma_p \\
k_{rw} \frac{k_i \mathbf{I}}{\mu_w} (-\nabla p_w + \rho_w \mathbf{g}) \cdot \mathbf{n} &= \bar{q} \quad \text{on} \quad \Gamma_q.
\end{aligned} \tag{4.1.4}$$

The governing equation is multiplied by the test function $w^p$ satisfying the homogeneous Dirichlet boundary condition $w^p = 0$ on $\Gamma_p$ and integrated

$$\int_\Omega w^p \left( \nabla \cdot \left[ -k_{rw} \frac{k_i \mathbf{I}}{\mu_w} (-\nabla p_w + \rho_w \mathbf{g}) \right] + n \frac{S_w}{K_w} \frac{\partial p_w}{\partial t} + C_s \frac{\partial p_w}{\partial t} \right.$$
$$\left. + S_w \frac{\alpha - n}{K_s} \left( S_w + \frac{C_s}{n} p_w \right) \frac{\partial p_w}{\partial t} + S_w \alpha \frac{\partial \mathrm{tr}(\nabla^s \mathbf{u})}{\partial t} \right) \mathrm{d}\Omega = 0. \quad (4.1.5)$$

The first term of Eq. (4.1.5) is treated separately:

$$\int_\Omega w^p \, \nabla \cdot \left[ -k_{rw} \frac{k_i \mathbf{I}}{\mu_w} (-\nabla p_w + \rho_w \mathbf{g}) \right] \mathrm{d}\Omega =$$
$$\int_\Omega \nabla w^p \cdot \left[ k_{rw} \frac{k_i \mathbf{I}}{\mu_w} (-\nabla p_w + \rho_w \mathbf{g}) \right] \mathrm{d}\Omega$$
$$- \int_{\Gamma_q} w^p \left[ k_{rw} \frac{k_i \mathbf{I}}{\mu_w} (-\nabla p_w + \rho_w \mathbf{g}) \right] \cdot \mathbf{n} \, \mathrm{d}\Gamma_q \quad (4.1.6)$$

The residual corresponding to the mass balance equation of the liquid water, $R^p = 0$, reads

$$R^p = \int_\Omega \nabla w^p \cdot \left[ k_{rw} \frac{k_i \mathbf{I}}{\mu_w} (-\nabla p_w + \rho_w \mathbf{g}) \right] \mathrm{d}\Omega + \int_\Omega w^p \, n \frac{S_w}{K_w} \frac{\partial p_w}{\partial t} \, \mathrm{d}\Omega$$
$$+ \int_\Omega w^p \, C_s \frac{\partial p_w}{\partial t} \, \mathrm{d}\Omega + \int_\Omega w^p \, S_w \frac{\alpha - n}{K_s} \left( S_w + \frac{C_s}{n} p_w \right) \frac{\partial p_w}{\partial t} \, \mathrm{d}\Omega$$
$$+ \int_\Omega w^p \, S_w \alpha \frac{\partial \mathrm{tr}(\nabla^s \mathbf{u})}{\partial t} \, \mathrm{d}\Omega - \int_{\Gamma_q} w^p \bar{q} \, \mathrm{d}\Gamma_q. \quad (4.1.7)$$

### 4.1.3 Phase-field evolution equation

The strong form of the phase-field evolution equation (Eq. (3.4.11)) and its Neumann boundary conditions on $\Gamma_d$ read

$$\frac{\mathcal{G}_c}{\ell} [d - \ell^2 \, \Delta d] - 2(1 - d)\mathcal{H} = 0 \quad \text{in} \quad \Omega$$
$$\nabla d \cdot \mathbf{n} = 0 \quad \text{on} \quad \Gamma_d.$$

The governing equation is multiplied by the test function $w^d$ satisfying $w^d = 0$ on $\Gamma_d$ and integrated

$$\int_\Omega w^d \left( \frac{\mathcal{G}_c}{\ell} [d - \ell^2 \, \Delta d] - 2(1 - d)\mathcal{H} \right) \mathrm{d}\Omega = 0. \quad (4.1.8)$$

The second term of Eq. (4.1.8) is treated separately:

$$- \int_\Omega w^d \mathcal{G}_c \ell \, \Delta d \, \mathrm{d}\Omega = \int_\Omega \nabla w^d \cdot \mathcal{G}_c \ell \, \nabla d \, \mathrm{d}\Omega - \int_{\Gamma_d} w^d \, \mathcal{G}_c \ell \, \nabla d \cdot \mathbf{n} \, \mathrm{d}\Gamma_d$$

The residual corresponding to the phase-field evolution equation, $R^d = 0$, is given by

$$R^d = \int_\Omega w^d \frac{\mathcal{G}_c}{\ell}\, d\, \mathrm{d}\Omega + \int_\Omega \nabla w^d \cdot \mathcal{G}_c \ell\, \nabla d\, \mathrm{d}\Omega - \int_\Omega w^d 2(1-d)\mathcal{H}\, \mathrm{d}\Omega. \tag{4.1.9}$$

## 4.2 Discretization

### 4.2.1 Temporal discretization

The time-dependent nature of the problem requires a time discretization. In this work, the backward, or implicit Euler scheme, is applied as follows

$$\frac{\partial \mathbf{u}}{\partial t}_{n+1} \approx \frac{\mathbf{u}_{n+1} - \mathbf{u}_n}{\Delta t} \quad \text{and} \quad \frac{\partial p_w}{\partial t}_{n+1} \approx \frac{p_{wn+1} - p_{wn}}{\Delta t}. \tag{4.2.1}$$

The subscripts $n$ and $n+1$ denote the previous and the current time steps, $t_n$ and $t_{n+1}$, respectively, and $\Delta t$ is the time increment. The unknowns discretized in time are substituted in the following.

### 4.2.2 Spatial discretization

The unknown fields $\mathbf{u}$-$p_w$-$d$ must be discretized in order to be solved for computationally. Here, the continuous domain is replaced by discrete finite elements, as shown in Fig. 4.1.

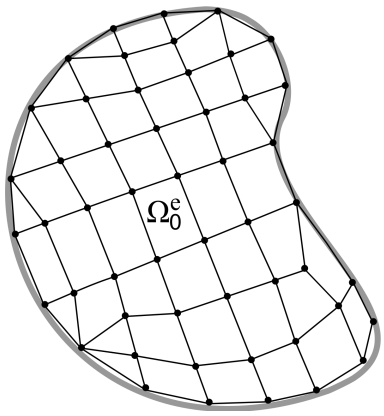


**Figure 4.1:** Discretized arbitrary domain at the initial configuration. The finite element discretization represents an approximation of the continuum domain.

The discretized domain $\Omega^h$ approximates the continuous domain $\Omega_0$ according to

$$\Omega_0 \approx \Omega_0^h = \bigcup_{e=1}^{n_e} \Omega_0^e \tag{4.2.2}$$

where $e$ is the element number, $n_e$ is the total number of elements. The domain of the element is given by $\Omega_0^e$.

The continuous variables $\mathbf{u}$, $p_w$ and $d$, are approximated by their discretized counterparts, $\mathbf{u}^h$, $p_w^h$ and $d^h$, respectively. The discretized solution is given by

$$\begin{aligned} \mathbf{u}^h &= \sum_{k=1}^{n_n} \phi_k^u \, \hat{\mathbf{u}}_k = \boldsymbol{\phi}^{u\,T} \, \hat{\mathbf{u}} \\ p_w^h &= \sum_{k=1}^{n_n} \phi_k^p \, \hat{p}_{w_k} = \boldsymbol{\phi}^{p\,T} \, \hat{\mathbf{p}}_w \\ d^h &= \sum_{k=1}^{n_n} \phi_k^d \, \hat{d}_k = \boldsymbol{\phi}^{d\,T} \, \hat{\mathbf{d}} \end{aligned} \tag{4.2.3}$$

where $n_n$ is the total number of nodes, $\phi_k^u$, $\phi_k^p$ and $\phi_k^d$ are the shape functions and $\boldsymbol{\phi}^u$, $\boldsymbol{\phi}^p$ and $\boldsymbol{\phi}^d$ are the shape function vectors. The vectors of the nodal unknowns $\hat{\mathbf{u}}$, $\hat{\mathbf{p}}_w$ and $\hat{\mathbf{d}}$ are expressed by

$$\hat{\mathbf{u}} = \begin{bmatrix} \hat{\mathbf{u}}_1 \\ \hat{\mathbf{u}}_2 \\ \vdots \\ \hat{\mathbf{u}}_{n_n} \end{bmatrix}, \; \hat{\mathbf{p}}_w = \begin{bmatrix} \hat{p}_{w_1} \\ \hat{p}_{w_2} \\ \vdots \\ \hat{p}_{w_{n_n}} \end{bmatrix} \quad \text{and} \quad \hat{\mathbf{d}} = \begin{bmatrix} \hat{d}_1 \\ \hat{d}_2 \\ \vdots \\ \hat{d}_{n_n} \end{bmatrix}. \tag{4.2.4}$$

In the standard finite element approach (Bubnov-Galerkin), the test functions are discretized with the same shape functions as the solution functions, i.e. $\mathbf{w}^u \approx \mathbf{w}^{u\,h} = \hat{\mathbf{w}}^{u\,T} \boldsymbol{\phi}^u$, $w^p \approx w^{p\,h} = \hat{\mathbf{w}}^{p\,T} \boldsymbol{\phi}^p$ and $w^d \approx w^{d\,h} = \hat{\mathbf{w}}^{d\,T} \boldsymbol{\phi}^d$.

Furthermore, the gradients of the continuous variables $\nabla \mathbf{u}$, $\nabla p_w$ and $\nabla d$ are required. These are approximated by their corresponding discretized counterparts, which are computed as

$$\begin{aligned} \nabla \mathbf{u}^h &= \sum_{k=1}^{n_n} \tilde{\mathbf{B}}_k^u \, \hat{\mathbf{u}}_k = \mathbf{B}^u \, \hat{\mathbf{u}} \\ \nabla p_w^h &= \sum_{k=1}^{n_n} \phi_{k,\mathbf{x}}^p \, \hat{p}_{w_k} = \mathbf{B}^p \, \hat{\mathbf{p}}_w \\ \nabla d^h &= \sum_{k=1}^{n_n} \phi_{k,\mathbf{x}}^d \, \hat{d}_k = \mathbf{B}^d \, \hat{\mathbf{d}} \end{aligned} \tag{4.2.5}$$

where

$$\tilde{\mathbf{B}}_k^u = \begin{bmatrix} \phi_{k,x_1}^u & & \\ & \phi_{k,x_2}^u & \\ & & \phi_{k,x_3}^u \\ \phi_{k,x_2}^u & \phi_{k,x_1}^u & \\ & \phi_{k,x_3}^u & \phi_{k,x_2}^u \\ \phi_{k,x_3}^u & & \phi_{k,x_2}^u \end{bmatrix}, \quad \mathbf{B}^u = \begin{bmatrix} \tilde{\mathbf{B}}_1^u & \tilde{\mathbf{B}}_2^u & \dots & \tilde{\mathbf{B}}_{n_n}^u \end{bmatrix} \tag{4.2.6}$$

$$\mathbf{B}^p = \begin{bmatrix} \phi^p_{1,\mathbf{x}} & \phi^p_{2,\mathbf{x}} & \dots & \phi^p_{n_n,\mathbf{x}} \end{bmatrix}, \quad \mathbf{B}^d = \begin{bmatrix} \phi^d_{1,\mathbf{x}} & \phi^d_{2,\mathbf{x}} & \dots & \phi^d_{n_n,\mathbf{x}} \end{bmatrix}$$

and $\phi_{k,\mathbf{x}} = \begin{bmatrix} \dfrac{\partial \phi_k}{\partial x_1} & \dfrac{\partial \phi_k}{\partial x_2} & \dfrac{\partial \phi_k}{\partial x_3} \end{bmatrix}^T$.

The gradient operators are also used to compute the gradients of the test functions, i.e. $\nabla \mathbf{w}^u \approx \nabla \mathbf{w}^{u\,h} = \mathbf{B}^u \hat{\mathbf{w}}^u$, $\nabla w^p \approx \nabla w^{p\,h} = \mathbf{B}^p \hat{\mathbf{w}}^p$ and $\nabla w^d \approx \nabla w^{d\,h} = \mathbf{B}^d \hat{\mathbf{w}}^d$. The discretized form of each equation is reported in the following.

### 4.2.3 Equilibrium equation

The discretized form of $R^u$, Eq. (4.1.3), is given by

$$\begin{aligned} R^{uh} \;=\; & -\hat{\mathbf{w}}^{u\,T} \int_\Omega \mathbf{B}^{u\,T} : (g(d)\, \mathcal{D}^+ : \mathbf{B}^u + \mathcal{D}^- : \mathbf{B}^u \mathrm{d}\Omega\, \hat{\mathbf{u}}_{n+1} \\ & + \hat{\mathbf{w}}^{u\,T} \int_\Omega \mathbf{B}^{u\,T} : (\alpha S_w \boldsymbol{\phi}^{p^T} \mathbf{I}) \mathrm{d}\Omega\, \hat{\mathbf{p}}_{w_{n+1}} \\ & + \hat{\mathbf{w}}^{u\,T} \int_\Omega \boldsymbol{\phi}^u \cdot [n S_w \rho_w + (1-n)\rho_s]\, \mathbf{g}\, \mathrm{d}\Omega + \hat{\mathbf{w}}^{u\,T} \int_{\Gamma_t} \boldsymbol{\phi}^u \cdot \bar{\mathbf{t}}\, \mathrm{d}\Gamma_t. \end{aligned} \tag{4.2.7}$$

### 4.2.4 Mass balance equation of the pore water

The discretized form of $R^p$, Eq. (4.1.7), is given by

$$\begin{aligned} R^{ph} \;=\; & \hat{\mathbf{w}}^{p\,T} \int_\Omega \mathbf{B}^{p\,T} \left[ k_{rw} \frac{k_i \mathbf{I}}{\mu_w} (\mathbf{B}^p\, \hat{\mathbf{p}}_{w_{n+1}} + \rho_w \mathbf{g}) \right] \mathrm{d}\Omega \\ & + \hat{\mathbf{w}}^{p\,T} \int_\Omega \mathbf{B}^{p\,T} \left[ n \frac{S_w}{K_w} + C_s \right] \boldsymbol{\phi}^{p\,T}\, \mathrm{d}\Omega\, \frac{\hat{\mathbf{p}}_{w_{n+1}} - \hat{\mathbf{p}}_{w_n}}{\Delta t} \\ & + \hat{\mathbf{w}}^{p\,T} \int_\Omega \boldsymbol{\phi}^p\, S_w \frac{\alpha - n}{K_s} \left( S_w + \frac{C_s}{n} \underbrace{\boldsymbol{\phi}^p \hat{\mathbf{p}}_{w_{n+1}}}_{p^h_w} \right) \boldsymbol{\phi}^{p\,T}\, \mathrm{d}\Omega\, \frac{\hat{\mathbf{p}}_{w_{n+1}} - \hat{\mathbf{p}}_{w_n}}{\Delta t} \\ & + \hat{\mathbf{w}}^{p\,T} \int_\Omega \boldsymbol{\phi}^p\, S_w \alpha \frac{\partial \mathrm{tr}(\nabla^s \boldsymbol{\phi}^{u\,T})}{\partial t}\, \mathrm{d}\Omega\, \hat{\mathbf{u}}_{n+1} \\ & - \hat{\mathbf{w}}^{p\,T} \int_{\Gamma_q} \bar{q}\, \mathrm{d}\Gamma_q. \end{aligned} \tag{4.2.8}$$

### 4.2.5 Phase-field evolution equation

The discretized form of $R^d$, Eq. (4.1.9), is given by

$$R^{dh} = \hat{\mathbf{w}}^{dT} \int_\Omega \frac{\mathcal{G}_c}{\ell} \left[ \boldsymbol{\phi}^d \boldsymbol{\phi}^{dT} + \ell^2 \mathbf{B}^{dT} \mathbf{B}^d \right] \mathrm{d}\Omega \, \hat{\mathbf{d}} - \hat{\mathbf{w}}^{dT} \int_\Omega \boldsymbol{\phi}^d 2(1 - \boldsymbol{\phi}^{dT} \hat{\mathbf{d}}) \mathcal{H} \, \mathrm{d}\Omega. \tag{4.2.9}$$

## 4.3 Linearization

In the presence of nonlinearities, e.g. geometrical, due to boundary conditions or to the material behavior, the discretized equations need to be linearized to be solved, e.g. with the Newton-Raphson method. First, the residual $\mathbf{R}$ is computed and linearized

$$\Delta \mathbf{R} = \frac{\partial \mathbf{R}}{\partial \mathbf{U}} \Delta \mathbf{U} \tag{4.3.1}$$

with respect to the global solution vector $\mathbf{U} = [\hat{\mathbf{u}}^T \ \hat{\mathbf{p}}_w^T \ \hat{\mathbf{d}}^T]$ and its increment $\Delta \mathbf{U} = [\Delta \hat{\mathbf{u}}^T \ \Delta \hat{\mathbf{p}}_w^T \ \Delta \hat{\mathbf{d}}^T]$. The linear system of equations

$$\mathbf{R} + \Delta \mathbf{R} = \mathbf{0} \tag{4.3.2}$$

is solved at each iteration $i$ up to convergence of the Newton-Raphson method. The solution vector is updated at each iteration

$$\mathbf{U}_{n+1}^{i+1} = \mathbf{U}_{n+1}^{i} + \Delta \mathbf{U}_{n+1}^{i}.$$

The derivatives of each residual are computed and shown in Appendix B. Due to the coupling terms, the resulting system of equations is non-symmetric.

## 4.4 Solution

### 4.4.1 Solution scheme and choice of the shape functions

The poromechanical problem $\mathbf{u}$-$p_w$ can be solved through splitting schemes [42, 83, 38]. Main idea of this approach is to separate the solution of each equation of the poromechanical problem. The advantage of the scheme is that the order of the shape functions of each finite element can be chosen arbitrarily. Following a similar line, pressure correction methods seek the solution of the equilibrium equation and the mass balance equation separately via intermediate time steps. The technique enables the use of equal order elements and is applied to dynamic problems [99]. Further techniques such as the use of multi-point mixed finite elements for the displacement part and finite

volumes for the discretization of the pore pressure can be used (see [38] and references therein).

On the other hand, the monolithic approach to solve the **u**-$p_w$ problem is straightforward, however it requires the fulfillment of the Ladyzhenskaya-Babuška-Brezzi (LBB) condition [168, 91, 69], e.g. through the use of Taylor-Hood or Raviart-Thomas finite elements or the discontinuous Galerkin method.

In this work, the shape functions for the solution of **u**-$p_w$ are modeled by the Taylor-Hood element shown in Fig. 4.2(a). This element uses Lagrange polynomial basis functions of second order for the displacement and first order for the pore water pressure.

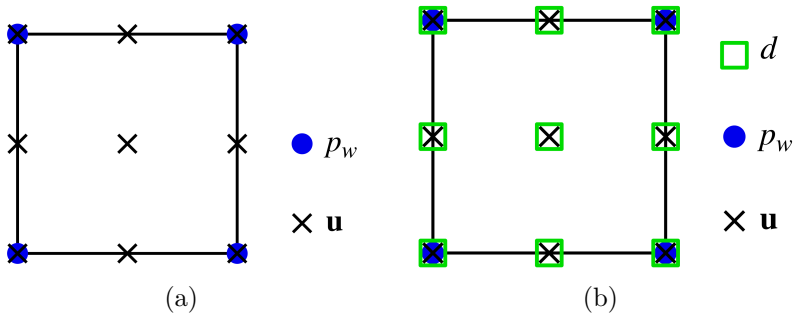


**Figure 4.2:** (a) Taylor-Hood element for discretization of the monolithic poromechanical problem. (b) The finite element is complemented with the nodes related to the crack phase-field.

The Taylor-Hood element is extended to account for the crack phase-field. The shape functions of the crack phase-field are chosen of second order such that displacement and phase-field have the same nodes (mesh) as shown in Fig. 4.2(b).

For the **u**-$d$ problem, i.e. for the purely mechanical problem, staggered or alternate minimization schemes are more robust, although less efficient than monolithic schemes [63, 103]. Staggered schemes are expected to always converge. However, the number of the required staggered iterations can be very large and it is heavily influenced by the time step size, see the detailed discussion in [63].

The system is solved with a staggered scheme [103]. Due to the low velocity of the drying process and due to the use of small time steps, an explicit staggered scheme is adopted in the solution of the phase-field evolution equation. Equations (4.1.3)-(4.1.9) are required in the implementation of the problem. The algorithm is summarized in Alg. 1. At $t = 0$, the stored elastic energy is set to zero and the initial and boundary values are initialized. As described in [36], the crack-field evolution equation is solved at the current time $t_{n+1}$. Then, the phase-field solution vector is frozen and inserted in the poromechanical equations, which are solved monolithically. The values of displacements and water pressure are computed at $t_{n+1}$, the corresponding solution vector **U** is frozen and the stored elastic energy is calculated/updated at each integration point.

If the current computed energy increases in comparison to the previously computed energy, the history variable is updated. Otherwise, the previously computed energy remains unchanged, i.e. in case the energy decreases or does not change. This strategy ensures the irreversibility of the crack-field variable. After the check, the history variable is inserted in the crack evolution equation and a new time step starts.

Due to the dependency of the elastic constants and/or fracture energy on the water content and/or age, Eq. (3.4.13), an update of these variables needs to be performed at each integration point after the solution of the poromechanical system.

**Initialization** ($t = t_0 = 0$)**:** $\bar{\mathbf{u}}$, $\bar{\mathbf{t}}$, $\bar{p}$, $\bar{q}$, $\bar{d}$, $\mathcal{H} = 0$;
**for** $n = 0 : N - 1$ **do**
  compute $\Psi^+(t = t_{n+1})$
  **if** $\Psi^+ > \mathcal{H}_n$ **then**
    $\mathcal{H}_{n+1} \leftarrow \Psi^+(t = t_{n+1})$;
  **else**
    $\mathcal{H}_{n+1} = \mathcal{H}_n$;
  **end**
  solve $d_{n+1}(\mathcal{H}_{n+1})$;
  solve $\mathbf{u}$-$p_w := \mathbf{U}_{n+1}(d_{n+1})$;
**end**

**Algorithm 1:** Algorithmic solution procedure for the $\mathbf{u}$-$p_w$-$d$ system (as shown in [36])

### 4.4.2 Solvers

As shown in the previous sections, after spatial and time discretizations followed by linearization, a coupled discretized $\mathbf{u}$-$p_w$-$d$ algebraic system of equations must be solved at each iteration of the Newton-Raphson solution scheme.

Iterative solvers are efficient, but require a good preconditioner in order for the solution to converge [17, 157, 54, 16, 156, 55, 98]. The constrained preconditioner and solver presented in [55] was tested in this work. This type of iterative procedure is able to treat the asymmetric matrix generated after discretization and preliminary results could be obtained.

Direct solvers are more robust and do not require preconditioning, however more computationally expensive when dealing with large systems (large number of degrees of freedom) due to the need for (approximate) matrix inversion. Due to this and to maintain the generality of the problem, direct solvers are used in the current work.

For implementation we use the finite element library `deal.II` [12]. This open-source library enables pre-processing of simple geometries and offers different elements and shape functions. Furthermore, the link with third-part libraries such as PetSC and Trillinos is built-in.

## 4.5 Summary

In this chapter, the numerical finite element treatment of the differential equations derived in Chapter 3 is described. First, the weak form of the equations is derived, then the unknown fields are discretized in time and space. The time dependency of the coupled problem is treated with the backward Euler method. Finally, non-linearities are treated with the Newton-Raphson iterative procedure.

The poromechanical equations are solved monolithically. In order to satisfy the LBB condition, a Taylor-Hood element is chosen for the description of the displacement vector and water pressure. This element is extended to account for the phase-field unknown, which is discretized with shape functions of the same order of the displacement field. A staggered scheme is adopted in the solution of the phase-field equation. To ensure the irreversibility of the crack-field variable, a history variable is adopted. The algorithmic implementation is discussed in detail and the system is solved using a direct solver.

# Part III

# Application to soils and verification of the framework

# Chapter 5

# Application to desiccation in soils

The poromechanical-phase-field framework presented in Chapter 3 is applied in the study of desiccation of soils. In the current chapter, the numerical results are compared with constrained desiccation experiments using input data found in the literature. Practical examples of one-, two- and three-dimensional desaturation and desiccation are studied with the developed framework [1].

The discretized set of linearized equations from the previous section is applied to study different numerical setups of variably saturated samples. The parameters used in each numerical test are specified in the respective example. In all computations, the bulk modulus, the dynamic viscosity and the density of the liquid water are assumed as follows: $K_w = 2.2\text{GPa}$, $\mu_w = 0.001\text{Pas}$ and $\rho_w = 1000\text{kg/m}^3$. Furthermore, the magnitude of the gravity $g = 9.81\text{m/s}^2$.

## 5.1 Verification of the numerical solution

The first two examples aim at verifying the **u**-$p_w$ model and the capability of the **u**-$p_w$-$d$ equations to simulate the crack development due to desaturation. After a convergence study, the time increment is set to $\Delta t = 1\text{s}$.

### 5.1.1 Estimation of geostatic stress state (consolidation)

In order to validate the poromechanical part of the framework and to start the actual computation of geomechanical problems, e.g. flow in a porous medium due to gravity, an initial computation of the geostatic stress state, also called consolidation is performed.

[1] Large part of this chapter is based and quoted verbatim from [36].

During consolidation, only the gravity force acts on the body. For the one-dimensional case of a column, the pore pressure is directly proportional to the height of the column and the specific gravity $\gamma_w = g\rho_w = 9.81\text{kN/m}^3$ as in

$$p_w = \gamma_w \, z \tag{5.1.1}$$

Figure 5.1(a) is a qualitative representation of the expected pressure distribution of a column exposed to the atmosphere. The water table indicates that fluid is flowing into the column allowing positive pressure to develop inside. If we move the water table along the column, a negative pressure, i.e. an unsaturated region, develops.

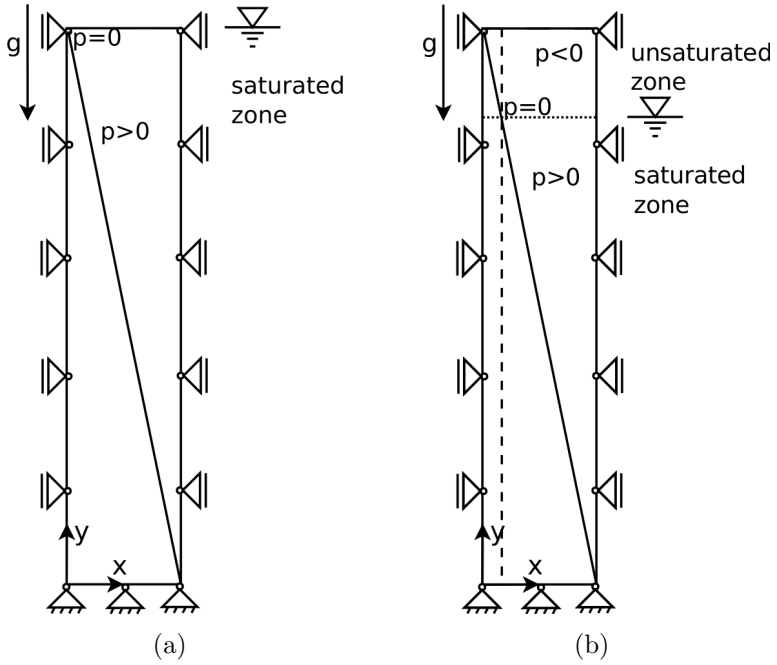


**Figure 5.1:** Pore pressure distribution during (a) consolidation and (b) when negative pressures develop.

The consolidation is simulated with a column of $1 \times 10$m and the numerically obtained results are compared to the analytical solution. Here, the geostatic stress state is achieved at $t = 450$ seconds and the analytical solution $p_w = 9.81\text{kN/m}^3 \times 10\text{m} = 98.1\text{kPa}$ is obtained at the bottom.

### 5.1.2 Desaturation of a column

This example is based on the experiment performed by Liakopoulos [93] concerning outflow of liquid water from a sand column due to gravity force. First, before starting the experiment (t<0), liquid water is continuously added from the top of a column of perspex with height $h = 1$m filled with Del Monte sand and is allowed to drain freely

at the bottom through a filter. When uniform flow is observed, the inflow of water is stopped ($t = 0$). The experiment reveals desaturation of the soil column from the top due to the action of the gravity force. A more detailed explanation regarding the test can be found in [60, 61]. In order to model the drainage process, the water pressure is kept constant at the bottom of the column and is equal to the seepage pressure ($p_w = 0$). The boundary conditions are shown in Fig. 5.2(a). The solid grain and liquid water are considered incompressible during the numerical simulation.

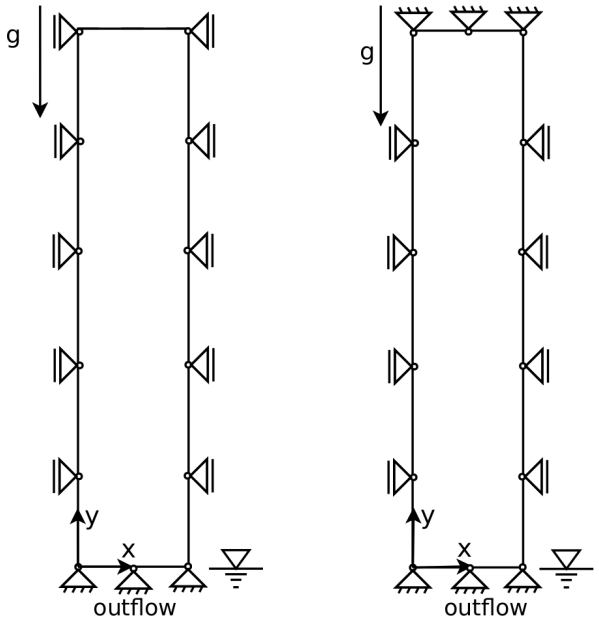


**Figure 5.2:** Boundary conditions for (a) desaturation and (b) restrained desaturation problems. The water level indicates that seepage pressure is imposed. The mechanical boundary conditions are shown schematically. Impervious and traction free boundary conditions are imposed over the remaining boundaries. The column is 1m high and 0.1m wide.

The constitutive equations for the water saturation and the relative permeability as presented in [60] are

$$\begin{aligned} S_w &= 1 - 1.9722 \times 10^{-11} p_c^{2.4279} \\ k_{rw} &= 1 - 2.207(1 - S_w)^{0.9529}. \end{aligned} \tag{5.1.2}$$

The material parameters used during the numerical test can be found in Table 5.1 [39].

The water loss from the bottom induces capillary pressure development along the column starting from the top, which, in turn, leads to partially saturated conditions and therefore to changes in the relative permeability and moisture content. The suction

**Table 5.1:** Parameters used in the modeling of a column subject to desaturation.

| n | $\rho_s$ | E | $\nu$ | $k_i$ |
|---|---|---|---|---|
| 0.2975 | 2000kg/m$^3$ | 1.3MPa | 0.4 | $4.5 \times 10^{-13}$m$^2$ |

together with the action of the gravity leads to the shrinkage of the column. Since the vertical displacements along the column are free, the column can deform vertically.

The numerical results of $\mathbf{u}$, $p_w$ and $S_w$ are compared with those of the benchmark results [80] from the Comes-Geo finite element code [91, 61, 131, 60] and show good agreement, see Fig. 5.3. The displacements due to consolidation of the specimen are subtracted from the total displacements, such that the plotted results are related exclusively to the time dependent process. A slightly different response of the vertical displacement is observed due to the use of the Taylor-Hood pair, while the results in [61, 80, 60] were obtained with bi-quadratic elements for the nodal displacements and pore pressures.

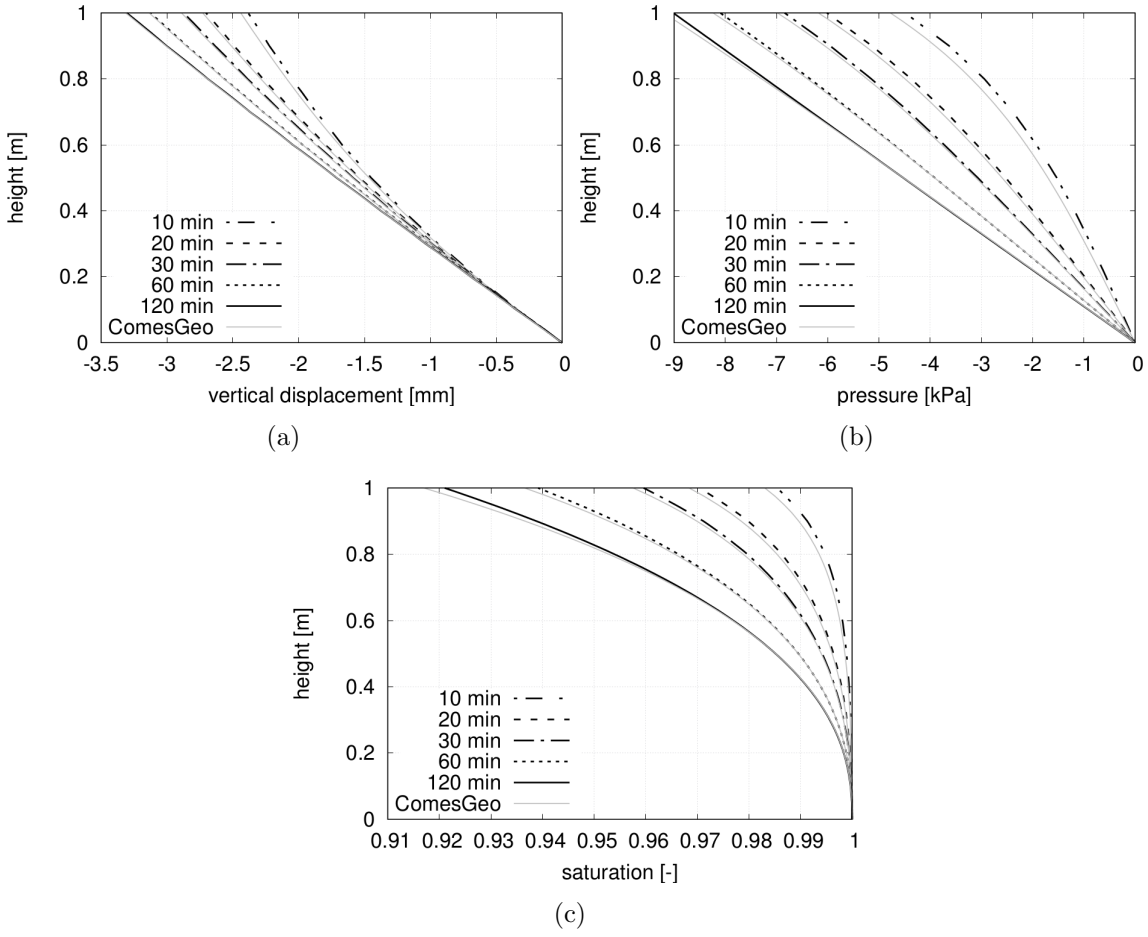


**Figure 5.3:** (a) Vertical displacement of the top edge, (b) liquid water pressure distribution and (c) water saturation degree along the column subject to desaturation and comparison with results from ComesGeo [61, 80, 131].

### 5.1.3 Desaturation of a restrained column

In the previous example, the column deforms freely in the vertical direction, allowing for the elastic energy to be fully released and, consequently, avoiding cracking. In order to verify the capability of the **u**-$p_w$-$d$ model to describe crack development, the nodes of the upper surface of the previous example are now restrained, Fig. 5.2(b). The other boundary conditions remain as in the previous example.

In the model, the water loss induces capillary pressures from the upper surface and, together with the mechanical constraint which prevents the settlement of the column, the formation of a positive vertical stress distribution in the same zone of the column as shown in Fig. 5.4(a) at an early time step, $t = 3$s. Cracking is expected to occur in the tension zone.

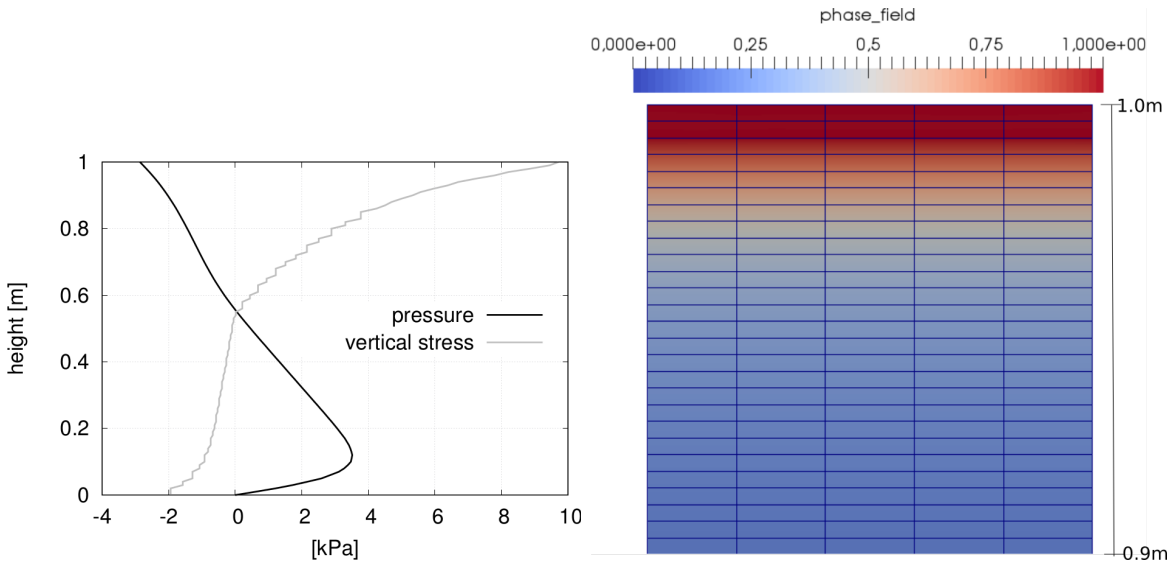


(a) (b)

**Figure 5.4:** Desaturation of a restrained column with test parameters $\mathcal{G}_c = 0.5$N/m and $\ell = 0.01$m. (a) Vertical stress and water pressure distributions at early stage $t = 3$s showing the positive and negative stress distribution along the column. (b) Phase-field evolution along the upper part of the restrained column with vertical coordinate between 0.9 and 1 meter at $t \approx 150$s.

Since the fracture properties of the material are not available in the literature, test values are chosen for $\mathcal{G}_c = 0.5$N/m and $\ell = 0.01$m, the latter corresponding to 1% of the height of the column.

The mesh is refined only along the vertical direction with element size $\ell/2$. With these parameters, localization of the crack-field variable is predicted by the numerical model at the top of the column. Figure 5.4(b) shows the phase-field distribution in the upper part of the column (vertical coordinate between $0.9h$ and $h$). It can be

observed that the thickness of the localization zone is consistent with the chosen crack length parameter. The corresponding degree of saturation in the cracked region is $S_w \approx 1$. The susceptibility of crack formation when $S_w \approx 1$ is in agreement with the observations of Péron [121].

## 5.2 Constrained desiccation test

In the following, a numerical model based on an experimental constrained desiccation test is presented. Computations are performed for a reference set of input parameters and results are analyzed in detail. Additionally, we investigate the influence of some input parameters (namely, the fracture energy, the mechanical restraint, the drying flux and the intrinsic permeability) on the numerical results.

### 5.2.1 Description of the test and input parameters

A constrained desiccation test is performed in order to show the capability of the model to describe the formation of multiple cracks during drying. The experimental tests from Péron [121] and Stirling [144, 142] are utilized as qualitative reference in the following numerical tests. Both authors consider clayey materials subjected to drying. Péron focuses his study on the desiccation of rectangular specimens restrained at the bottom while Stirling's specimen is inserted into a semi-cylindrical mould and left to dry. In Stirling's tests, there is no access to the sides of the specimen. The upper surface of the specimen is visible and the results are related to the top view. However, his work provides more detailed information regarding the hydraulic and mechanical properties of the material, that are necessary in our framework. For this reason, we utilize his data in the next numerical tests. Additionally, some observations provided by Péron are taken into account in the description of the behavior of constrained drying specimens.

Stirling's experimental setup consists of a steel mould which is first sandblasted. After the mould has a fixed sand line, it is filled with clay so that higher friction is created corresponding to a mechanical restraint. The clay is then compacted with a hammer for the purposes of homogenization and increase of the dry density. The density obtained by the author varies in the range of $1600 - 1650\text{kg/m}^3$.

The desiccation process starts with the initially water saturated material. In [144] several environmental conditions, i.e. different temperatures, are tested to determine the experimental drying flux. Drying occurs due to an increased ambient temperature around the saturated compacted sample, i.e. the higher temperature induces lower ambient relative humidity and the specimen loses water. No thermal expansion is reported. After one hour, a crack has already initiated on the surface of the specimen, propagating further on the upper surface and then vertically to the bottom of the mould. After 17 hours from the beginning of the test, the maximum degree of shrinkage

is achieved. No remarkable changes are observable in the next hours. The complete test takes 144 hours (6 days). Stirling observed one to two cracks that fully propagate through the specimen and several secondary cracks, i.e. cracks that do not propagate until the bottom. The differences in the crack propagation are related to the velocity of drying. No exact specifications regarding the crack onset time are reported.

In the numerical test, a two-dimensional half model of the specimen's longitudinal cross section is studied. This test is not aiming at quantitatively reproducing the experimental results but just at verifying if a qualitative agreement can be obtained. The model dimensions are $0.285 \times 0.051\text{m}^2$. The flux $\bar{q}$ is applied on the free drying surfaces of the specimen, while the bottom of the specimen is mechanically constrained as shown in Fig. 5.5. The value of the drying flux is chosen according to the discharge rates presented in [144]. The discharge rate is determined experimentally by the author. The material parameters can be found in Table 5.2. Furthermore the compressibility (bulk modulus) of the solid grains and the liquid water are taken into account.

**Table 5.2:** Parameters utilized in the modeling of the constrained desiccation test.

| n | $\rho_d$ | $k_i$ | $\alpha_{vG}$ | $S_r$ | $n_{vG}$ | $m_{vG}$ | $\bar{q}$ | $\ell$ |
|---|---|---|---|---|---|---|---|---|
| 0.41 | $1650\text{kg/m}^3$ | $10^{-15}\text{m}^2$ | $0.028\text{m}^{-1}$ | 0.15 | 1.3 | $1\text{-}1/n_{vG}$ | $6 \times 10^{-7}\text{m/s}$ | 0.002m |

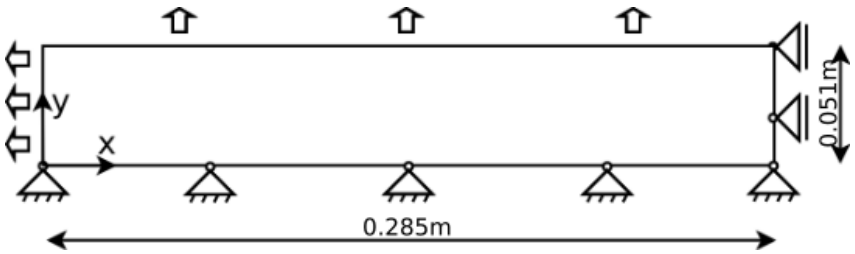


**Figure 5.5:** Constrained experimental based desiccation test. The model indicates the half-geometry used and mechanical boundary conditions. The applied drying flux $\bar{q}$ is represented by the arrows.

Finally, it is important to point out that the stiffness and the strength of the material increase during drying. Stirling proposed two functions relating the Young's modulus $E$ and the tensile strength $\sigma_t$ with the water content $w$, as follows

$$E = 1770\exp(-0.297w)\text{MPa} \tag{5.2.1}$$

$$\sigma_t = 228.85\exp(-0.14w)\text{kPa} \tag{5.2.2}$$

The Poisson's ratio $\nu = 0.3$.

These functions are used to compute the fracture energy of the material through Eq. (3.4.13). As indicated in Table 5.2, the length scale parameter is set to $\ell =$

0.002m. This value leads to a reasonable fracture energy ($\mathcal{G}_c(w=0) = 1.12$N/m and $\mathcal{G}_c(w=100) = 1.71$N/m) as found in the literature for clayey materials [121, 87]. As a result of a preliminary convergence study, we set the element size to $h = \ell/2$ and adopt $\Delta t = 1$s. Since the time increment is very small, the phase-field evolution equation is solved explicitly, i.e. no staggered iterations are carried out. In order to check the accuracy of the results, some tests were run with 10 staggered iterations and results are reported in Section 5.2.4. The residual stiffness is set to $\eta = 10^{-6}$. The end time of the simulation is $t = 120$ minutes.

As observed in the previous examples, gravity can be the unique driving load leading to the development of capillary pressure along the specimen when a seepage pressure is imposed as a strong boundary condition. Additionally, non-homogeneous Neumann natural boundary conditions can be applied. The applied flux can be constant or a function of time. In our numerical tests, we apply a constant drying flux on the free surfaces of the specimen (see Fig. 5.5 and Table 5.2).

### 5.2.2 Reference test

When the drying process starts, suction develops on the free surfaces of the specimen. The extraction of the water leads to increase of the suction that consequently leads to increase of the horizontal stresses along the specimen. In an early phase the horizontal stress is uniform along the upper drying surface of the specimen. At the extremity of the specimen, where the drying fluxes from the side and upper surfaces overlap, the horizontal stress is negative. A first qualitative study is shown in Fig. 5.6, where the pressure, displacement magnitude and horizontal stress fields are plotted. The negative pressure layer around the specimen (blue region in Fig. 5.6(a)) corresponds to higher suction values due to the applied drying flux in this region. The suction layer will extend to the interior of the specimen with time. The computation of the saturation degree along the extending drying layer reveals $S_w \approx 1$, which from experimental observations is known to be a favorable condition for cracking [121], see also end of Section 3. We observe slightly larger vertical shrinkage than lateral shrinkage in the specimen based on its deformed configuration in Fig. 5.6(b). The shrinkage is a result of the gravity action and applied drying flux. The horizontal stress field has a positive uniform distribution on the upper surface of the specimen except for the left edge, Fig. 5.6(c). The values close to the surface are higher than in the interior of the specimen. Due to the tensile nature of these stresses, crack in mode I is expected to occur, starting from the upper drying surface. This behavior has been observed in diverse experiments related to desiccation cracks in soils and also plain cement paste.

The uniform stress distribution corresponds to an uniform phase-field distribution, Fig. 5.7(a) and 5.7(b). The first localization zones of the crack field at the drying surface occur 44 minutes after the start of the test, Fig. 5.7(c). With further drying, the suction and the horizontal stress increase at the upper region and drive propagation of the upper crack downwards, Fig. 5.7(d). After full propagation of the upper crack,

the crack at the corner propagates further and the specimen starts detaching from the bottom. At $t = 85$ minutes, a second crack is observed in the medium, Fig. 5.7(e), followed by a third one that initiates 16 minutes later as shown in Fig. 5.7(f). Also, the crack at the bottom propagates further and the sample is almost fully detached from the bottom. The full detachment would lead to the release of the constraints, so that further desiccation occurs in free conditions and no further cracking would be observed.

It is interesting to understand the variation of quantities such as water pressure, degree of saturation and fracture energy during the test. The water pressure distribution along the specimen is shown in Fig. 5.8 for different time steps. The suction layer expands gradually from the outer layer to the inner core of the specimen, which can be better observed at later time steps due to the chosen range of the pressure field. After 15 minutes from the start of the test, the water pressure is negative everywhere and decreases continuously until the end of the test at 120 minutes. The distribution of the saturation degree is given in Fig. 5.9. At the beginning of the test, the specimen is fully saturated, $S_w = 1$. Due to the increase of suction in the medium as shown previously, the saturation degree decreases. At 15 minutes of test, $S_w \approx 0.99$ in the outer layer of the specimen (except at the upper left corner), Fig. 5.9(a). It is possible to recognize that the saturation degree in the inner part of the specimen is much higher than on the outer surface. This is related to the higher values of suction along the surface. Subsequently, the saturation degree decreases gradually, Figs. 5.9(b)-5.9(e), to a value of about 0.897 at the upper layer as shown in Fig. 5.9(f).

As previously mentioned, the fracture energy is a function of the water content in the body, which is computed from $S_w$. At the beginning of the test, the maximum value of the fracture energy is observed with $\mathcal{G}_c = 1.712$N/m. This value decreases with drying reaching the minimum of $\mathcal{G}_c = 1.639$N/m excluding the corner region of the specimen. At the left extremity of the specimen, $\mathcal{G}_c = 1.417$N/m. The results are shown in Fig. 5.10.

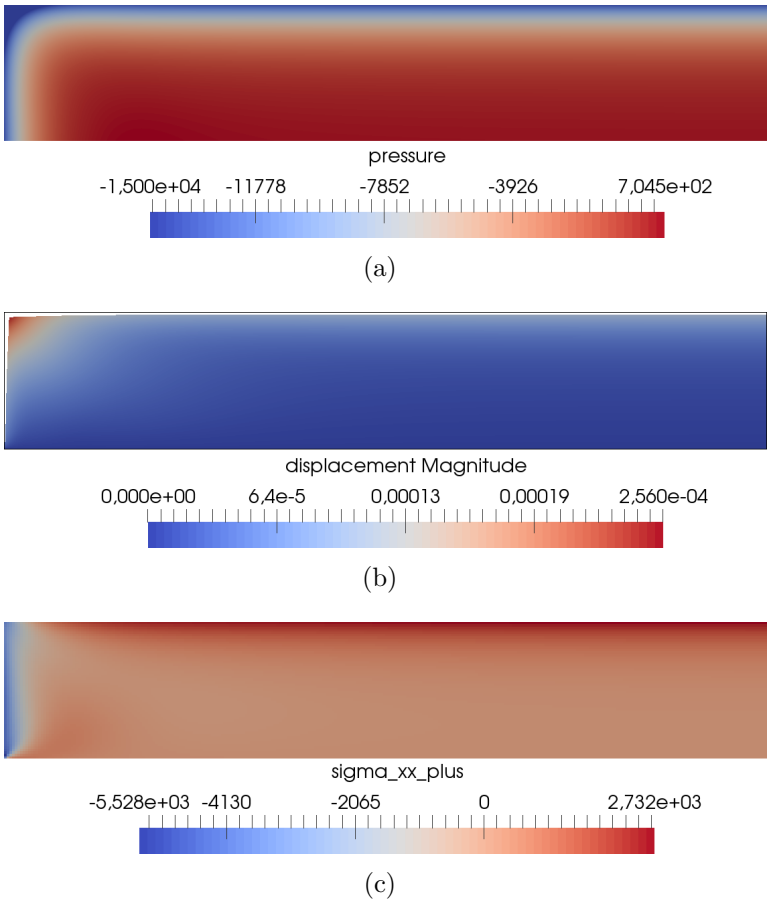


**Figure 5.6:** (a) Liquid water pressure in $Pa$, (b) displacement magnitude in $m$ plotted on the deformed configuration and scaled with factor 10 and (c) horizontal stress fields in $Pa$ at $t = 5$ minutes in the early stage for general evaluation of the behavior of the specimen during drying and before cracking.

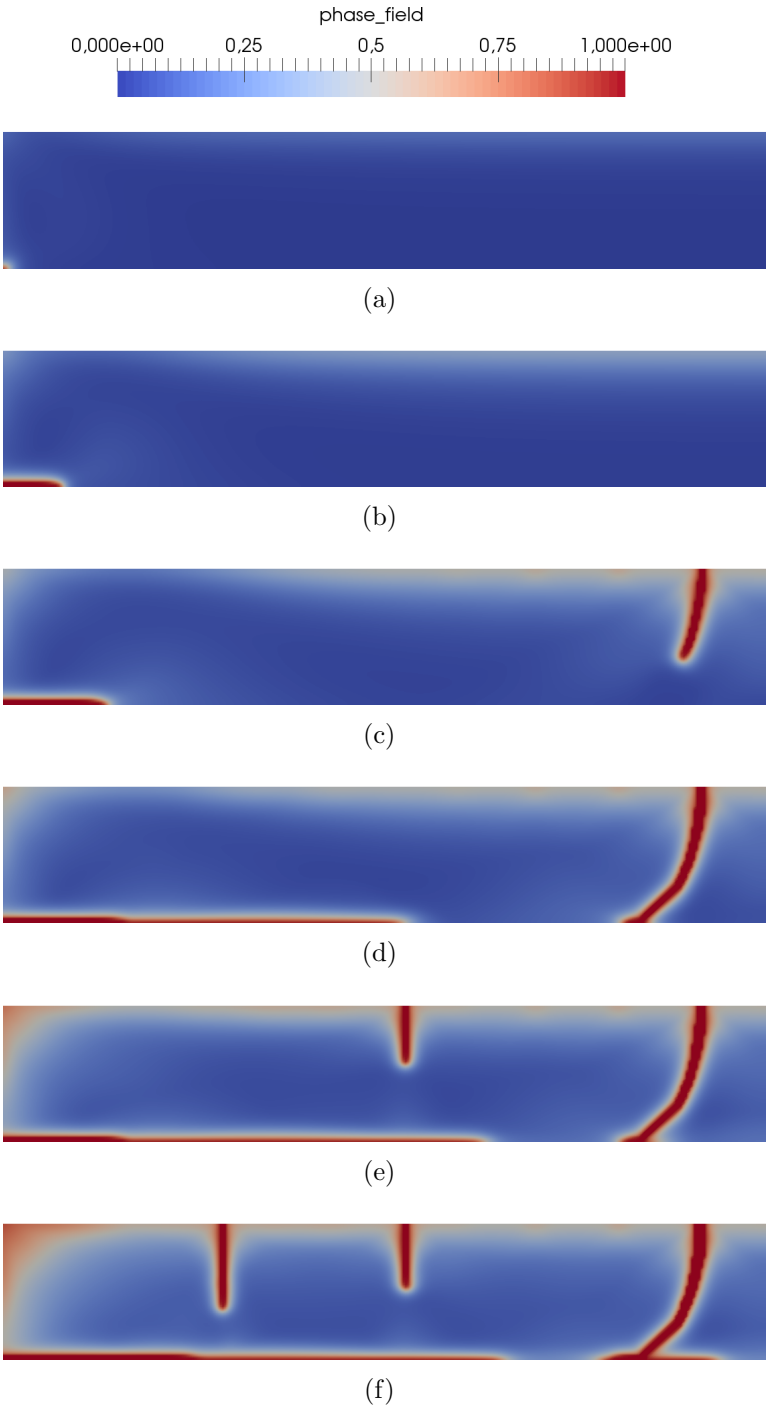


**Figure 5.7:** Phase-field evolution in the reference specimen subject to drying flux $\bar{q} = 6 \times 10^{-7}$ m/s. At (a) $t = 15$ minutes, the phase-field distribution is uniform on the surface and the crack at the corner initiated. Further propagation of the crack at the corner is observed at (b) $t = 30$ minutes. Drying crack onset is registered at $t \approx 44$ minutes. Specimen at (c) 45 minutes, (d) 60 minutes, (e), 90 minutes and (f) 120 minutes.

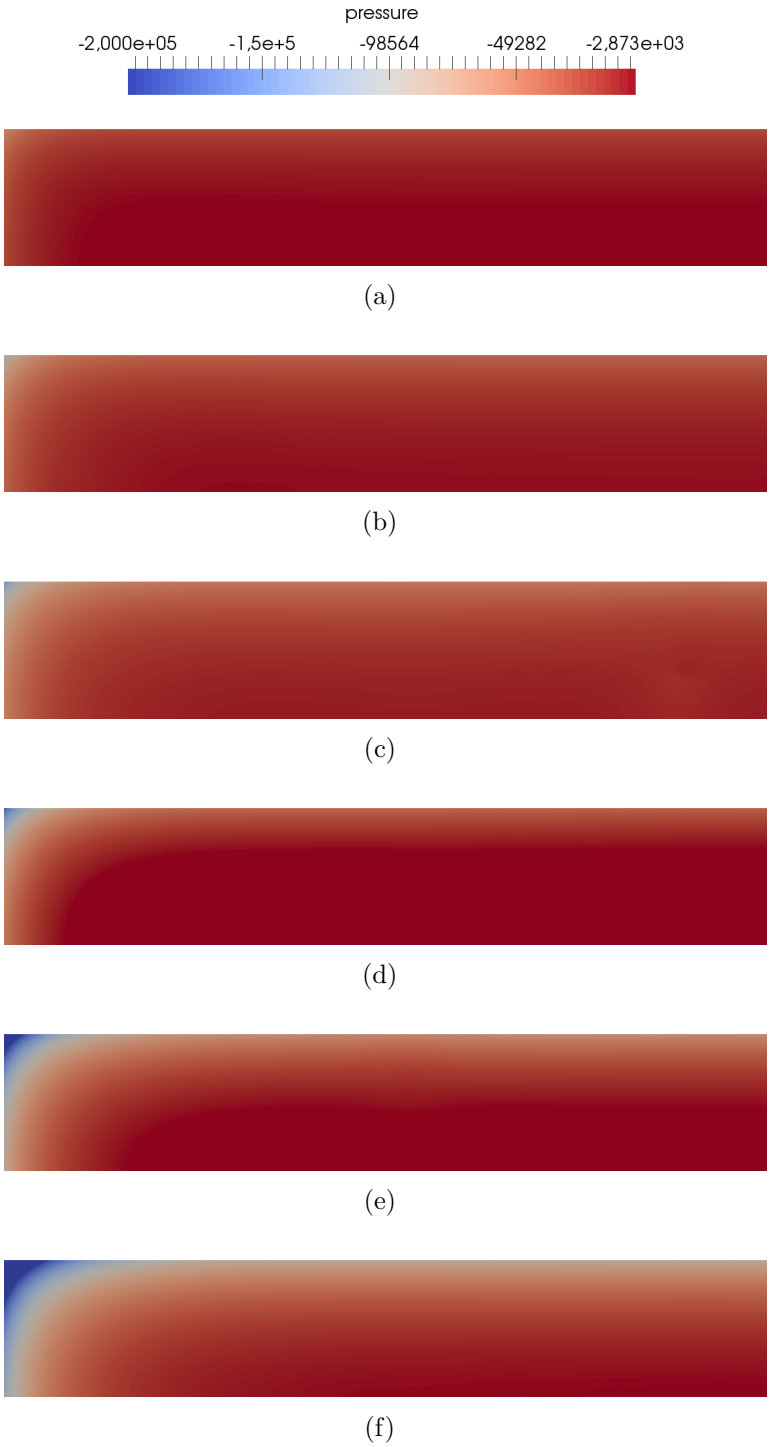


**Figure 5.8:** (a) Water pressure $[Pa]$ distribution in the reference specimen subject to drying flux $\bar{q} = 6 \times 10^{-7}$ m/s at $t = 15$ minutes, (b) 30 minutes, (c) 45 minutes, (d) 60 minutes, (e) 90 minutes and (f) 120 minutes.

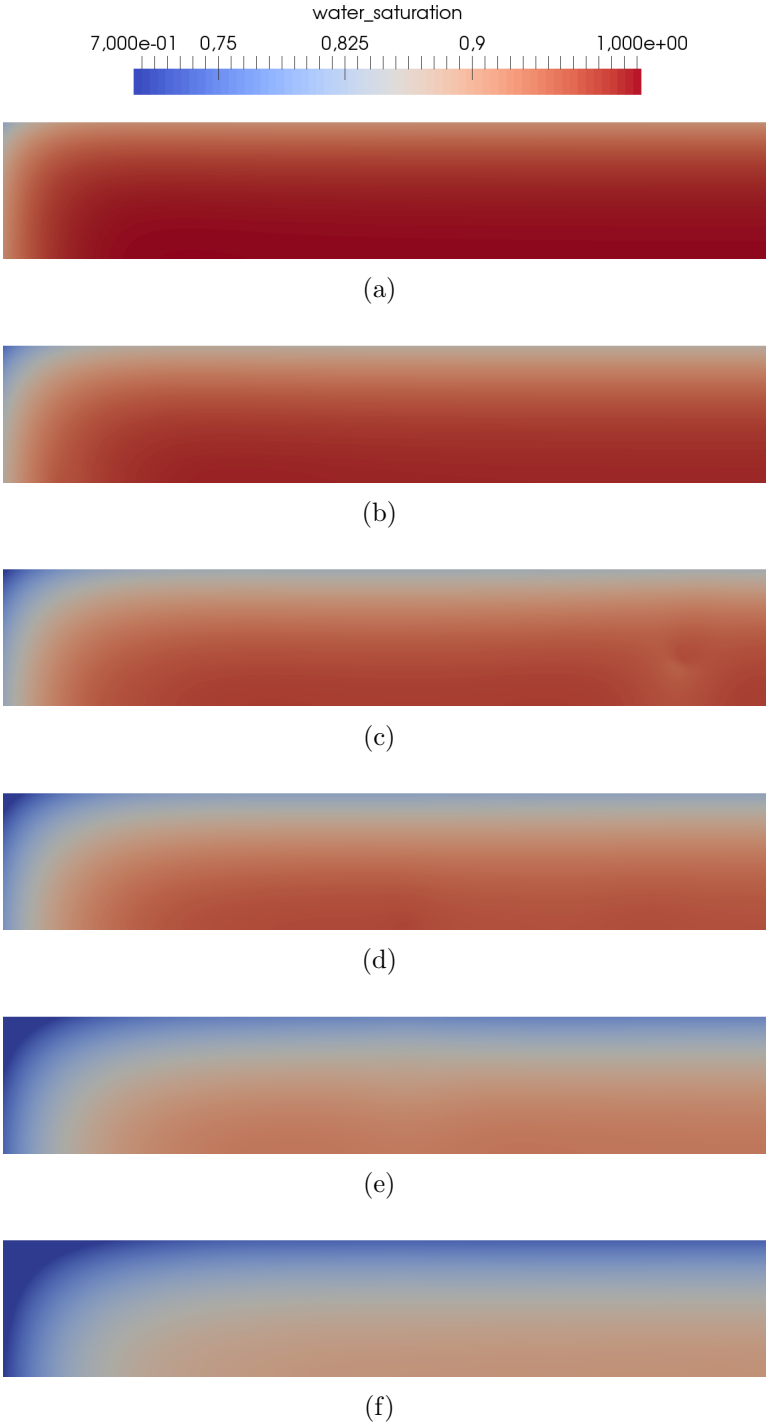


**Figure 5.9:** Water saturation distribution in the reference specimen subject to drying flux $\bar{q} = 6 \times 10^{-7}$ m/s at (a) $t = 15$ minutes, (b) 30 minutes, (c) 45 minutes, (d) 60 minutes, (e) 90 minutes and (f) 120 minutes.

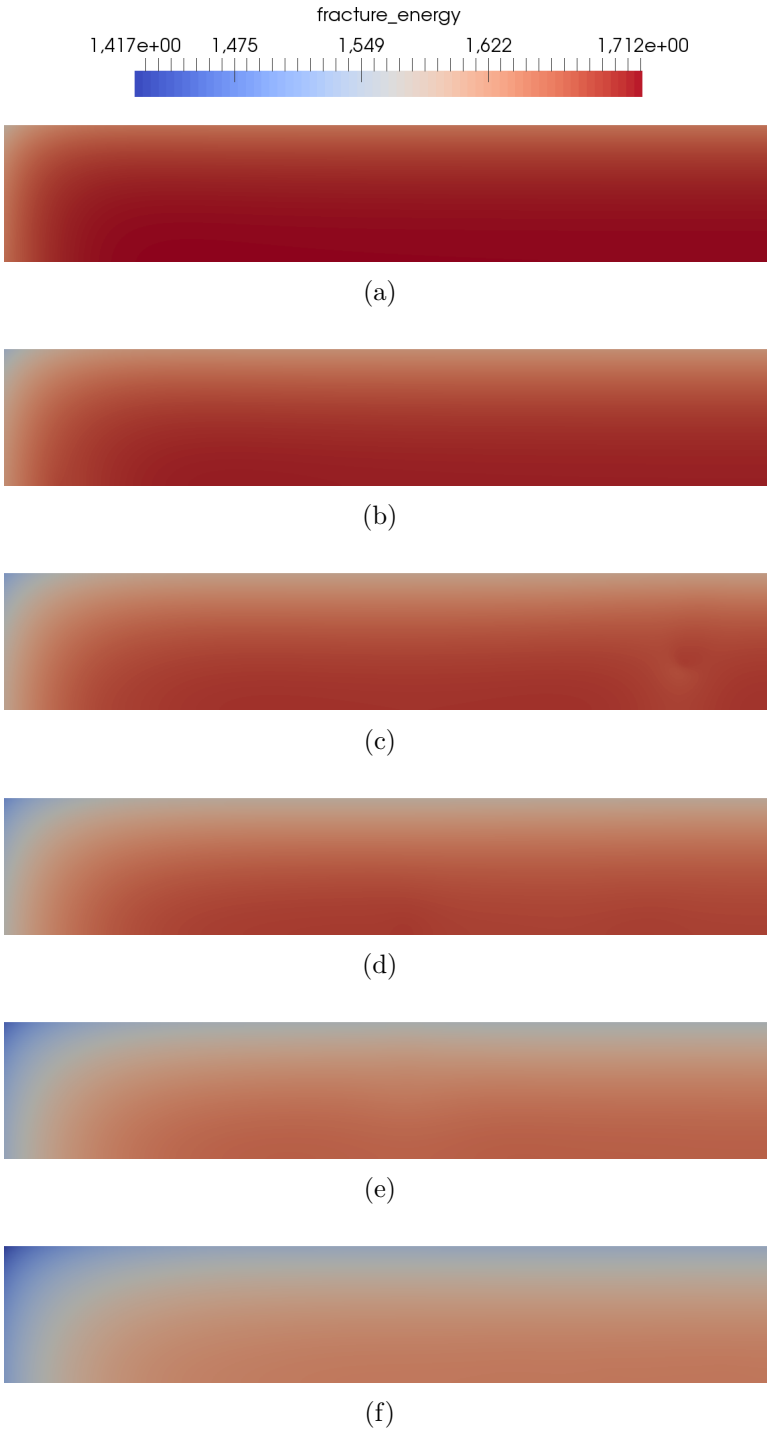


**Figure 5.10:** Fracture energy $[N/m]$ distribution in the reference specimen subject to drying flux $\bar{q} = 6 \times 10^{-7}$ m/s at (a) $t = 15$ minutes, (b) 30 minutes, (c) 45 minutes, (d) 60 minutes, (e) 90 minutes and (f) 120 minutes.

### 5.2.3 Sensitivity of the numerical solution

In the following, we present the results of additional numerical simulations, which aim at evaluating how the choice of fracture energy, dry density, permeability and boundary conditions affects the results.

#### Influence of the fracture energy

As shown in Eq. (3.4.12), the length scale parameter is related to the material properties (fracture energy, tensile strength and elastic modulus). As we decided to keep $\ell$ constant and consider $\sigma_t$ and $E$ as functions of $w$ only, the fracture energy turns out to increase linearly with $\ell$ (Eq. (3.4.13). Furthermore, the width of the regularization zone proportionally increases with $\ell$.

The results of the constrained desiccation test are shown when the length scale parameter is increased to $\ell = 0.004$m, so that the fracture energy for a given $\ell$ is doubled. As expected, the crack at the upper drying surface occurs later in comparison to the reference case with $\ell = 0.002$m, Figs. 5.7(a)-5.7(d). This can be observed in Figs. 5.11(a)-5.11(d). Furthermore, the transition zone is wider. The upper crack propagates vertically and then curves, Fig. 5.11(d). After approximately 95 minutes from the beginning of the test, it is observed that the crack at the corner and the upper crack propagate further, Figs. 5.11(e). A second crack from the upper drying surface is observed and the propagation of the crack at the corner is slower in comparison to the reference test, Fig. 5.11(f).

#### Influence of the mechanical restraint

Péron [121] observed cracks at the corner of his specimens and attributed them to the mechanical restraint. There is no reference to such cracks in Stirling's work, probably because the sides of the specimen are hidden. The aim of this section is to analyze the occurrence of cracking at the corner of the specimen in relation to the type of mechanical restraint at the bottom. In the following test, as in the reference test, the vertical component of the displacement of all nodes at the bottom is restrained. However, in the horizontal direction now only one node (lowest left node) is restrained to avoid rigid body motion and all other nodes are left free.

The parameters from Table 5.2 are used. This case can be interpreted as an ideal model with no friction on the bottom surface of the mould. Figure 5.12 shows the results of this test case. The horizontal shrinkage is larger leading to a different stress distribution in comparison to the fully constrained simulation. On the other hand, the vertical shrinkage is slightly smaller. The suction increases and consequently the horizontal stresses increase. The region with uniform stress field is prone to phase-field evolution. Although the phase-field does not localize up to 60 minutes, it is possible to recognize

its slight uniform increase on the upper layer, Fig. 5.12(a)-5.12(d). Localization occurs close to the left end of the specimen due to larger strain development 70 minutes after the start of the test. Figure 5.12(e) shows the developed crack at 90 minutes. This first crack propagates and approximately 23 minutes later, the onset of a second crack is observed. The third crack appears shortly after between the first two cracks, Fig. 5.12(f). A fourth crack initiates at the symmetry line approximately at 115 minutes and propagates further. The crack at the corner of the specimen does not initiate, confirming that the occurrence of such cracks is related to the mechanical horizontal restraint at the bottom of the specimen. It is also important to note that in this test case none of the cracks propagates through the specimen.

### Influence of the drying flux

Here we perform a numerical test applying a higher drying flux $\bar{q} = 1 \times 10^{-6}$m/s. The phase-field distribution at different time steps is shown in Fig. 5.13. It is possible to observe an increase of the number of secondary cracks with respect to the reference case solved with a lower flux ($\bar{q} = 6 \times 10^{-7}$m/s), which is in agreement with the observations from Stirling [144].

At 15 minutes from the start of the test, cracking at the corner of the specimen is observed, Fig. 5.13(a). After 20 minutes of drying, two small cracks are initiated at the upper surface and one lower crack is visible. Shortly after, one main crack propagates further. At 25 minutes, this main crack and three other secondary cracks are present along with a larger crack at the corner than in the reference test at the same time step, Figs. 5.13(b) and 5.13(c). The crack at the corner does not propagate further. At 45 minutes, the first main crack has almost completely propagated, Fig. 5.13(c), while with lower flux the first vertical cracks had appeared at about 44 minutes. Further cracks appear and propagate until three main cracks are visible in Fig. 5.13(d) and 5.13(e). The degradation of the left extremity of the specimen is also observed at 90 minutes and its region extends further until the end of the test. Figure 5.13(f) denotes a very advanced stage of the simulation where the specimen has failed and is only reported for consistency with the other figures. In summary, the higher flux leads to an earlier appearance of cracks and to a more extensive cracking. Also, it favors the crack propagation from the upper surface over the corner crack.

### Step-wise application of the drying flux

The next numerical example simulates an experimental desiccation test where the specimen is inserted in a compartment [87]. In this case, only the upper surface of the specimen is allowed to dry and only after the occurrence of lateral shrinkage the specimen loses water from the sides. To model this test we introduce the idea of step-wise drying flux. First, a drying flux is imposed at the upper surface of the specimen and, when lateral shrinkage is observed ($t \approx 60$ minutes), a second drying flux is applied to

the lateral sides of the sample.

Comparing the results of this simulation with the results from the reference test, we notice that the extension of the crack at the corner diminishes. At $t \approx 44$min, this extension corresponds to less than half of that observed in the standard test, Fig. 5.14(a). The phase-field at the upper surface localizes 10 seconds later in comparison to the reference case and the location of this crack is shifted to the left. This can be explained due to the smaller extension of the crack at the corner leading to a different stress distribution along the specimen. Shortly before 1 hour of test, the crack has fully propagated through the specimen, Fig. 5.14(c)-5.14(d). At approximately 80 minutes, a second crack starts at the upper surface. The crack at the corner and the first crack propagate further as shown in Fig. 5.14(e)-5.14(f).

### Influence of the intrinsic permeability

The intrinsic permeability is a material property that varies in a wide range due to the grain structure and the compaction processes of the experimental tests. In reality, there is a link between the permeability and the saturation, e.g. lower permeability means smaller pores and this would affect the saturation and increase the pore pressure. The material properties are coupled through the microstructure, i.e. changing one of them at a time is somewhat artificial. For the purpose of the sensitivity study and of understanding the influence of the variation of the intrinsic permeability on cracking, we perform three case studies taking the values $k_i = \{0.5, 1, 10\} \times 10^{-15}\text{m}^2$. The intermediate value was already used in the reference test described in Section 5.2.2.

In a material with higher permeability, the water flows more easily in comparison to a material with lower permeability and, consequently, the pressure gradients are lower. Smaller permeability leads to larger pressure gradients which are expected to accelerate cracking.

Figure 5.15 shows the distributions of the water pressure (a) and horizontal stress (b) along the upper surface at 15 and 30 minutes. The higher the permeability, the higher the value of the water pressure. The water pressure increases in absolute value with time. The horizontal stress distribution follows the opposite tendency as shown in Fig. 5.15(b). The lower the permeability, the higher the value of the horizontal stress. At 15 minutes, a positive uniform horizontal stress distribution is observed. The stress increases with time for the specimens with $k_i = \{0.5, 1\} \times 10^{-15}\text{m}^2$. On the other hand, since the specimen with higher permeability suffers early detachment from the bottom, the stress decreases, becomes negative and no main cracking is expected to occur. This condition is comparable to a free desiccation test, where no cracks initiating on the upper surface are observed in the experiments. The crack at the corner of the specimen and its propagation with time can be confirmed in Fig. 5.16.

We expect a larger number of cracks in the specimen with the lowest permeability $k_i = 0.5 \times 10^{-15}\text{m}^2$. Here, the pressure gradients within the specimen are higher,

corresponding to a desiccation crust in the specimen. Already after 30 minutes from the start of the test, several localization areas can be observed, Fig. 5.17(a). From these, two cracks emerge, Fig. 5.17(b). The two cracks propagate further along the specimen and we observe a third localization area at 48 minutes. The three cracks propagate together and more localization areas are observed, Fig. 5.17(d) and 5.17(e). A total of six cracks is registered after the first hour, Fig. 5.17(f). It can be observed that the crack at the corner is a secondary crack that does not extend after the onset of the first crack. The crack at the extremity of the specimen propagates further due to high pressure in this region.

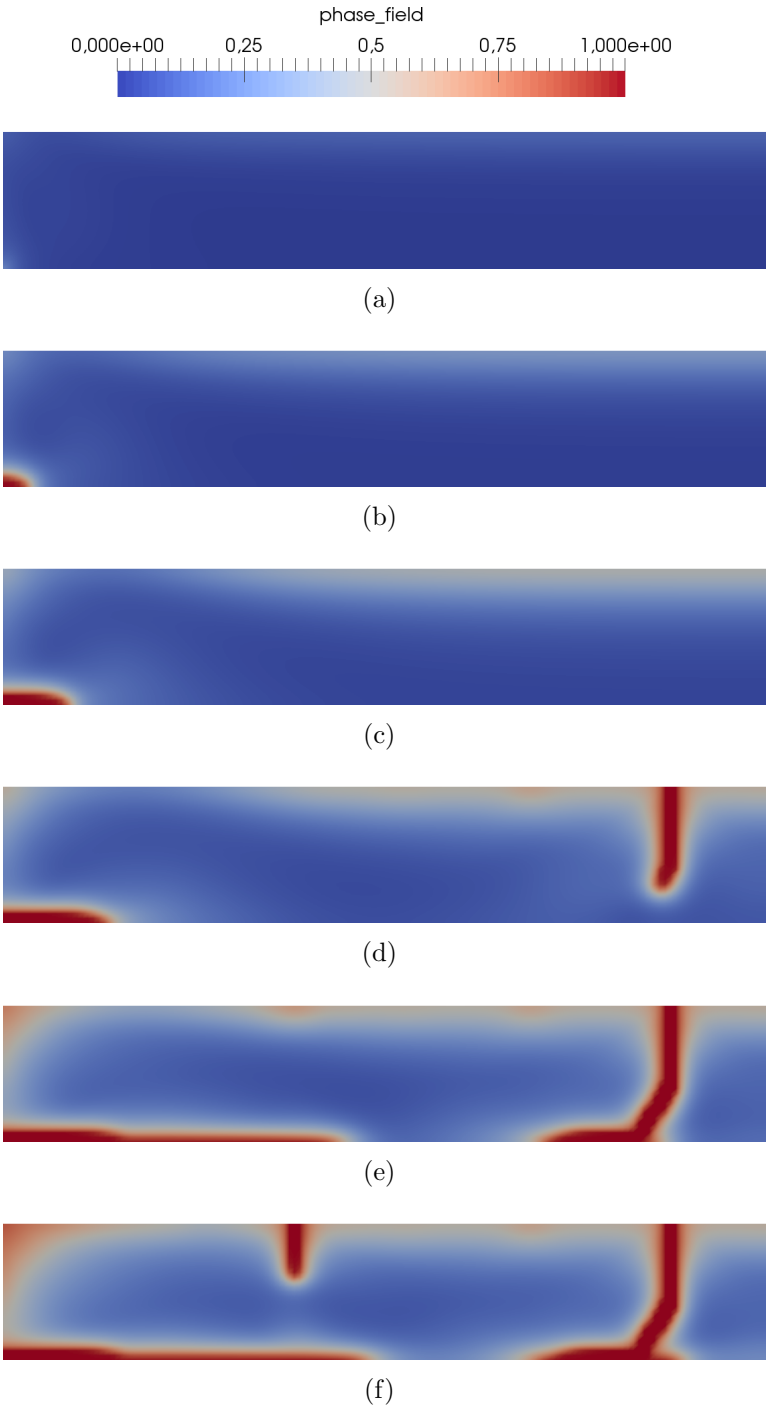


**Figure 5.11:** Phase-field evolution in the specimen with $\ell = 0.004$m, subjected to drying flux $\bar{q} = 6 \times 10^{-7}$ m/s at (a) $t = 15$ minutes, (b) 30 minutes, (c) 45 minutes, (d) 60 minutes, (e) 90 minutes and (f) 120 minutes. The first surface crack is observed at $t \approx 52$ minutes.

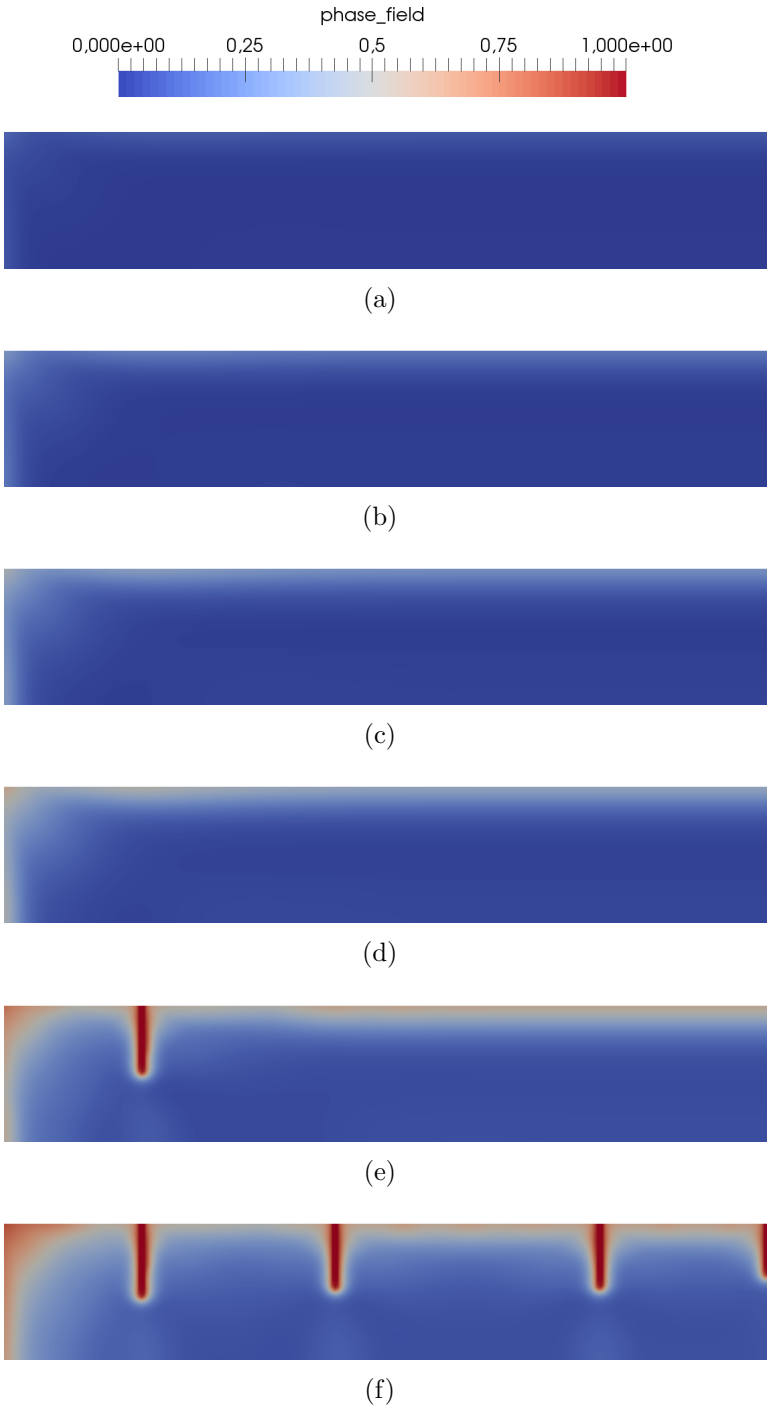


**Figure 5.12:** Phase-field evolution in the single point restrained specimen configuration at (a) $t = 15$ minutes, (b) 30 minutes, (c) 45 minutes, (d) 60 minutes, (e) 90 minutes, and (f) 120 minutes. The first surface crack is observed at $t = 70$ minutes.

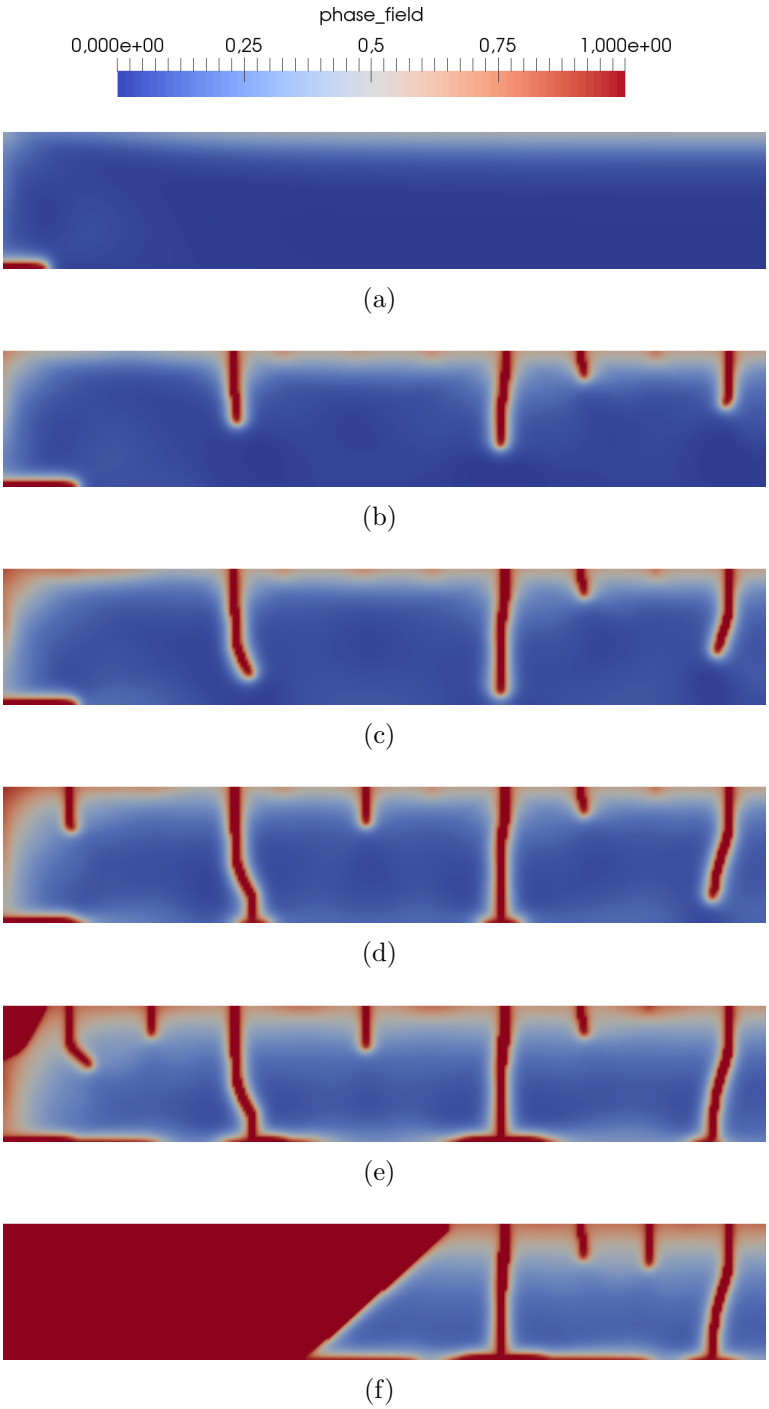


**Figure 5.13:** Phase-field evolution in the specimen with high drying flux $\bar{q} = 1 \times 10^{-6}$ m/s at (a) $t = 15$ minutes, (b) 30 minutes, (c) 45 minutes, (d) 60 minutes, (d) 90 minutes (f) and 120 minutes. The first surface crack is observed at $t \approx 20$ minutes.

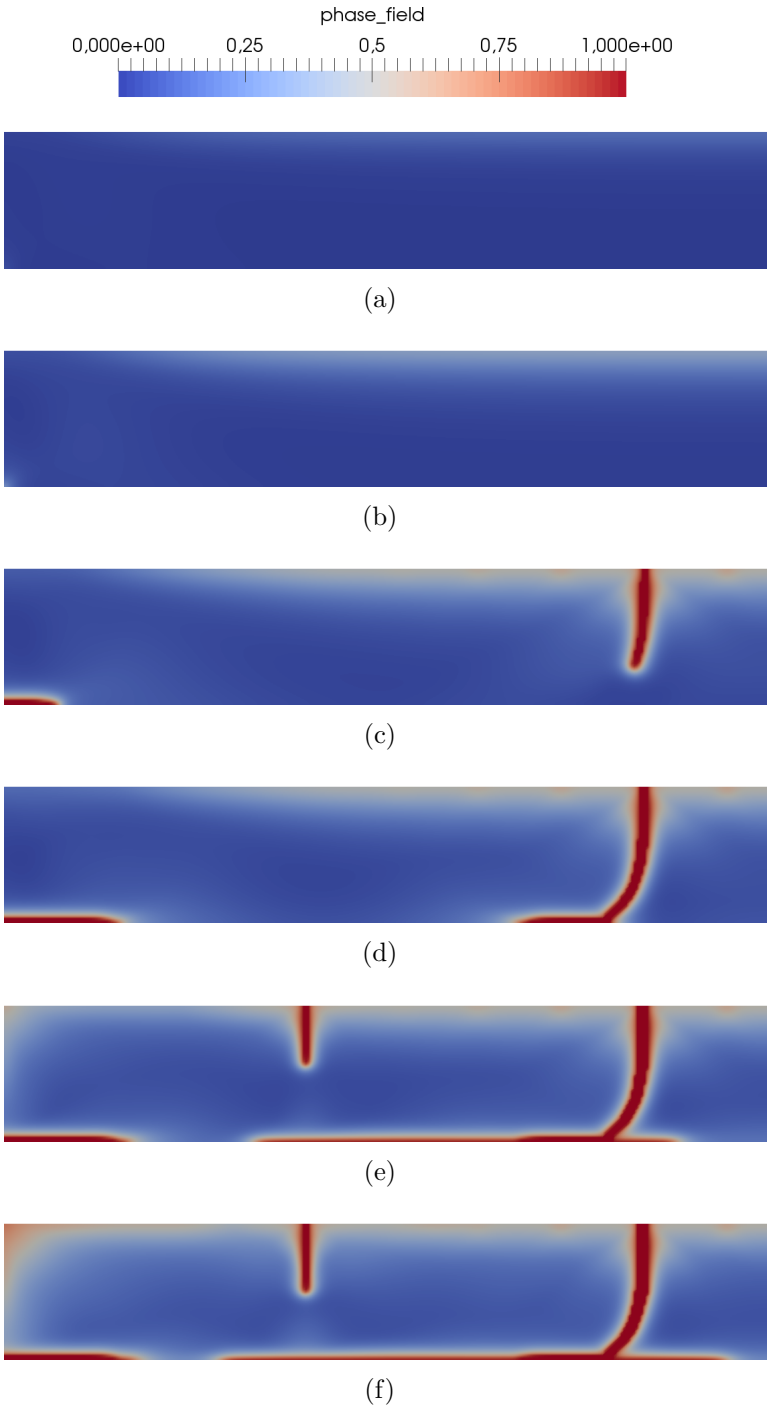


**Figure 5.14:** Phase-field evolution in the specimen with step-wise applied drying flux $\bar{q} = 6 \times 10^{-7}$ m/s at (a) $t = 15$ minutes, (b) 30 minutes, (c) 45 minutes, (d) 60 minutes, (e) 90 minutes and (f) 120 minutes. The first surface crack is observed at $t \approx 44$ minutes.

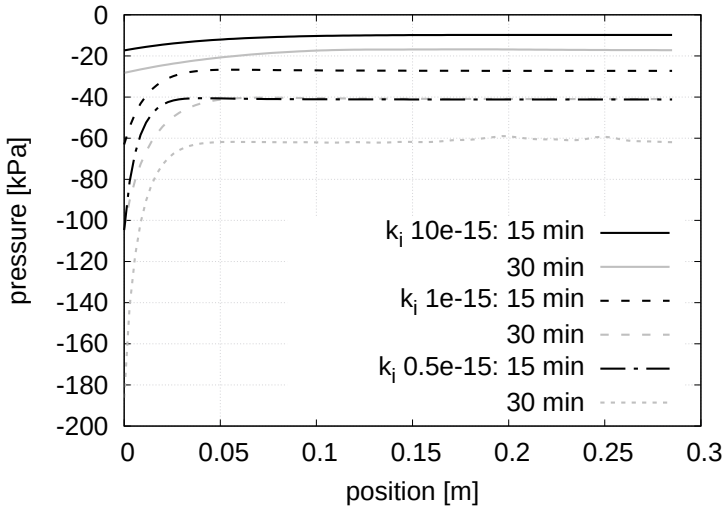


(a)

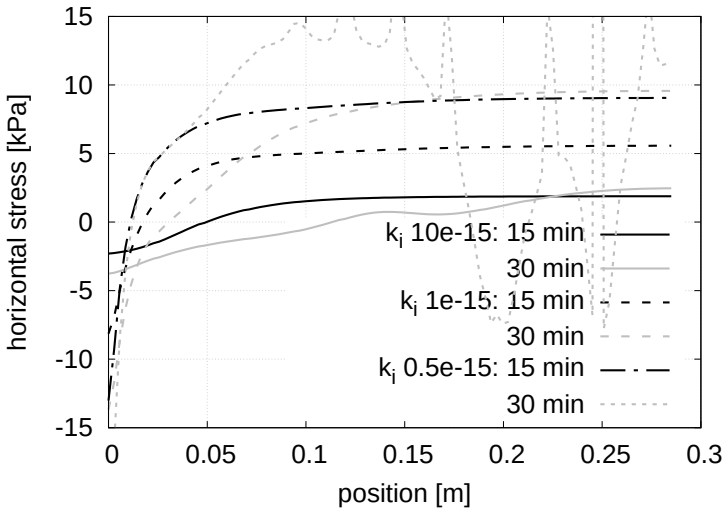


(b)

**Figure 5.15:** (a) Pressure and (b) horizontal stress distribution along the upper surface at 15 and 30 minutes with $k_i = \{0.5, 1, 10\} \times 10^{-15}\text{m}^2$.

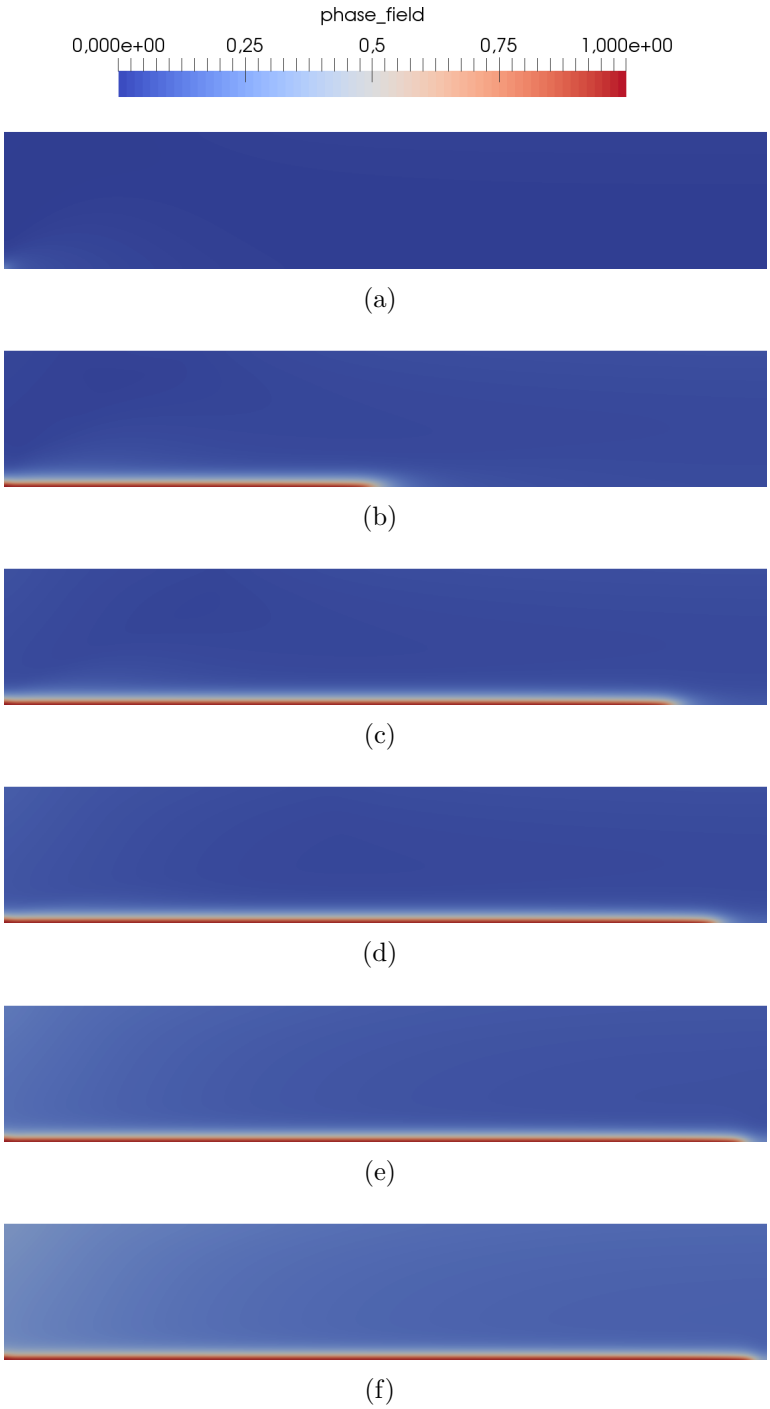


**Figure 5.16:** Phase-field evolution in the specimen with intrinsic permeability $k_i = 10 \times 10^{-15}\text{m}^2$ and drying flux $\bar{q} = 6 \times 10^{-7}$ m/s at (a) $t = 15$ minutes, (b) 30 minutes, (c) 45 minutes, (d) 60 minutes, (e) 90 minutes and (f) 120 minutes. A crack initiates and propagates only at the bottom of the specimen.

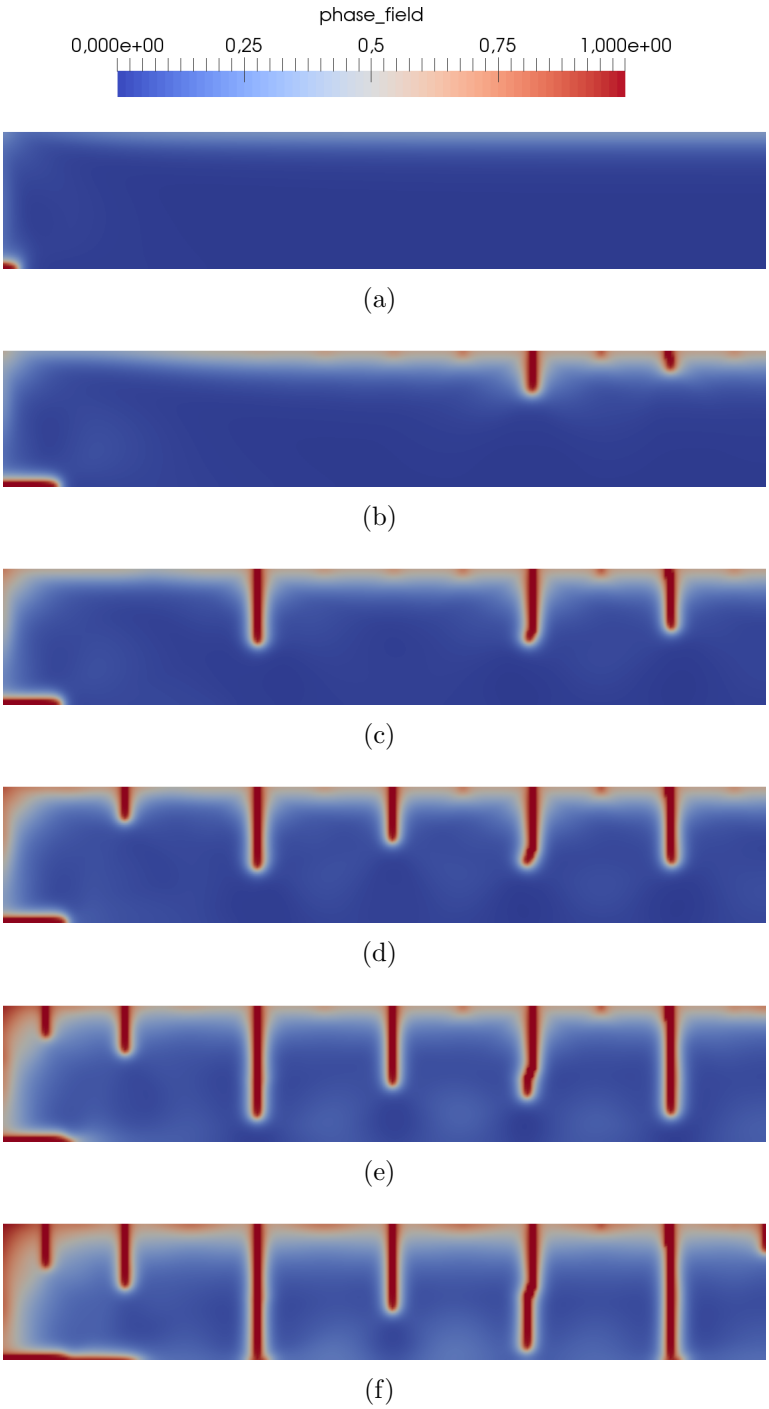


**Figure 5.17:** Phase-field evolution in the specimen with intrinsic permeability $k_i = 0.5 \times 10^{-15}\text{m}^2$ and drying flux $\bar{q} = 6\times10^{-7}$ m/s at (a) $t = 15$ minutes, (b) 30 minutes onset of first upper crack, (c) 45 minutes, (d) 60 minutes, (e) 90 minutes and (f) 120 minutes. The crack at the corner of the specimen remains limited.

### 5.2.4 Further numerical tests

The possibility of using adaptive mesh refinement and the influence of the number of staggered iterations are investigated. Furthermore, the effect of the crack phase-field on the pore water pressure field is evaluated and the coupling is commented on.

#### Adaptive mesh refinement computations

In order to assess the accuracy of the numerical solution, adaptive computations are carried out. Adaptive mesh refinement schemes for multi-field problems such as mechanical-fracture and poromechanical problems are available in the literature [64, 73]. However, they need to be adapted and implemented in the framework described in this thesis.

With the aim of preliminary testing, an adaptive scheme available in the `deal.II` library is adopted. The scheme is based on the so-called Kelly estimator and was developed for the Laplace equation [47, 12]. The main idea is to apply this error estimator to one of the unknown fields $\mathbf{u}$-$p_w$-$d$.

Due to the dominance of the water pressure in the coupled problem of this thesis (see discussion in Section 5.2.2 and Figs. 5.8 and 5.9), the error estimator is applied to this unknown. Furthermore, it can be observed that the water pressure varies largely not only along the specimen due to drying but also around the cracked regions as shown in Fig. 5.18. This may be a reasonable strategy, since the evolution of the water pressure also induces the evolution of the crack.

The built-in error estimator and adaptive scheme are used to re-compute the reference test of Section 5.2.2. Since the flux is applied at the upper surface and large pressure changes are expected nearby, the mesh is adaptively refined close to the drying surface. These elements reach the required element length $h = \ell/2$ on the first refinement. A region with homogeneous phase-field distribution is observed at early stages before its localization. Apart from the crack at the corner of the specimen, crack initiation and propagation are observed at the same times computed in the fixed mesh, Fig. 5.7 and 5.19 for comparison. This simulation shows good agreement and runs with half computational time in comparison to the simulation with fixed, pre-refined mesh. Better computational efficiency can be achieved with the use of an adaptive scheme implemented in the context of the coupled problem.

#### Number of staggered iterations

In order to check the accuracy of the results reported in Section 5.2, which are obtained using an explicit staggered approach, the reference test and the test case with $k_w = 0.5 \times 10^{-15}\mathrm{m}^2$ were recomputed with 10 staggered iterations. The comparison

with the explicit results (Figures 5.7 and 5.17) in Figs. 5.20 and 5.21 show that the phase-field evolution is not strongly affected by the number of staggered iterations.

### Influence of the crack field on the pressure field

The reference specimen in Section 5.2.2 is further analyzed with respect to the influence of the crack on the pressure field.

The pressure field develops uniformly on the upper drying surface during the calculations. When there is a chance for a crack to propagate, e.g. for $d > 0.5$, at approximately 43 minutes (2590 seconds), the pressure field becomes slightly non-uniform between 0.25 and 0.285 m as shown in Fig. 5.22(a), see the zoom in the relevant region in 5.22(b). The increase of the phase-field is associated with further non-uniformity of the pressure field. Once the crack fully propagates between 43 and 44 minutes, the pore pressure near the damaged region broadens and later becomes uniform again (approximately 60 minutes). The same tendency is observed in later crack onset and on the crack propagation within the vertical layers of the mesh. This indicates that the crack phase-field does affect the pressure field although the coupling between these two fields is only indirect.

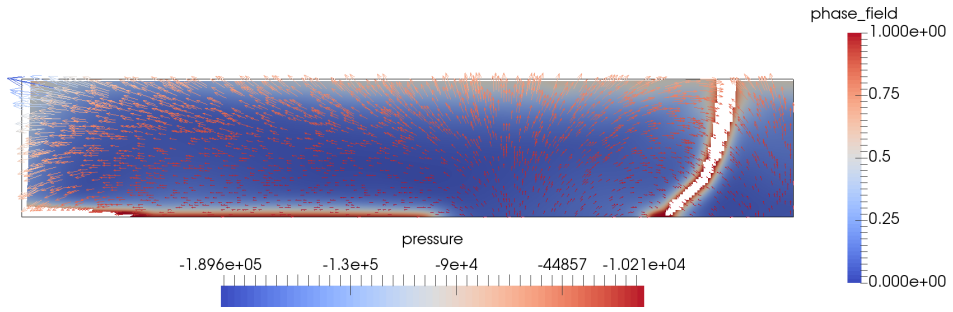


**Figure 5.18:** Deformed specimen with projected pressure distribution (arrows). The fully damaged zones are filtered in the figure. The pressure varies widely around the cracked zones and drying surfaces.

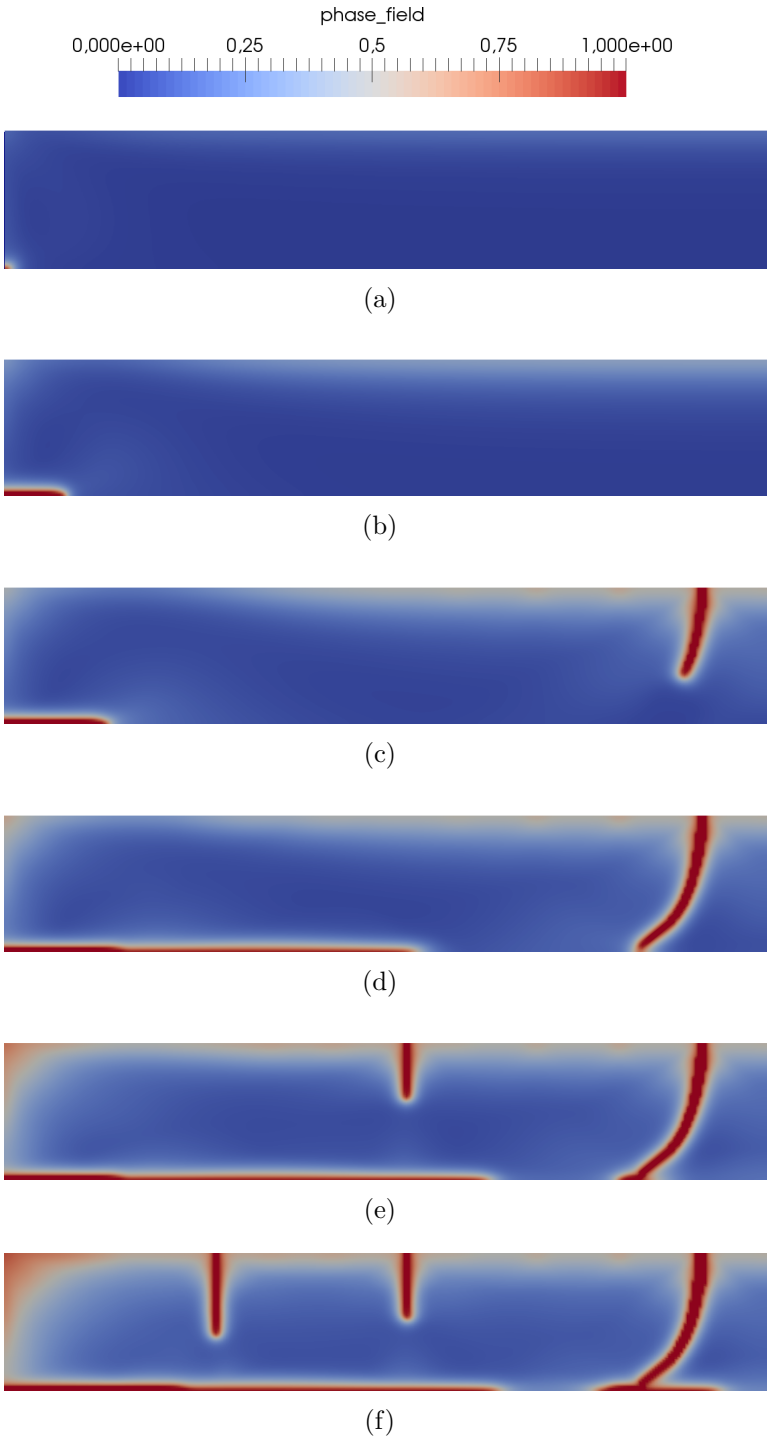


**Figure 5.19:** Phase-field evolution with adaptive mesh refinement in the reference specimen subject to drying flux $\bar{q} = 6 \times 10^{-7}$ m/s at $t = 15$ minutes (a) 30 minutes (b) 45 minutes (c) 60 minutes (d) 90 minutes (e) and 120 minutes (f). These results can be compared with the results in Fig. 5.7.

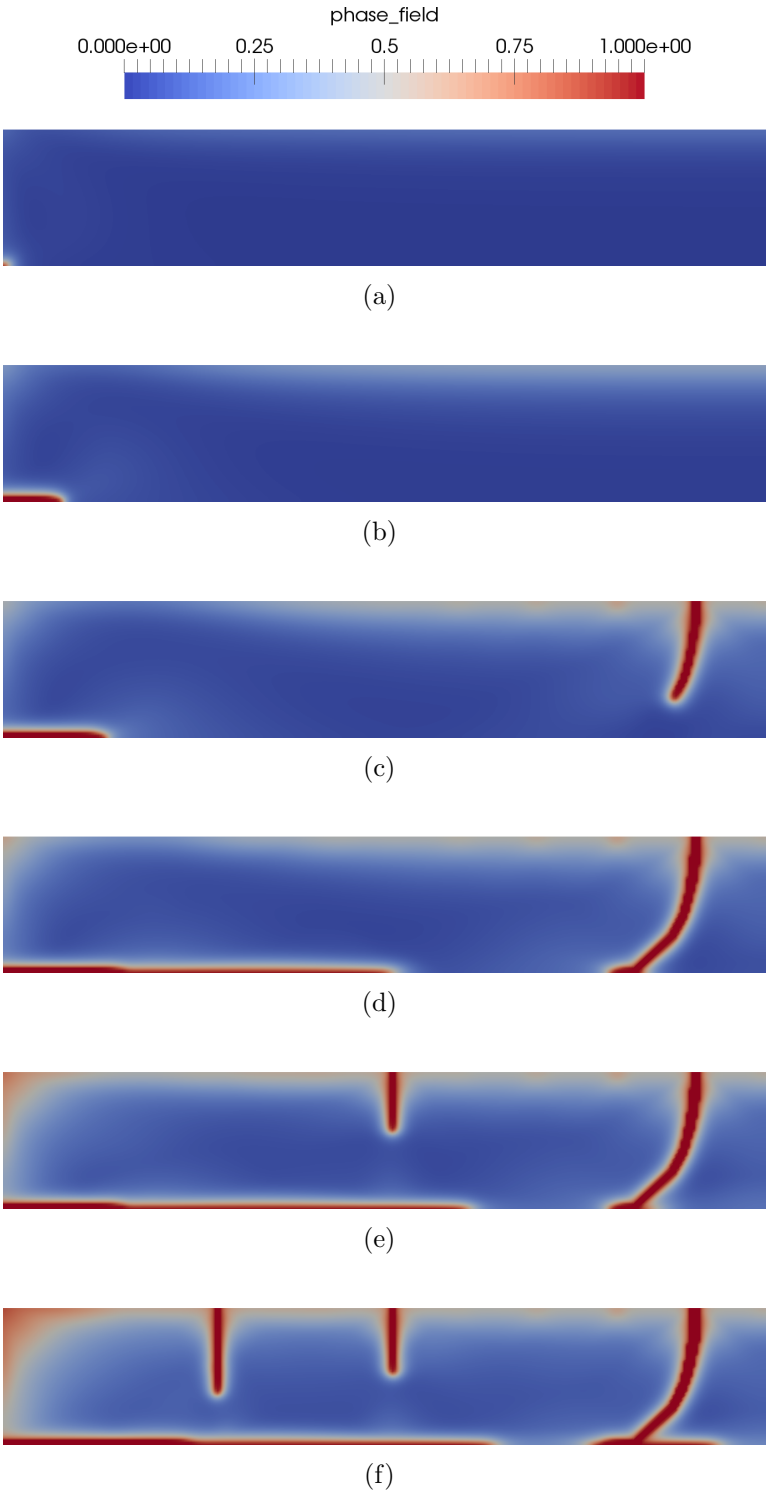


**Figure 5.20:** Phase-field evolution in the reference specimen subject to drying flux $\bar{q} = 6 \times 10^{-7}$ m/s computed with 10 staggered iterations at (a) $t$ =15 minutes, (b) 30 minutes, (c) 45 minutes, (d) 60 minutes, (e) 90 minutes and (f) 120 minutes. These results can be compared with the results in Fig. 5.7.

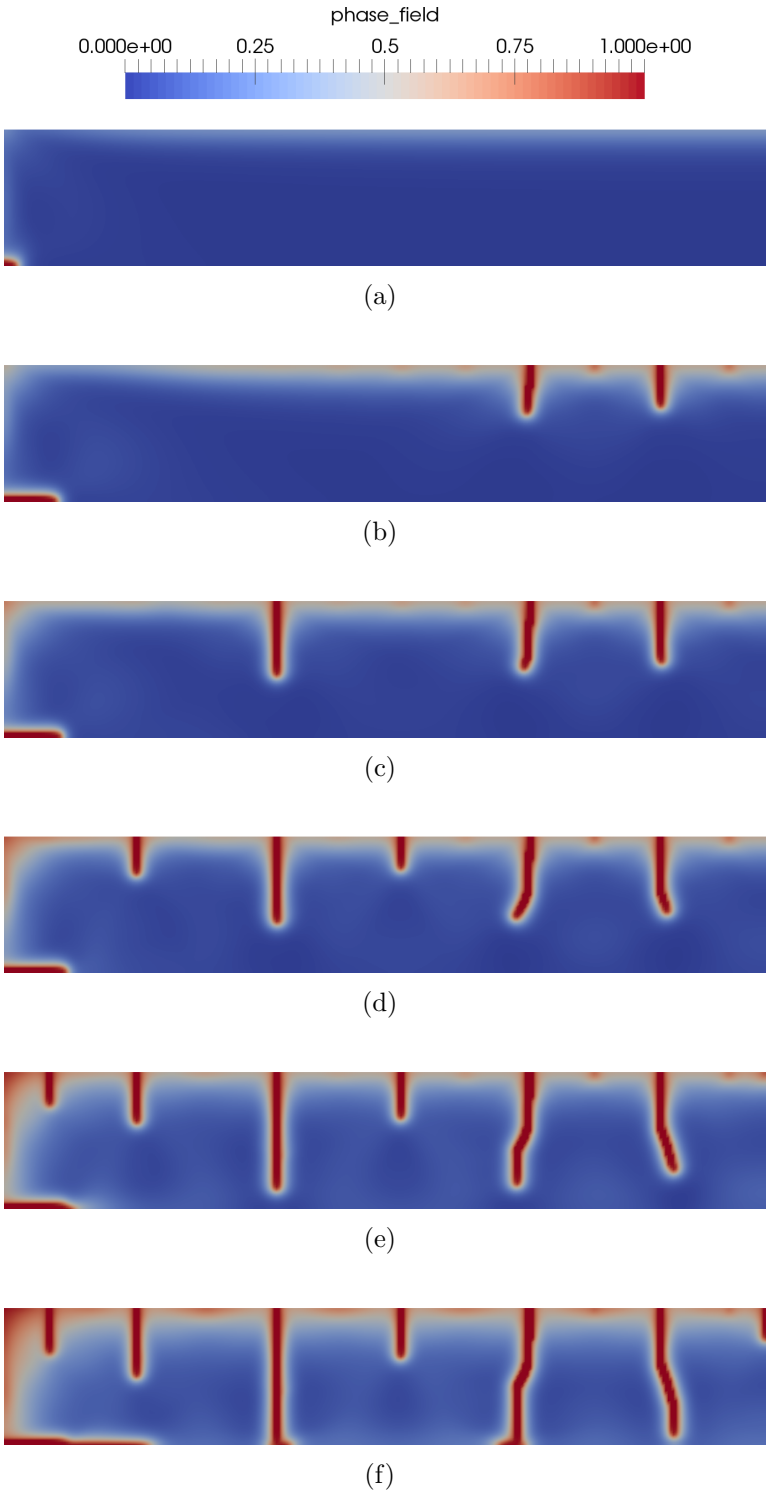


**Figure 5.21:** Phase-field evolution in the specimen with intrinsic permeability $k_i = 0.5 \times 10^{-15}\text{m}^2$ and drying flux $\bar{q} = 6 \times 10^{-7}$ m/s computed with 10 staggered iterations at (a) $t$ =15 minutes, (b) 30 minutes, (c) 45 minutes, (d) 60 minutes, (e) 90 minutes and (f) 120 minutes. These results can be compared with the results in Fig. 5.17.

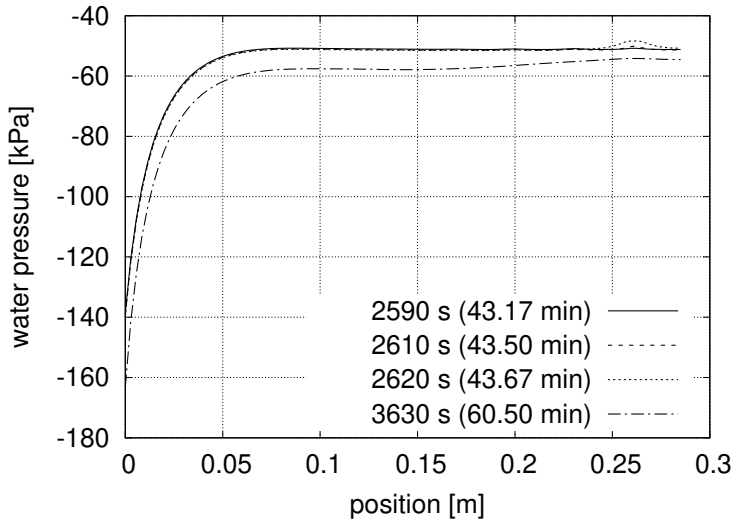


(a)

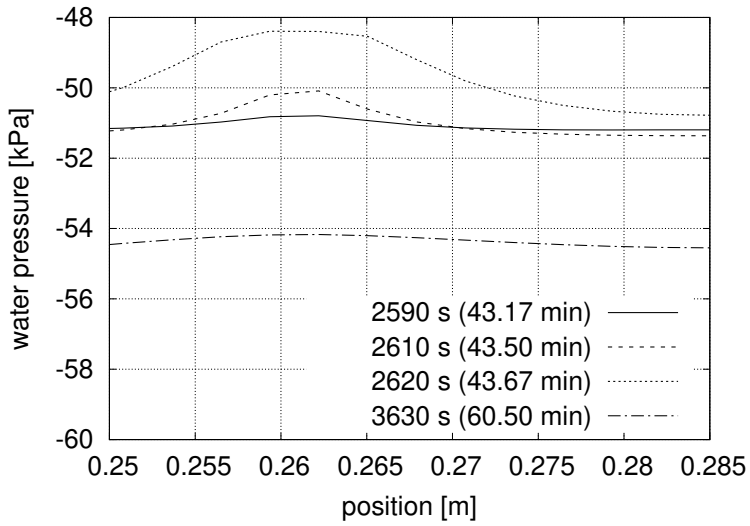


(b)

**Figure 5.22:** (a) Evaluation of the influence of the crack phase-field on the pressure development at the upper drying layer and (b) zoom in the region where the crack propagates.

## 5.3 Three-dimensional desiccation and crack patterns

The experimental setup of the following test is inspired by the thesis of [87], which focuses on the experimental study of three-dimensional crack patterns observed during soil desiccation. The work presents a large range of experimental samples with different

sizes and surface roughness.

The chosen setup consists in inserting clay into prismatic moulds with the dimensions of $210 \times 297 \times 10\text{mm}^3$. These samples are placed in a climatic chamber to dry. Several qualitative aspects regarding the temporal crack pattern evolution are reported in [87]. However, the material data and boundary conditions of the test are not presented in detail and are therefore insufficient to be used as input in the current framework. For this reason, the material data presented in Section 5.2 are used further as input in the following tests that aim at indicating the capability of the framework in predicting complex crack patterns in three-dimensional samples.

The model setup is shown in Fig. 5.23(a). The nodes located at the bottom surface are mechanically restrained in both of the following study-cases. Figures 5.23(b) and 5.23(c) show the mechanical and symmetry boundary conditions imposed in the free and restrained test cases, respectively. Moreover, a drying flux is applied on the upper surface of the samples. Fine meshes are associated with high computational costs due to assembly and solving procedures. A compromise is found by choosing a large length scale. The test value $\ell = 0.004\text{m}$ is assumed with $\Delta t = 1$ s.

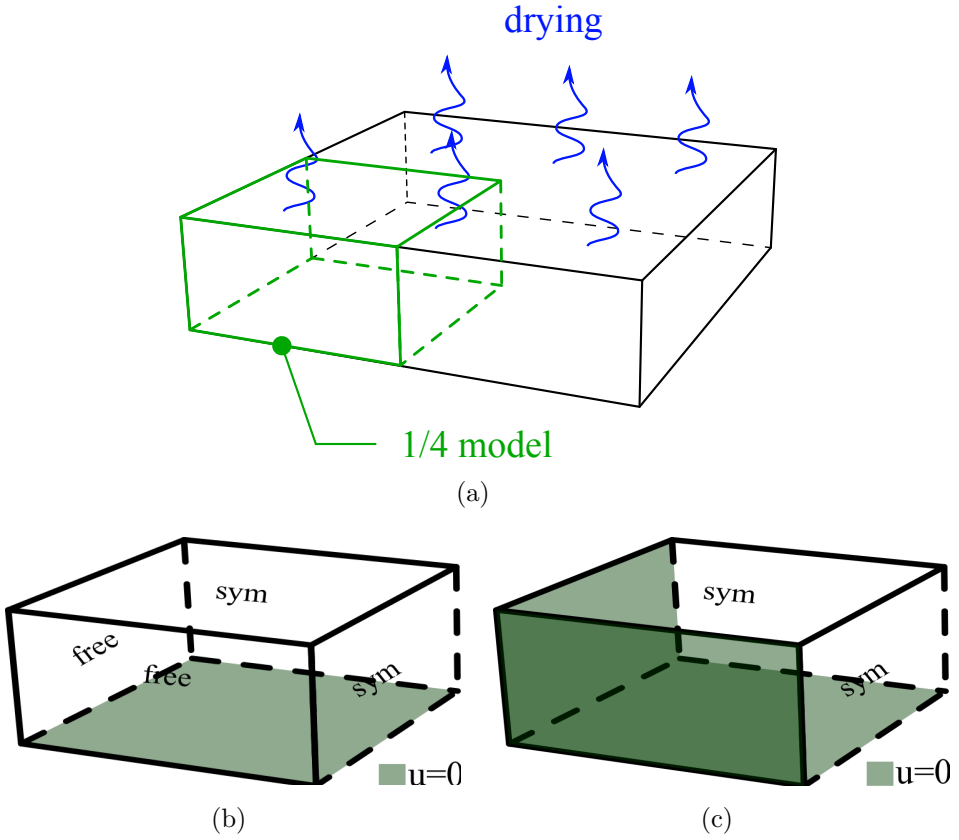


**Figure 5.23:** (a) Model for the experimental setup of three-dimensional desiccation test drying from the upper surface. The model is complemented with mechanical and symmetry boundary conditions in the (a) free sides configuration and (b) restrained sides configuration.

### 5.3.1 Free sides

The first test case with restrained bottom and free sides is shown in Fig. 5.23(b). The drying boundary condition is applied on the top of the sample. The pressure field increases approximately uniformly at the upper surface. On the sides of the sample, a pressure gradient can be identified, with maximum suction at the upper, drying surface and minimum suction at the bottom of the sample. Cracking occurs approximately at 23 minutes after the test starts near the symmetry edges. A third crack near the center of the sample initiates around 25 minutes. The surface cracks become stationary after 30 minutes and the bottom surface starts to detach. The temporal crack pattern evolution is shown in Fig. 5.24.

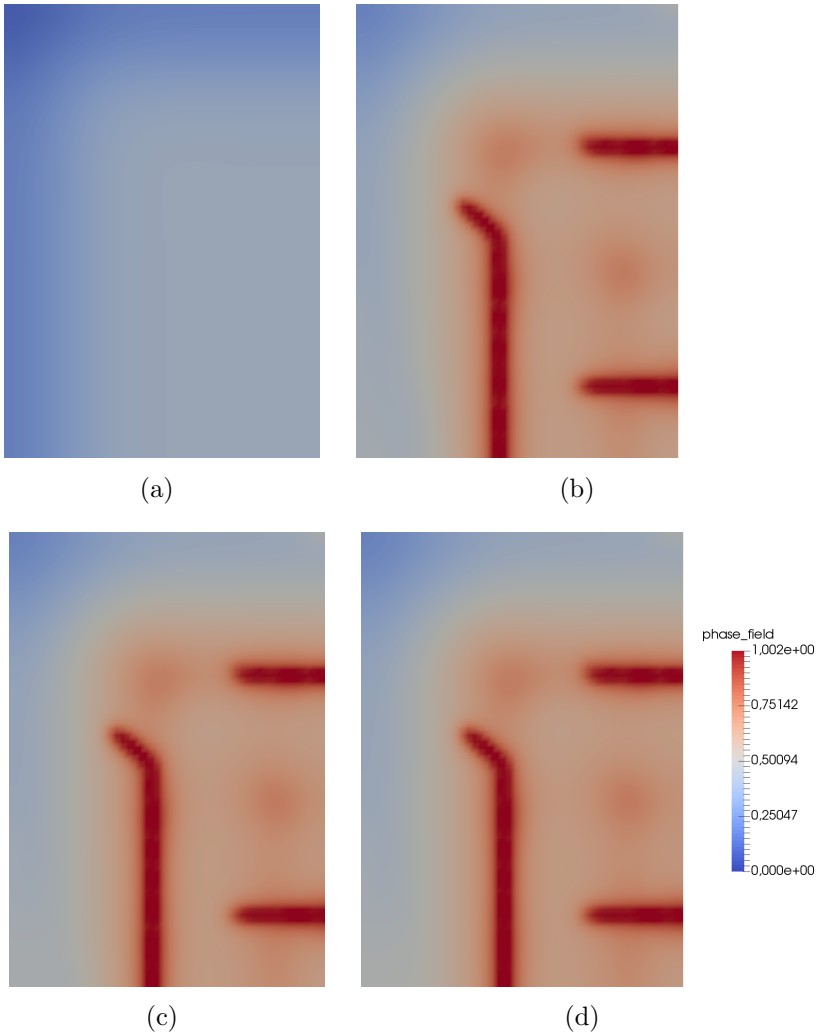


**Figure 5.24:** Top view of phase-field evolution in the three-dimensional specimen (free sides) with $\ell = 0.004$m, subjected to drying flux $\bar{q} = 6 \times 10^{-7}$ m/s at (a) $t = 15$ minutes, (b) 30 minutes, (c) 45 minutes, (d) 60 minutes. The first surface crack is observed at $t \approx 23$ minutes.

### 5.3.2 Restrained sides

Unlike in the first test case, the nodes on the sides of the sample are also restrained in the current configuration, Fig. 5.23(c). Surface cracks start to develop after 27 minutes from the start of the test. These propagate further and join each other between 30 and 45 minutes. Moreover, crack branching is observed. After 60 minutes, the surface cracks become stationary and bottom detachment is observed. The temporal crack evolution can be observed in Fig. 5.25. The pressure field evolves similarly to the previous test case.

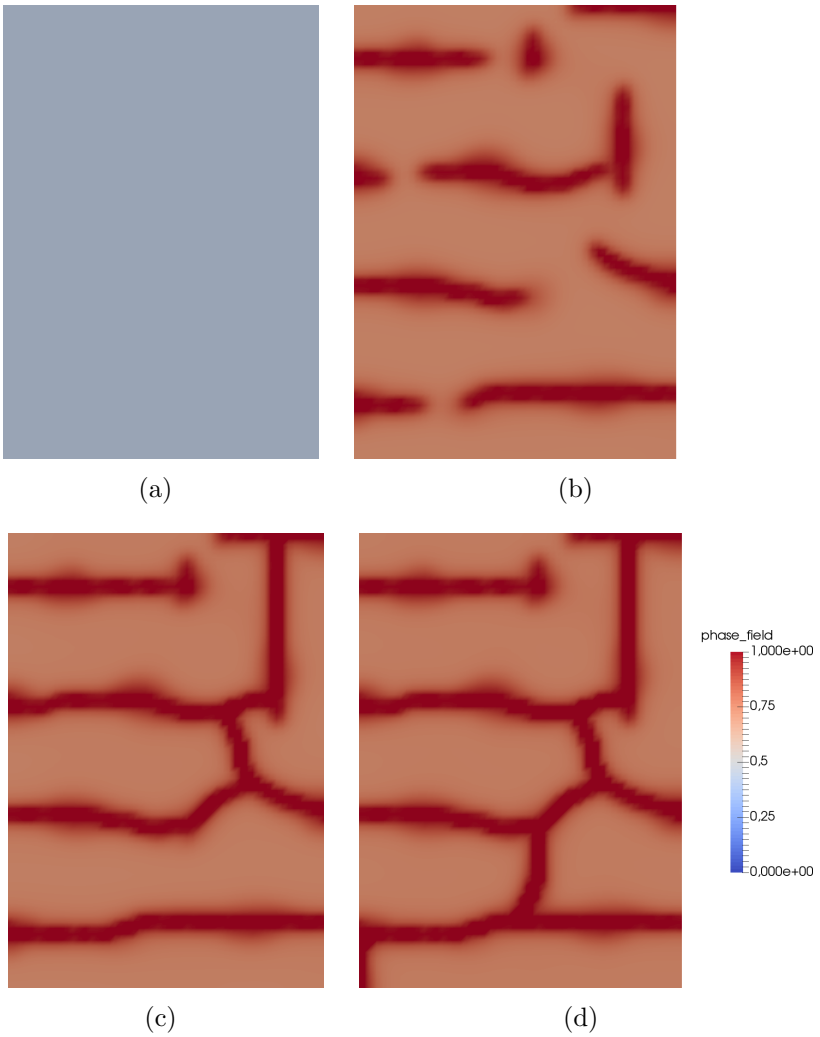


**Figure 5.25:** Top view of phase-field evolution in the three-dimensional specimen (restrained sides) with $\ell = 0.004$m, subjected to drying flux $\bar{q} = 6 \times 10^{-7}$ m/s at (a) $t = 15$ minutes, (b) 30 minutes, (c) 45 minutes, (d) 60 minutes. The first surface crack is observed at $t \approx 27$ minutes.

The three-dimensional cases demonstrate the ability of the model to simulate more

complex cracks induced by desiccation. The results show the influence of the mechanical restraint on the crack propagation. The *stronger* the restraint, the more cracks can be observed. This influence is also remarkable on the crack pattern, which becomes more complex in the restrained case in comparison with the free sides case. The same tendency is observed experimentally in [87, 88], where several and more complex mechanical restraints and surface roughnesses are tested.

### 5.3.3 Further numerical tests

As a result of the tested length scale, which determines the width of the regularization zone of the crack, the obtained *numerical* cracks are wide when compared to real, experimental cracks. The mesh size needs to satisfy $h \leq 0.5\ell$. A fine mesh is directly associated with an increase in the number of degrees of freedom. The increase is larger in the context of the mixed formulation when compared to a standard finite element formulation. A two-dimensional, quadrilateral element has 18, 4 and 9 degrees of freedom for $\mathbf{u}$, $p_w$ and $d$, respectively, while in three dimensions 81, 12 and 27 degrees of freedom are present for $\mathbf{u}$, $p_w$ and $d$, respectively. For this reason, further strategies to improve the efficiency of the current algorithm need to be developed. To check in practice the influence of the combination of shape functions with different orders and possibly reduce the number of degrees of freedom, the restrained case in three dimensions is reduced to a two-dimensional case. Aim is to investigate the influence of different shape function combinations for $\mathbf{u}$-$p_w$-$d$. The specimen is reduced to $210 \times 10\text{mm}^2$, representing the shortest edge of the three-dimensional sample. The bottom and sides are restrained, except for the symmetric ones, and the upper surface dries. To increase the resolution of the results, the next crack phase-field visualizations vary within the range $d \in [0.25 : 1]$.

The first case is tested with the Taylor-Hood pair and quadratic interpolation for the phase-field, i.e. quadratic for the displacement and phase-field variables and linear for the pore water pressure. This test is performed as a reference for the next scenarios. Three surface cracks initiate and propagate through the specimen as well as further at the bottom, Fig. 5.26.

Keeping the Taylor-Hood pair and assigning linear shape functions for the phase-field leads to mirrored results along the longitudinal axis in comparison to previous case, Fig. 5.27. These results are otherwise very similar to the previous case.

When all shape functions are linear, the cracks become wider and do not respect the chosen element scale, Fig. 5.28. This can be related to the wrong choice of the element pair for the displacement and pressure which violates the LBB condition.

For the sake of completeness, the case with quadratic shape function for the phase-field and linear shape functions for the displacement and pressure is computed, Fig. 5.29. The same tendency of wider crack propagation as in the previous test case is observed, as also in this case the LBB condition is not fulfilled.

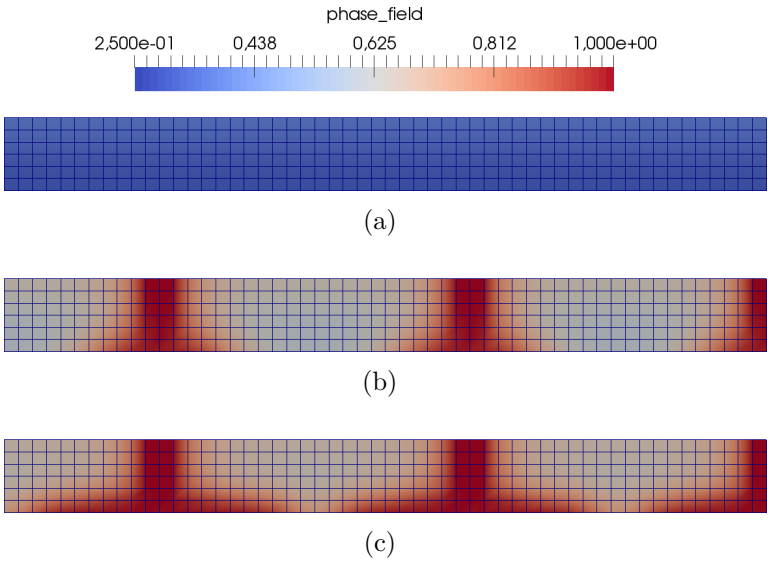


**Figure 5.26:** Phase-field evolution in the specimen with $\ell = 0.004$m, subjected to drying flux $\bar{q} = 6 \times 10^{-7}$ m/s with quadratic shape functions for the displacement and phase-field and linear shape functions for the pore water pressure at (a) $t = 15$ minutes, (b) 30 minutes and (c) 60 minutes. The first surface crack is observed at $t \approx 27$ minutes.

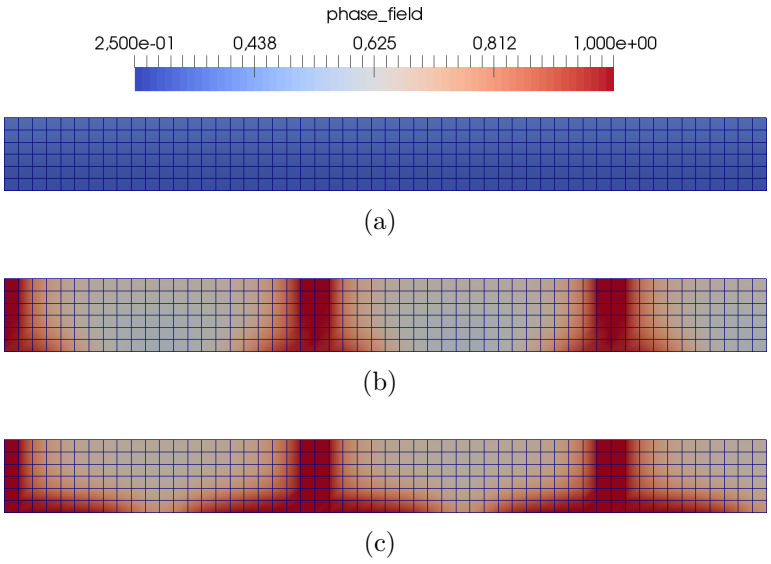


**Figure 5.27:** Phase-field evolution in the specimen with $\ell = 0.004$m, subjected to drying flux $\bar{q} = 6 \times 10^{-7}$ m/s with quadratic shape functions for the displacement and linear for the pore water pressure and phase-field variables at (a) $t = 15$ minutes, (b) 30 minutes and (c) 60 minutes. The first surface crack is observed at $t \approx 27$ minutes.

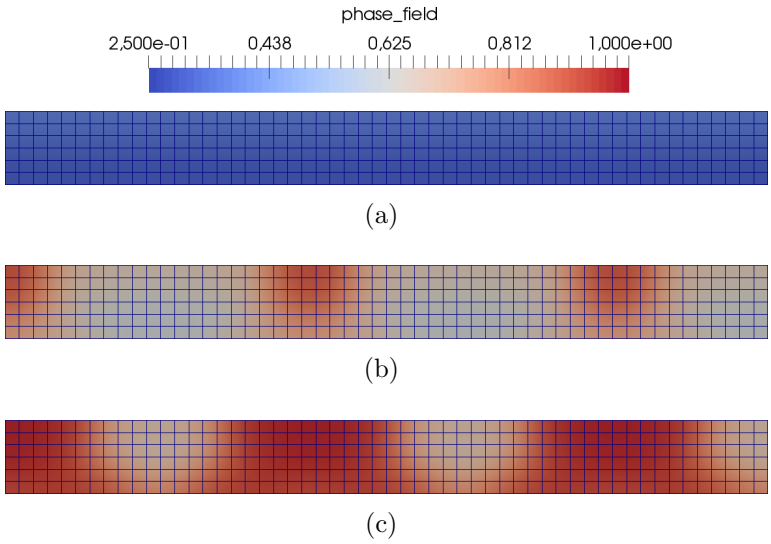


**Figure 5.28:** Phase-field evolution in the specimen with $\ell = 0.004$m, subjected to drying flux $\bar{q} = 6 \times 10^{-7}$ m/s with linear shape functions for the displacement, pore water pressure and phase-field variables at (a) $t = 15$ minutes, (b) 30 minutes and (c) 60 minutes. The first surface crack is observed at $t \approx 57$ minutes.

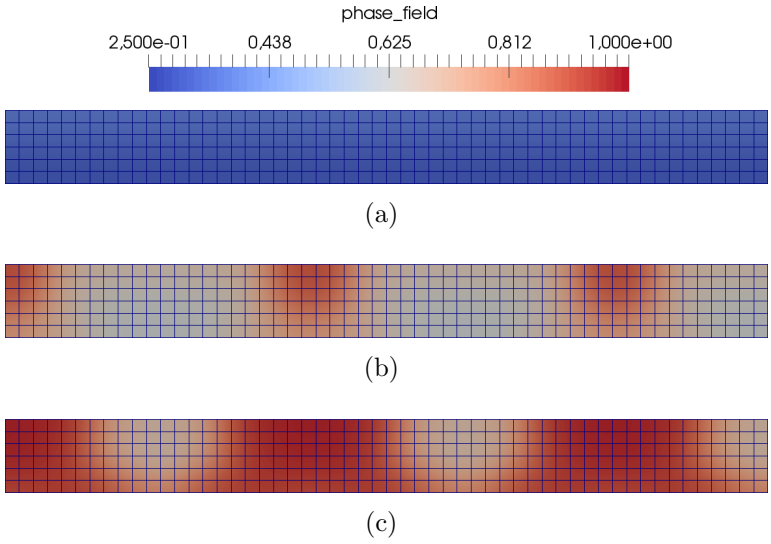


**Figure 5.29:** Phase-field evolution in the specimen with $\ell = 0.004$m, subjected to drying flux $\bar{q} = 6 \times 10^{-7}$ m/s with linear shape functions for the displacement and pore water pressure and quadratic for the phase-field at (a) $t = 15$ minutes, (b) 30 minutes and (c) 60 minutes. The first surface crack is observed at $t \approx 57$ minutes.

The test cases show the influence of the shape function combination for the involved variables and the generation of wider cracks. Due to the monolithic nature of the poromechanical problem, the LBB condition needs to be satisfied and consequently,

the number of degrees of freedom cannot be reduced. The tested cases indicate that the shape functions of the phase-field do not play an important role. The use of linear shape functions for all involved variables and avoiding the issue of wider cracks can be overcome with the stress-splitting solution scheme, see [163].

## 5.4 Summary

The model derived and discussed in Chapters 3 and 4 is applied to the study of consolidation, desaturation and desiccation. First, the poromechanical part of the model is validated in one dimension with the consolidation problem and the Liakopoulos desaturation benchmark. The numerical results are compared with either analytical solutions or benchmark numerical solutions from the literature. Later, the Liakopoulos column benchmark is modified in order to verify the ability of the model regarding crack evolution. For this, an external mechanical restraint is added to the problem resulting in cracking of the column.

After the one-dimensional verification, more complex problems are investigated. These are inspired by experimental constrained desiccation tests of clay-based materials from the literature. The setup represents a symmetric two-dimensional cross section of the specimen and takes into account the experimentally measured flux and saturation degree fitted with the van Genuchten curve. The elastic properties and fracture energy are let to vary with the water content according to experimental observations. A reference test shows that the framework is able to reproduce drying, deformation and cracking.

A sensitivity study related to the choice of the boundary conditions and material data is performed. Mechanical restraints affect the development of the crack on the corner of the sample. The higher the degree of restraint the more stress concentration on the corner and consequently the earlier the cracking. Furthermore, the step-wise application of the drying flux induces a later crack development on the corner of the sample. The increase of the drying flux induces more cracking. The same tendency is observed when decreasing the intrinsic permeability, since both strategies are related to larger pressure gradient development along the height of the specimen.

The relationship between the fracture energy and length scale parameter established in Chapter 3 is utilized in all setups. The dependency of the fracture energy on the length scale affects not only the crack development but also the width of the phase-field profile. With the increase of the length scale, the earlier and the more cracks are likely to occur due to the inverse proportionality between the length scale and the fracture energy. On the other hand, the increase of the length scale is directly associated with the crack width.

Preliminary numerical tests are conducted with adaptive mesh refinement. The error estimator is applied to the gradient of the pressure field due to its large variations during

drying. The computational cost reduces to half and the results obtained with the locally refined solution agree with the results provided by the fixed mesh. A specific error estimator for the phase-field solution and a corresponding procedure for the current framework need to be developed in order to obtain a more significant computational cost reduction.

The solution with 10 staggered iterations is compared with the explicit solution of the constrained desiccation problem. The compared results of the reference and higher flux test cases show good agreement. This fact can be related to the slow evolution of the desiccation-induced cracking problem.

In order to evaluate the influence of the crack field on the pressure field, the reference test case is analyzed. The uniform pore pressure field originated from the drying becomes non-uniform when the crack starts to evolve. The crack phase-field affects the pressure field up to the full development of the crack, although the coupling is indirect. Nevertheless, the coupling between these two fields should be further analyzed and improved as previously discussed in Chapter 3 and Appendix A.

Three-dimensional tests show the capability of the framework in simulating complex crack patterns and drying conditions. The mechanical restraint strongly affects the crack development and complexity of the crack pattern, i.e. the *stronger* the restraint, the more cracks occur.

Further work to improve the efficiency of the solution algorithm must be performed. This should concentrate on the development of efficient solution strategies with e.g. iterative solvers. The development of an hybrid algorithm combining both the advantages of shared and distributed memory in the parallelization strategies should be considered. Together, these should lead to an improvement of the speed of assembling and solving process. Moreover, a staggered strategy in the solution of the poromechnical problem can be applied. From the experimental viewpoint, experiments with a detailed range of material data and specific tests such as mass loss and cracking combined with aging should be carried out in order to enable quantitative comparison with simulation results.

# Part IV

# Application to cement-based materials and validation of the framework

# Chapter 6

# Experimental calibration and validation of poromechanical properties for cement mortar

In Chapter 5, material data from the literature were used as input to the numerical simulations of desiccation and the computational framework was applied to soils. The current chapter focuses on cement mortar and presents poromechanics-related experiments, including flexural tests, mass loss and free shrinkage tests. The mechanical and hygral material properties obtained through these tests are used as input to the drying and shrinkage simulations. These are performed for validation of the poromechanical part of the computational framework developed in Chapter 3.

## 6.1 Experiments

When utilizing input data from the literature, uncertainties related to the material composition and testing conditions such as boundary conditions, loading and environment are always present. For this reason, an experimental campaign was designed and carried out to provide accurate and consistent input parameters for the numerical framework presented in Chapter 3. The campaign took place at the Swiss Federal Laboratories for Materials Science and Technology (Empa) in Dübendorf, Switzerland.

In this chapter, the poromechanics-related experiments are described. The base material used to prepare the samples is a cement mortar with water-to-cement ratio (w/c) 0.5 and 40% aggregates by volume. The largest aggregates are of 3.2 mm size. Ordinary, rapid hardening portland cement CEM I 52.2N is used. The sand had average grain size of 312$\mu$m and maximum grain size of 650$\mu$m. The mortar mixture proportions are shown in Table 6.1.

**Table 6.1:** Mortar mixture proportions [kg/m$^3$]

| cement | water | sand |
|---|---|---|
| 599 | 306 | 1331 |

The experimental campaign is associated with the parameters of the poromechanical equations, namely the mechanical equilibrium equation, Eq. (3.2.6), i.e. Young's modulus and bulk modulus, porosity and density, and the mass balance of the pore water, Eq. (3.2.7), i.e. the van Genuchten parameters $\alpha_{vG}, n_{vG}$ and $m_{vG}$. We differentiate between direct and indirect calibration. During direct calibration, the measured quantities are either used directly as input parameters in the model or calculated analytically, e.g. the drying test is used to calibrate the flux of each specimen size since the outcome of this test is the mass loss. The indirect calibration uses the numerical model to calibrate the input parameter, e.g. the relative humidity test is simulated to calibrate the intrinsic permeability.

The size and number of prepared samples, the type of performed tests and their outcome in terms of measured quantities are all reported in Tables 6.2 and 6.3, for the direct and indirect calibration procedures, respectively.

**Table 6.2:** Experimental tests for direct calibration of the poromechanical properties

| **Test** | **Measured quantity** | **Sample size [mm$^3$]** | **Calibrated input parameters** | **Number of samples** |
|---|---|---|---|---|
| Three-point bending | Young's modulus | $40 \times 40 \times 160$ | Biot parameter | 3 |
| Water accessible porosity | Porosity<br>Density | $40 \times 40 \times 160$ | Porosity<br>Density | 2 |
| Gravimetric sorption | Sorption isotherm | $10 \times 10 \times 0.5$ | van Genuchten parameters | 2 |
| Drying | Mass loss | $40 \times 40 \times 160$<br>$120 \times 120 \times 360$ | Flux | 3<br>2 |

**Table 6.3:** Experimental tests for indirect calibration of the poromechanical properties

| **Test** | **Measured quantity** | **Sample size [mm$^3$]** | **Calibrated input parameters** | **Number of samples** |
|---|---|---|---|---|
| Relative humidity | Relative humidity | $100 \times 100 \times 360$ | Intrinsic permeability | 2 |

Finally, the poromechanical framework is validated with the free shrinkage test, which uses all directly and indirectly calibrated parameters. The experimental tests and respective results are described in detail in the following subsections.

### 6.1.1 Three-point bending tests

The static Young's modulus is obtained through three-point bending tests according to the norm DIN EN 12390-13:2013 [50]. Three samples with $H \times B \times L = 40 \times 40 \times 160\text{mm}^3$ are cast, hermetically sealed and placed in a room with controlled temperature of 20°C and relative humidity of 70%. All samples are sealed up to 28 days. At the age of 28 days, the samples are removed from the room and flexural tests are performed resulting in the Young's modulus $E_{28d} = 25.6 \pm 0.1$ GPa.

The bulk modulus of the porous medium $K_{28d}$ is computed with estimated Poisson's ratio $\nu = 0.2$

$$K_{28d} = \frac{E_{28d}}{3(1-2\nu)} \Rightarrow K_{28d} = 14.22 \pm 0.06\text{GPa} \tag{6.1.1}$$

and applied to determine the Biot parameter $\alpha$ with estimated bulk modulus of the solid grains $K_s = 45$GPa [96],

$$\alpha = 1 - \frac{K_{28d}}{K_s} \Rightarrow \alpha = 0.684 \pm 0.001. \tag{6.1.2}$$

### 6.1.2 Water accessible porosity tests

The water accessible porosity and the density of the material are determined with the water accessible porosity tests. Two prismatic samples with $40 \times 40 \times 160\text{mm}^3$ are tested. First, the initial weights of the samples in air and water (apparent weight), $m_0$ and $m_{0_w}$, respectively, are determined. These samples are placed in an oven with constant temperature of 50°C for one week. Then, their weights in air are measured. In order to re-use the samples and continue the test at a second dry state, these are placed in another oven with constant temperature of 105°C for one week. After that the weights in air are determined. Table 6.4 shows the obtained values at the different measurement phases.

**Table 6.4:** Weight measurements [kg], obtained porosity [-] and density [kg/m$^3$]

| $m_{0_w}$ | $m_0$ | $m_{(T=50)}$ | $m_{(T=105)}$ | $n_{(T=50)}$ | $\rho_{d(T=50)}$ | $n_{(T=105)}$ | $\rho_{d(T=105)}$ |
|---|---|---|---|---|---|---|---|
| 0.29642 | 0.5521 | 0.51933 | 0.50067 | 0.139 | 2007 | 0.211 | 1935 |

During weight measurement in water, the mass of water displaced by the sample $m_{dw}$ is given by

$$m_{dw} = m_0 - m_{0_w} \tag{6.1.3}$$

and the corresponding displaced volume $V_{dw} = \dfrac{m_{dw}}{\rho_w}$ coincides with the bulk volume of the sample $V$ as stated by the Archimede's principle (hydrostatic weighing). The relationship between the volume of the pores $V_v$, i.e. the (accessible) volume of water

lost between the initial and reference dry state measurements, and the bulk volume of the sample represents the water accessible porosity, determined by

$$n = \frac{V_v}{V} = \frac{\frac{m_0 - m}{\rho_w}}{V_{dw}}. \tag{6.1.4}$$

The dry density is computed with

$$\begin{aligned} \rho_d &= \frac{m}{V} = \frac{m}{V_{dw}} \\ \rho_s &= \frac{\rho_d}{1-n} \end{aligned} \tag{6.1.5}$$

where $m$ is the current weight in air after one week in the oven at the specified temperature. The $\rho_s$ represents the density of the solid grain/phase and is shown for completeness.

### 6.1.3 Gravimetric sorption tests

Gravimetric sorption measurements are performed with a dynamic vapor sorption (DVS) analyzer. Here, the mass changes of platelets with $10 \times 10 \times 0.533\text{mm}^3$ are measured with a high-precision balance with $10\mu$g accuracy. The mass variations are caused by RH changes. At the end of the test, a higher temperature is imposed to determine the reference state. The obtained results represent the sorption isotherm of the material, i.e. the curve which relates the changes in water content or water degree of saturation and the relative humidity.

The sorption isotherms for the material in study are determined at $T = 20°\text{C}$ for two reference dry states, $T = 50°\text{C}$ and $T = 105°\text{C}$. The results given by the relationship between the moisture content (quotient between the current mass of water in the sample and the reference dry mass of the sample) and the RH are shown in Fig. 6.1. The dry mass of the sample is 106.51g at $T = 50°\text{C}$ and 103.18g at $T = 105°\text{C}$.

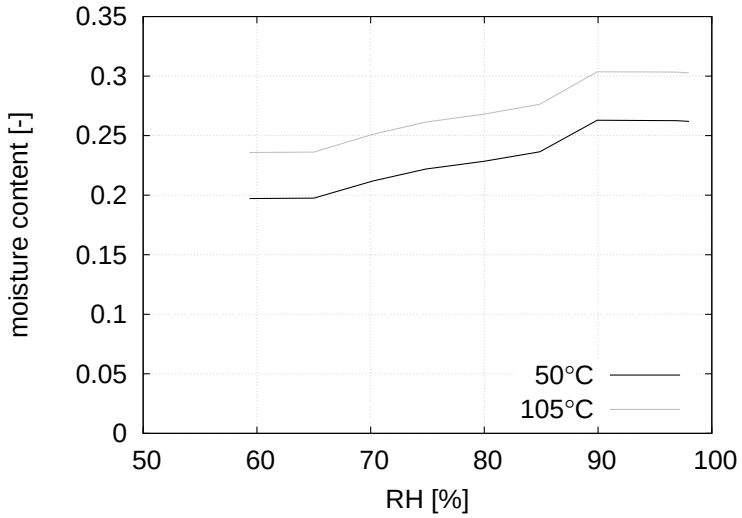


**Figure 6.1:** Water content sorption isotherms of mortar specimen with w/c=0.5 and 40% aggregate volume for reference dry states $T = 50, 105°\mathrm{C}$.

The saturation degree is then computed as the quotient between the current and the initial water contents, resulting in Fig. 6.2.

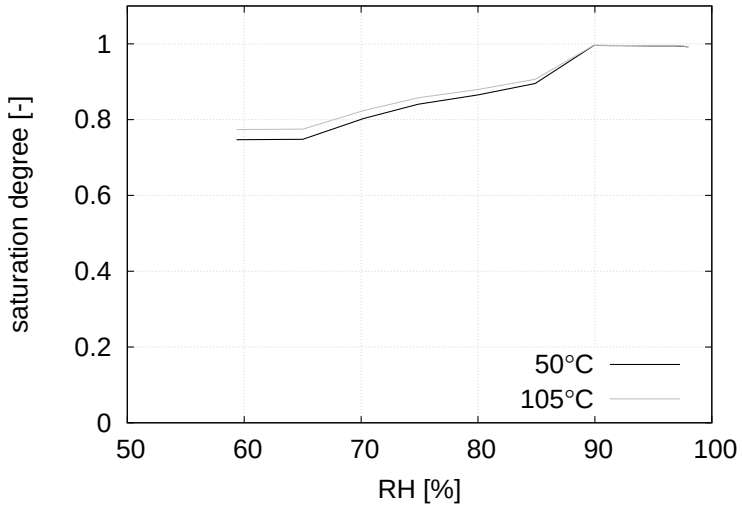


**Figure 6.2:** Degree of saturation curves of mortar specimen with w/c=0.5 and 40% aggregate volume for two reference dry states $T = 50, 105°\mathrm{C}$.

Note that the water degree of saturation curves at the two reference dry states are very similar. The isotherm for $T = 50°\mathrm{C}$ is chosen and referred to further in this work. For exemplification, the shrinkage responses utilizing the porosity and solid dry density at the two reference dry states are modeled in Subsection 6.2.2.

The degree of saturation curve can be re-computed in order to obtain a direct rela-

tionship between the water degree of saturation $S_w$ and the pore pressure $p_w = -p_c$ to satisfy Eq. (3.2.7). A widely used saturation-pressure law is known as van Genuchten law [152] and is commonly used in the literature to model the development of $S_w$ due to suction changes. The water pore pressure is computed via the Kelvin-Laplace relationship as follows

$$p_w = \frac{\rho_w R T}{M} \ln(RH), \tag{6.1.6}$$

where $R = 8.314\text{J/(mol K)}$ is the universal gas constant, $T = 293.15\text{K}$ is the ambient temperature, $M = 0.01802\text{kg/mol}$ is the molar mass of the pore fluid (water) and RH is the relative humidity. Equation (6.1.6) is valid for RH $\in ]0:1]$ and negative pore water pressure values, namely in the capillary regime. When the water pore pressure is positive, the RH is constant and equal to 1 (or 100%).

The saturation degree $S_w$, the effective saturation $S_e$ and the relative permeability $k_{rw}$ are calibrated by a fitting through Eqs. 3.3.1-3.3.3. The van Genuchten parameters obtained after the fitting are $\alpha_{vG} = 3.5863 \times 10^{-4}\text{m}^{-1}$, $n_{vG} = 2.6293$ and $m_{vG} = 1 - 1/n_{vG}$. Moreover, $S_r = 0.67881$ and the correspondence index is $R^2 = 0.91938$, Fig. 6.3. The parameters are obtained using the SWRC fitting tool available in [137]. For this, the pressure must be given in terms of suction head in [m], i.e. suction $= \dfrac{-p_c}{g\,\rho_w}$

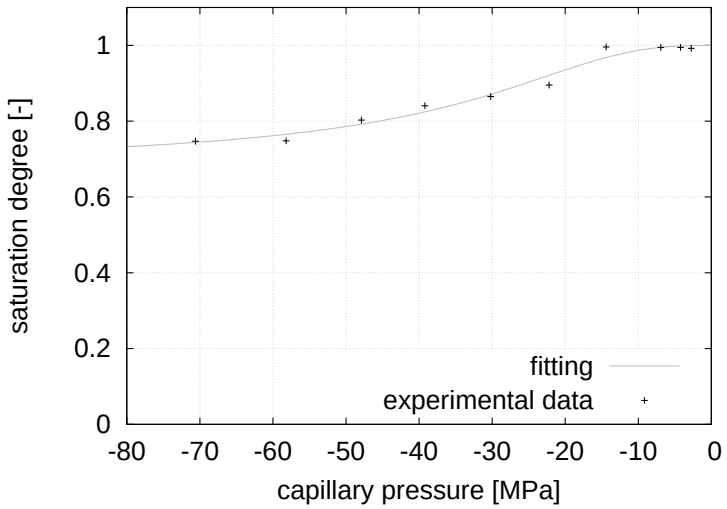


**Figure 6.3:** Van Genuchten fitting of experimental data points obtained from sorption isotherm.

### 6.1.4 Drying tests

The mass loss experiment consists in determining the mass changes of samples at different times/ages. In this work, mass loss experiments of medium ($40\times40\times160\text{mm}^3$) and large ($120 \times 120 \times 360\text{mm}^3$) samples are carried out. The samples are placed in

a room with controlled temperature $T = 20^oC$ and RH= 70%. After maturing time of 28 days (initial age, $t_0 = 0$) in sealed conditions, the mass loss of each sample is determined at $1, 3, 7, 14, 28$ days. The average mass loss and corresponding deviations for each specimen type are shown separately in the following subsections.

The mass loss results are used to compute the flux $q$ for each time increment as

$$q = \frac{\Delta m}{A\rho_w}\frac{1}{\Delta t} = \frac{m - m_0}{(4A_1 + 2A_2)\rho_w}\frac{1}{\Delta t} \tag{6.1.7}$$

where $\Delta t = t - t_0$, with $t$ as the actual time of measurement. The total specimen area is represented by $A$. Since all sides are free to dry, the total area is calculated by the sum of the rectangular $A_1$ and square $A_2$ surface areas.

For completeness, the standard deviation of the flux is computed. The latter decreases with time since $\Delta t$ increases, e.g. the average deviation after $\Delta t = 1$ day of drying is larger than the average deviation after $\Delta t = 28$ days of drying. The pointwise computed fluxes are fitted with the Matlab Curve Fitting Toolbox® to obtain a continuous curve to be implemented in the simulations. The double exponential function given by

$$q = a\exp(bt) + c\exp(dt) \tag{6.1.8}$$

is used to fit the computed flux. The results are shown in the following.

### Medium sample

The mass loss results and their corresponding deviations are shown in Fig. 6.4(a). The values of the computed pointwise flux and fitted curve are plotted in Fig. 6.4(b) A linear extrapolation from the data of 1 and 3 days is performed to obtain the flux at the first point (day 0).

### Large sample

Figure 6.5(a) shows the mass loss of the large sample and Fig. 6.5(b) shows the correspondent computed fluxes. The slope of the flux obtained between day 1 and 3 is negative and not compatible with the further course of the curve. Furthermore, the data at day 1 has a large deviation. For this reason, the data from day 1 are discarded and the flux at day 0 is determined using the exponential curve directly.

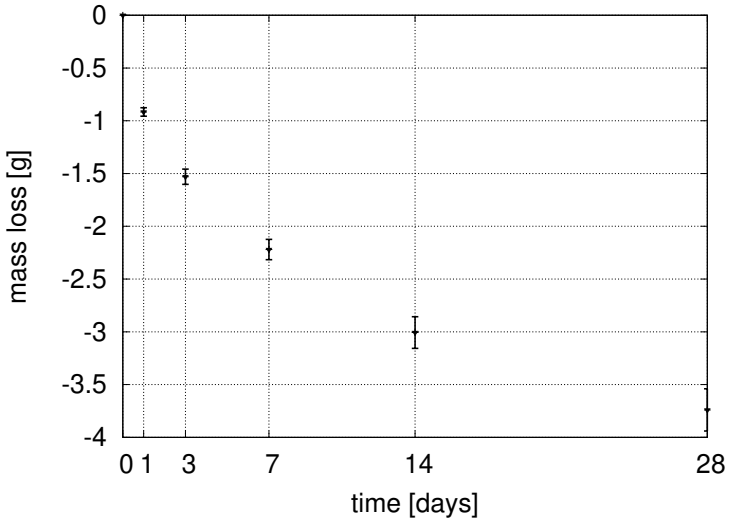


(a)

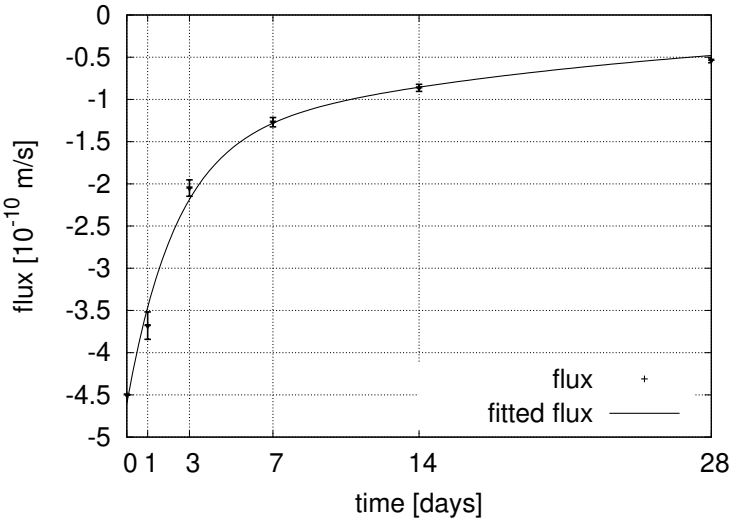


(b)

**Figure 6.4:** Mass loss of medium specimen measured at $1, 3, 7, 14, 28$ days after start of the test with samples 28 days old. The flux is computed through the mass difference and fitted with a double exponential curve with $a = -3.105 \times 10^{-10}$, $b = -4.965 \times 10^{-6}$, $c = -1.499 \times 10^{-10}$, $d = -4.711 \times 10^{-7}$ and deviation $R^2 = 0.9938$.

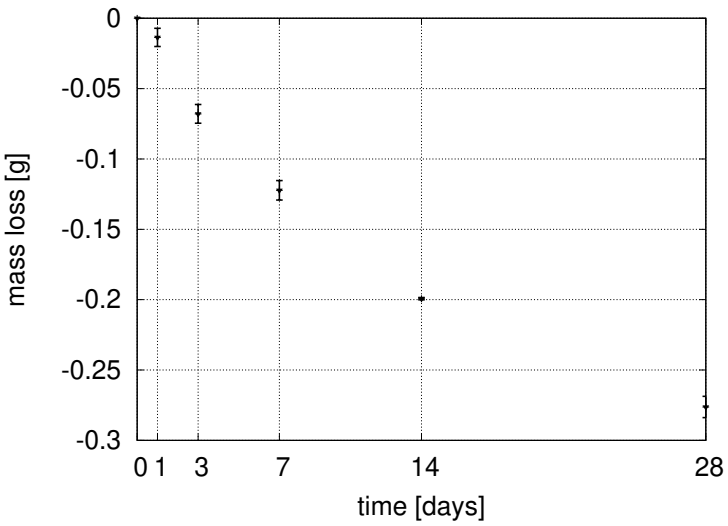


(a)

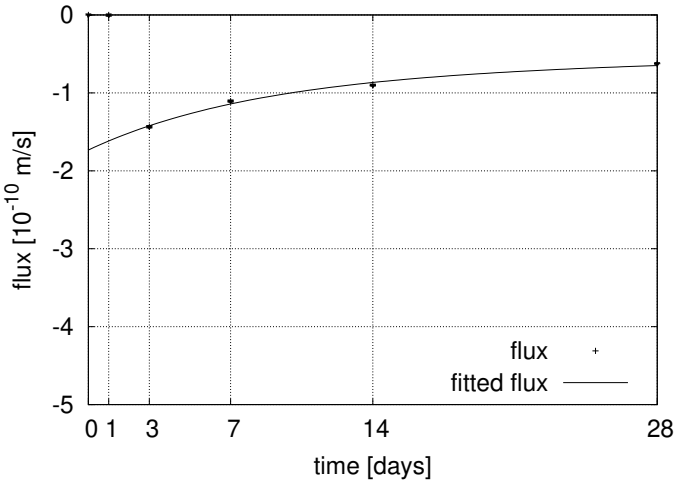


(b)

**Figure 6.5:** Mass loss of large specimen measured at $1, 3, 7, 14, 28$ days after start of the test with samples 28 days old. The flux is computed through the mass difference and fitted with a double exponential curve with $a = -9.666 \times 10^{-11}$, $b = -1.391 \times 10^{-6}$, $c = -7.666 \times 10^{-11}$, $d = -9.055 \times 10^{-8}$ and deviation $R^2 = 0.995$.

Note that the average mass loss increases with the increase of the sample size and that the computed flux decreases in absolute value.

### 6.1.5 Relative humidity tests

In order to understand the evolution of the RH in the sample, a one directional free drying test is carried out with the large samples. The large samples are completely

sealed and are placed in a room with controlled constant temperature, $T = 20°C$ and relative humidity $RH = 70\%$. At the age of 28 days, all faces remain sealed except for the two longitudinal sides, from where the samples are allowed to dry, as shown in Fig. 6.6.

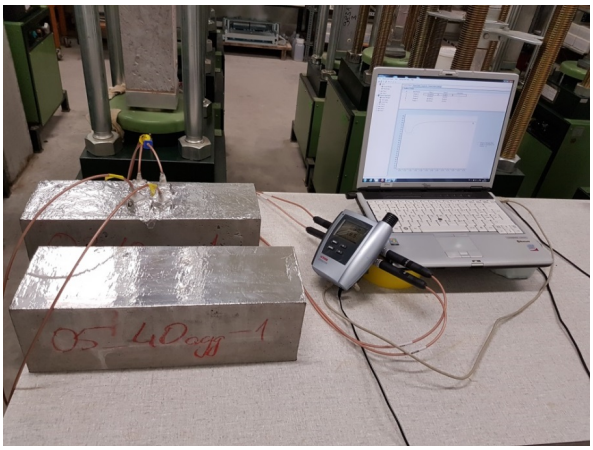

**Figure 6.6:** Experimental setup of RH test. The sample is sealed everywhere except for two longitudinal surfaces.

In order to measure the RH evolution with time, sensors are placed at different distances $(1, 2, 3, 4, 5, 6$ cm) from the unsealed (drying) surface of the specimen. With this type of arrangement, the gradients present in the medium due to the drying front and the average of the measurements can be determined. The obtained values at different ages are calibrated and shown in Fig. 6.7.

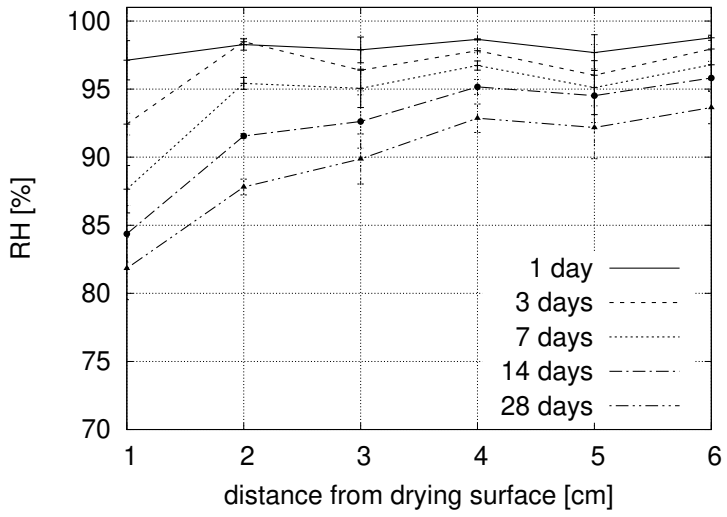


**Figure 6.7:** RH evolution along distance from the drying surface at 1, 3, 7, 14 and 28 days after starting of drying from the longitudinal sides. The initial condition of the test (day 0) corresponds to a completely sealed state.

Note that the samples remain at rather high RH$\geq$ 90% during the measurements performed at days 1 and 3. The region near the core at distances 3 to 6 cm remain at RH$\geq$ 90% up to 28 days. The first layer shows the larger rate of decrease in RH, as expected, due to the proximity to the drying front.

### 6.1.6 Shrinkage tests

The shrinkage experiment consists in determining the change of volume of a determined specimen. In the current experimental setup, the specimen is placed on a simple support such that it is free to dry and shrink, Fig. 6.8.

**Figure 6.8:** Medium samples utilized in the mass loss and shrinkage experiments.

The shrinkage of the medium and large samples is determined experimentally in the same samples utilized in the mass loss experiments. Three repetitions are executed for the medium samples, while two repetitions are carried out for the large ones.

In this work, the shrinkage obtained experimentally is related to the unidimensional length change of the longer axis, i.e. the axial dimension of the specimen. For the medium and large samples, the initial length is 160 and 250 mm, respectively. The measurements are performed according to the Swiss Standard SIA 262/1 (2013) Annex F [1].

In order to avoid repetitions, the experimental results are presented and compared directly with the numerical ones. These are shown together in Section 6.2.2.

## 6.2 Simulations

Aim here is to use the experimental results to calibrate the intrinsic permeability of the material as well as to validate the poromechanical model by simulating (i) RH tests for the large sample and (ii) free shrinkage tests for all sample sizes.

### 6.2.1 Simulation of the relative humidity tests

This setup is used to calibrate the intrinsic permeability of the medium. Moisture gradients develop due to the different environmental and internal RH. The numerical RH evolution is compared to the experimental RH measurements.

The numerical setup reproduces the RH experimental setup of the large specimen, discussed in Section 6.1.5. The symmetry of the problem is considered, moreover the full three-dimensional model is reduced to a two-dimensional cross-section in the drying direction as shown in Fig. 6.9.

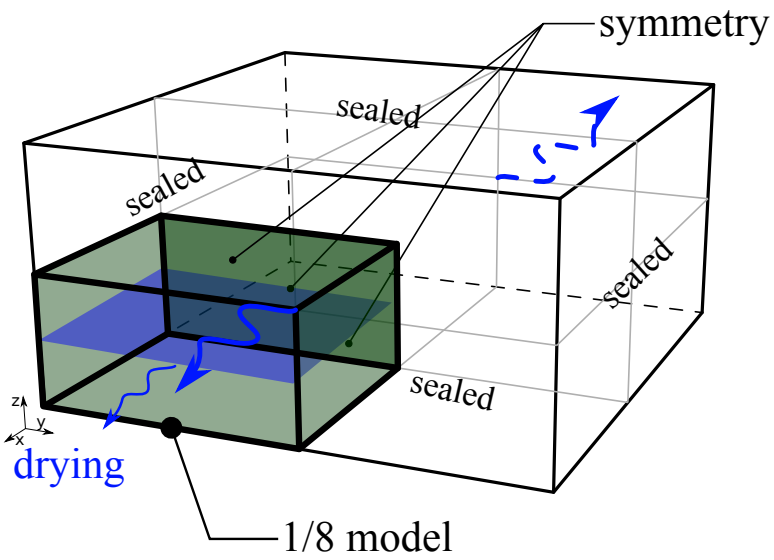


**Figure 6.9:** Modeling setup of RH test. The thicker blue arrows represent the drying. The symmetry is taken into account in all three planes and the model is reduced to two dimensions (cross-section in light blue). The sample is sealed everywhere except for the two specified drying surfaces.

A Dirichlet boundary condition representing the ambient RH= 70% is imposed on the drying face of the sample. Zero-flux boundary conditions are imposed everywhere else. Furthermore, symmetry boundary conditions are imposed as shown in Fig. 6.9.

The sorption isotherm, i.e. degree of saturation curve, obtained experimentally is utilized. The further experimentally determined hygral parameters as presented in Section 6.1 are also taken into account. The only unknown parameter is the intrinsic permeability $k_i$, which we aim at calibrating by comparing the numerical moisture profile and the experimental profile discussed in Section 6.1.5, Fig. 6.7.

First, a large set of intrinsic permeability values, $k_i = \{10^{-19}, 10^{-20}, 10^{-21}, 10^{-22}, 10^{-23}\}$ m$^2$, is considered up to 1 day of test to determine the acceptable range of permeability values. The results of the preliminary analysis are shown in Fig. 6.10.

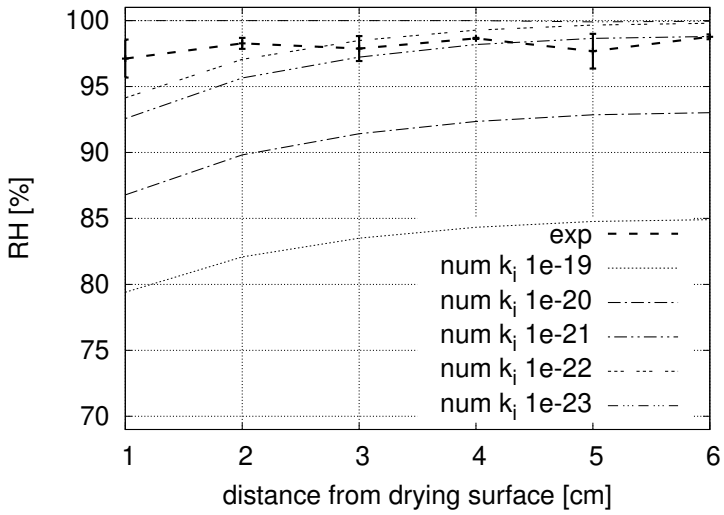


**Figure 6.10:** Experimental and numerical results of relative humidity (drying) simulation up to 1 day of test. The experimental range at 1 day is shown.

The best agreement between experiments and simulation is found within the range of intrinsic permeabilities $10^{-21}$ m$^2$ to $10^{-22}$ m$^2$. The convergence of the results with respect to the time step and mesh size are also tested. The time step $\Delta t = 8640$s (1/10 day) and a fixed mesh with 12288 elements ($128 \times 96$ elements in each direction) are adopted. In this type of simulation, a fine mesh is required to ensure that the gradients can be reproduced. The results of the coupled poromechanical simulation ($\alpha \neq 0$, determined in Section 6.1.1) are shown in Fig. 6.11 up to 28 days.

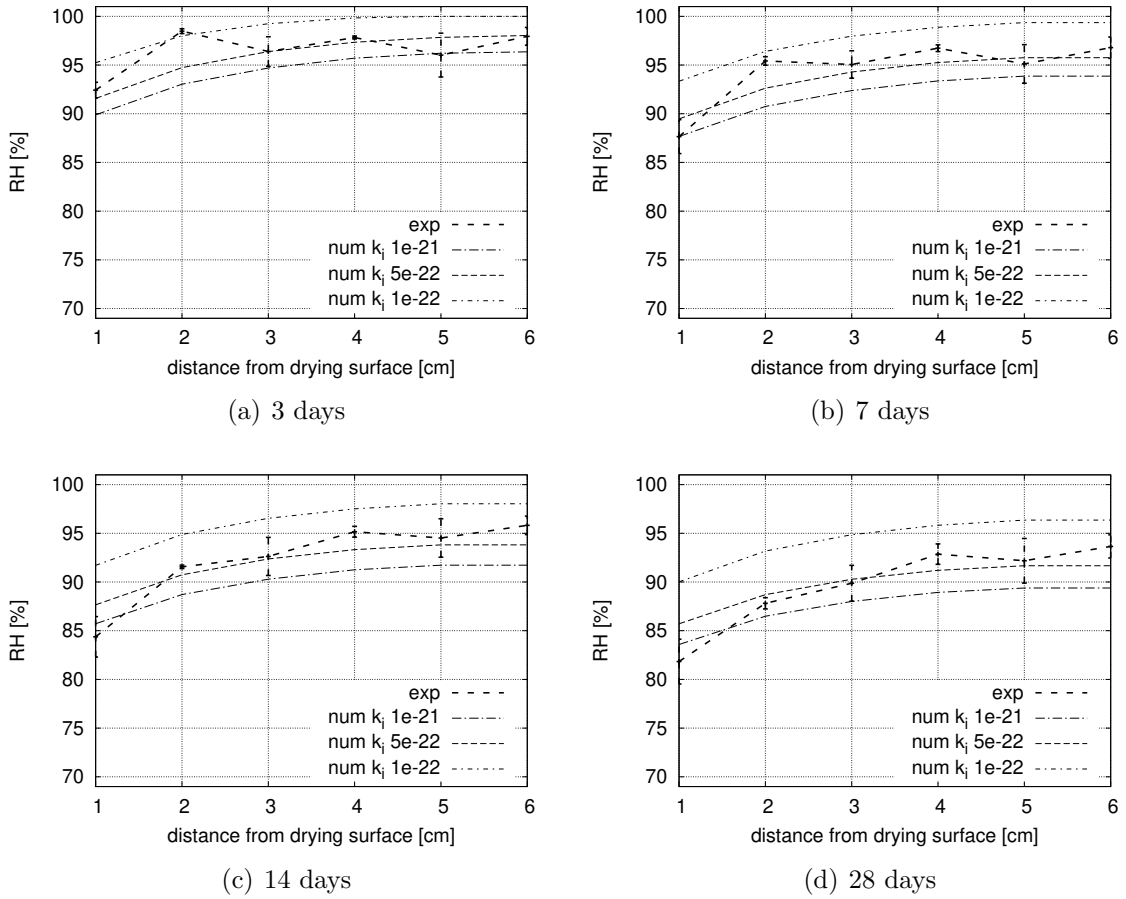


(a) 3 days (b) 7 days

(c) 14 days (d) 28 days

**Figure 6.11:** Experimental and numerical results of relative humidity (drying) test from 3 to 28 days using the coupled poromechanical model. The experimental results are shown in the same range.

As it can be observed, the intrinsic permeabilities $k_i = 1 \times 10^{-21}$ and $k_i = 5 \times 10^{-22}$ m$^2$ show good agreement with the experimental values.

For completeness and comparison, the uncoupled simulation ($\alpha = 0$) is carried out. The results are shown in Fig. 6.12. The curves are flatter in comparison to the coupled case.

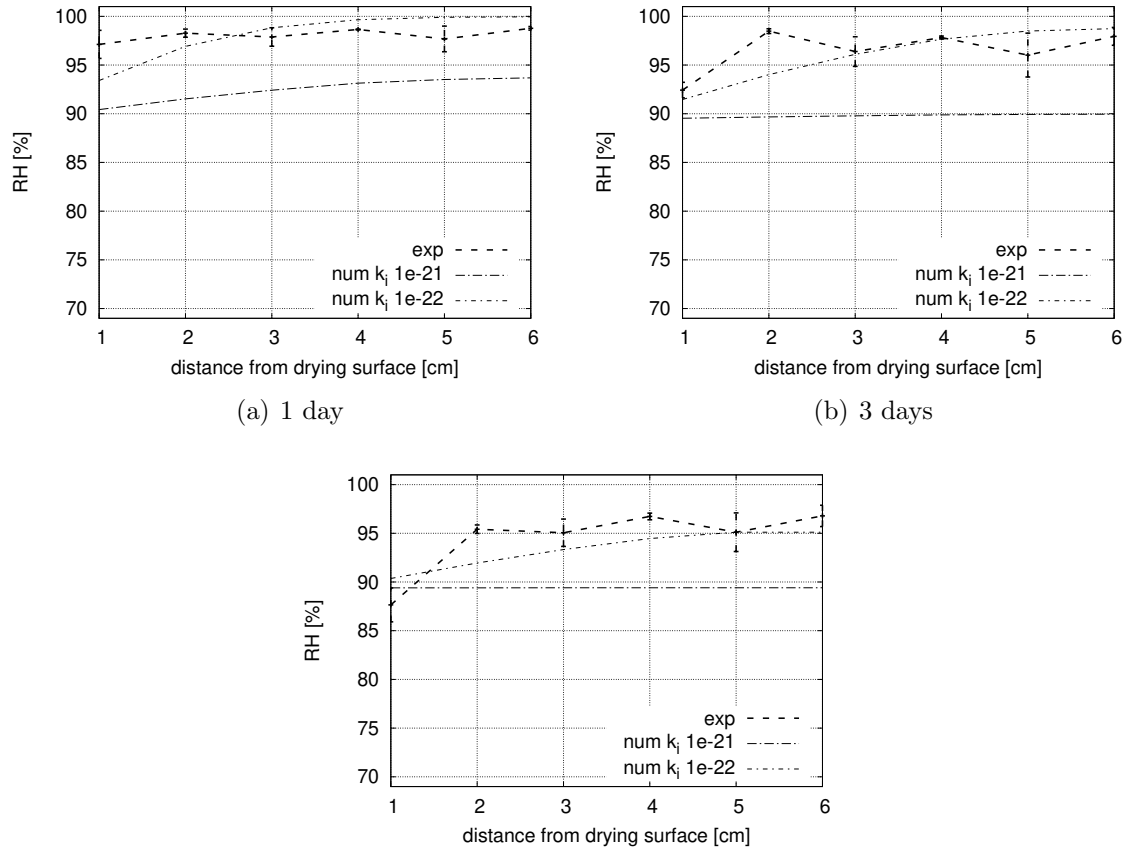


(a) 1 day

(b) 3 days

(c) 7 days

**Figure 6.12:** Experimental and numerical results of relative humidity (drying) test from 1 to 7 days using the uncoupled poromechanical model. The experimental results are shown in the same range.

As it can be observed from the results, the coupled simulation shows better agreement with the experimental results. In general, the uncoupled model predicts lower RH at the same tested permeability, when compared to the coupled one. This is due to the fact that important terms such as the contribution of the change of strain in Eq. (3.2.7) are neglected. This denotes that the simplification of the model, i.e. the uncoupled model, can lead to wrong calibration of the permeability.

The coupled poromechanical model with the narrow range of intrinsic permeability values $k_i = \{1, 5, 10\} \times 10^{-22}$ m$^2$ is adopted in the following section for validation with the results of the shrinkage test.

### 6.2.2 Simulation of the shrinkage tests

Aim here is the validation of the poromechanical part of the framework. The prismatic samples of Section 6.1.6 and their experimental setup are reproduced computationally. Since the flux is present on all faces of the samples and these are free to shrink, symmetry boundary conditions are used. The three-dimensional model consists of one-eight of the sample with imposed drying flux at all the outer surfaces except for the symmetric ones, Fig. 6.13.

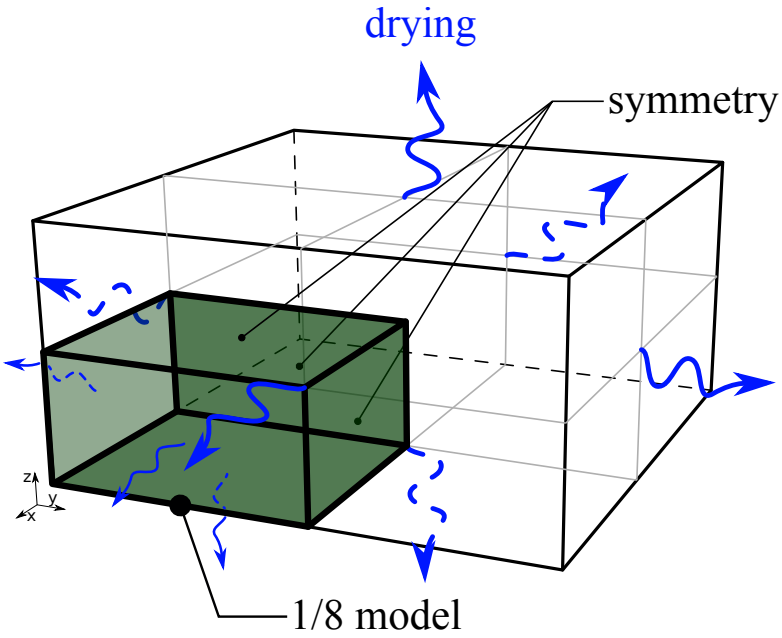


**Figure 6.13:** Modeling setup of the free shrinkage test. The thicker blue arrows represent the drying. The symmetry is taken into account in all three planes. The sample is unsealed everywhere and flux is imposed at the outer surfaces.

The experimental data calibrated in Section 6.1, including Young's modulus, Biot parameters and van Genuchten parameters, are adopted. The flux computed through the experimental mass loss is utilized. Furthermore, the intrinsic permeability calibrated in Section 6.2.1 is used. The simulation runs up to $t = 28$ days with $\Delta t = 8640$ s (1/10 day). The mesh consists of $8 \times 8 \times 32$ elements.

Results for each specimen type are shown separately and compared with the experimental results in the next subsections. The length change is measured at the main axis of the sample.

#### Medium sample

The flux curve shown in Fig. 6.4(b) is applied as drying flux. Figure 6.14 shows the results obtained experimentally and numerically.

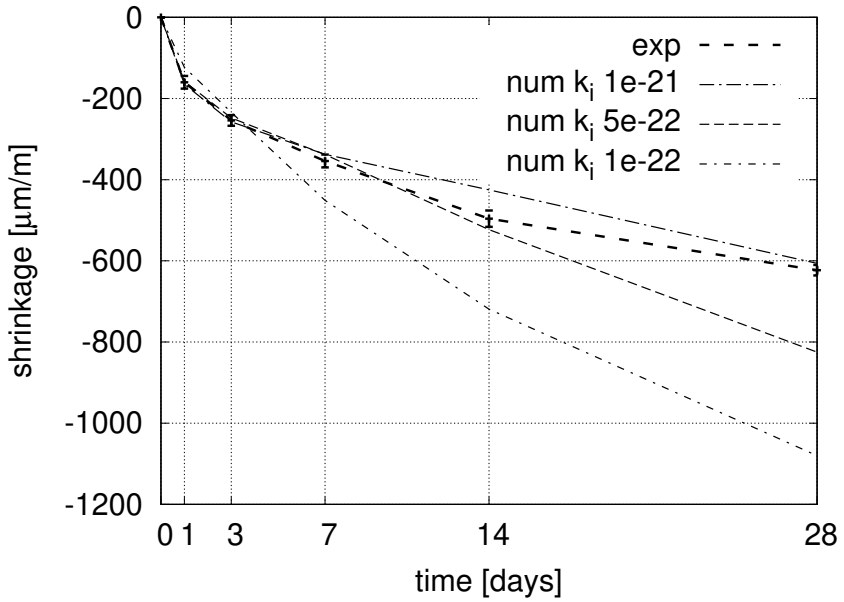


**Figure 6.14:** Experimental and numerical shrinkage results of the medium specimen.

Both simulation results using $k_i = \{5, 10\} \times 10^{-22}\mathrm{m}^2$ show good agreement up to 14 days, while $k_i = 1 \times 10^{-22}\mathrm{m}^2$ overestimates the expected shrinkage. The best agreement is found with $k_i = 1 \times 10^{-21}\mathrm{m}^2$ up to 28 days.

For completeness, the results using the experimentally obtained porosity and density at the reference state $T = 105°\mathrm{C}$ are depicted in Fig. 6.15.

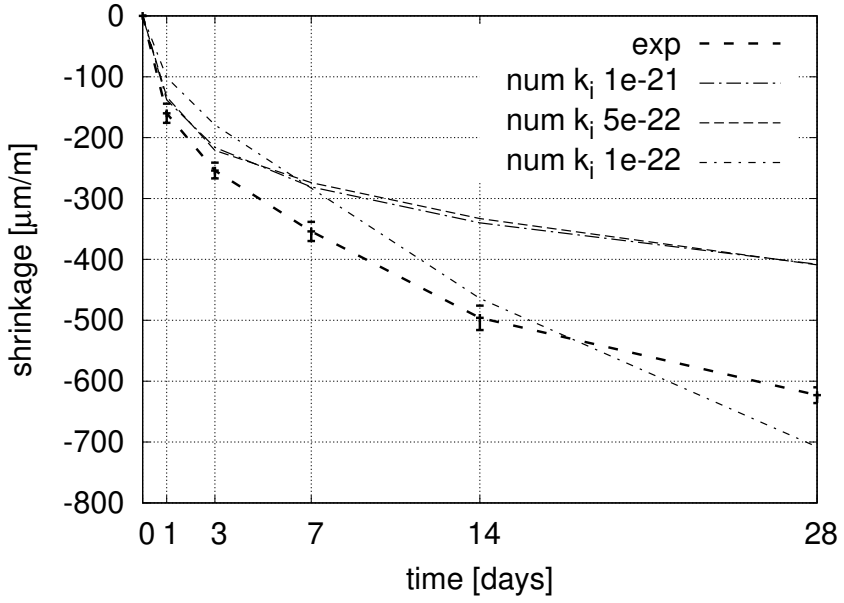


**Figure 6.15:** Experimental and numerical shrinkage results of the medium specimen using the experimental input parameters obtained at higher reference temperature.

As expected, these samples shrink less in comparison to the reference case at $T = 50°C$ at the same range of tested permeabilities. At the drier reference state, the porosity is lower and this fact contributes to the decrease of the deformation of the sample. This behavior is also related to the strong dependency of the approach on $S_w$ as referred in [160].

### Large sample

The experimental measurements are taken along 250 mm of the sample (total sample length is 360 mm). The flux curve shown in Fig. 6.5 is applied as drying flux. Figure 6.16 shows the results obtained experimentally and numerically.

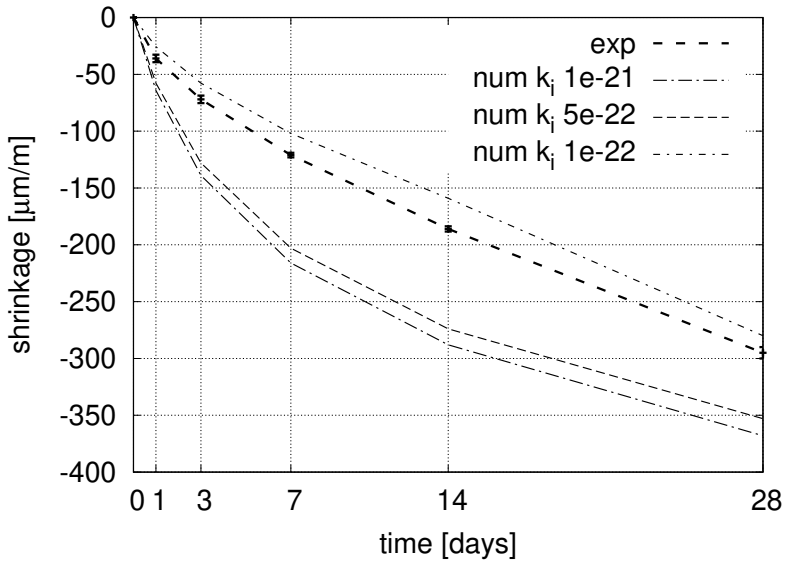


**Figure 6.16:** Experimental and numerical shrinkage results of the large specimen.

The numerical shrinkage results with $k_i = \{5, 10\} \times 10^{-22}\text{m}^2$ overestimate the experimental results. At 28 days, the overestimation is approximately 15%. On the other hand, the results with $k_i = 1 \times 10^{-22}\text{m}^2$ slightly underestimate the expected shrinkage.

The differences in the shrinkage results could be related to the fact that the simulations do not account for viscoelastic effects. These effects are stronger for less permeable materials as well as during slower transport. The influence of relaxation is more important for larger samples when compared to smaller ones, since in larger samples the transport is slower.

### *Remarks*

- The best agreement between experiments and simulation is found with intrinsic permeability $k_i = 1 \times 10^{-21}\mathrm{m}^2$ in the medium and large samples. For this reason, the intrinsic permeability $k_i = 1 \times 10^{-21}\mathrm{m}^2$ is further used in this work.

## 6.2.3 Predictions of long-term shrinkage

Short-term shrinkage is observed at early ages, when water is available in more quantity in the sample. This type of shrinkage is characterized by a large slope in the shrinkage response. With age and less available water, the shrinkage of the sample tends to stabilize, i.e. the slope of the curve reduces and becomes approximately constant. This behavior is called long-term shrinkage.

To predict long term shrinkage, the final time of the simulation is set to 1 year. The same input data is utilized, i.e. input data up to 28 days related to short-term shrinkage. Furthermore, the medium sample is chosen since it is independent of the large samples with respect to the geometry and flux, e.g. used during the RH tests. The results are shown in Fig. 6.17. The long term simulation predicts the experimental results very well.

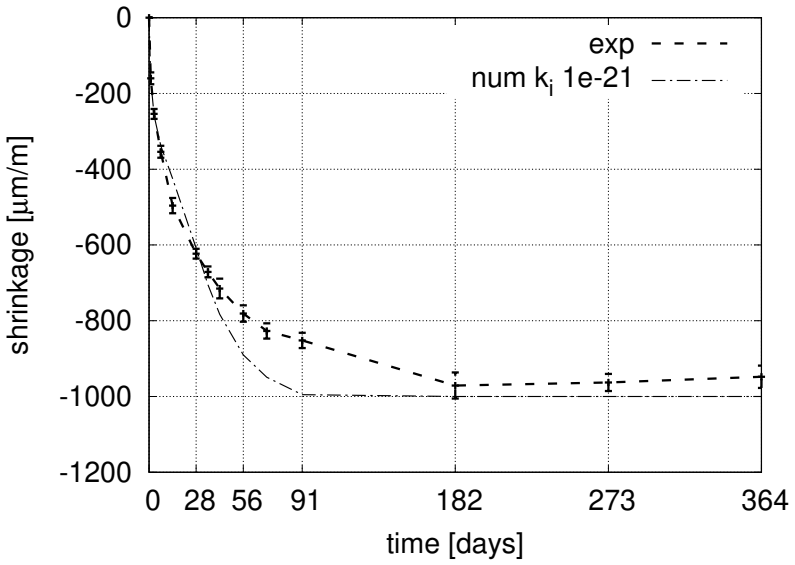


**Figure 6.17:** Experimental and numerical shrinkage results of the medium specimen over 1 year.

To ensure that the predictions of long term shrinkage are also valid for the large samples, these are computed up to 1 year. The results are shown in Fig. 6.18. The numerical predictions agree very well with the experimental results.

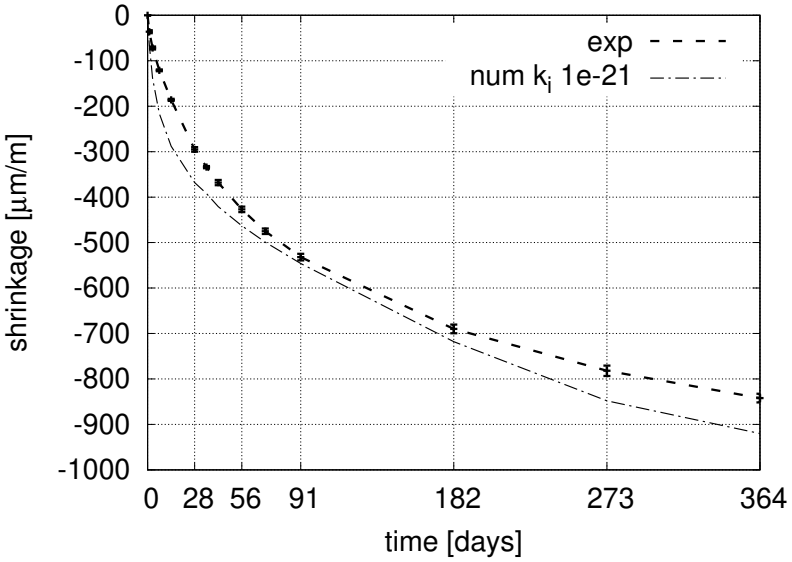


**Figure 6.18:** Experimental and numerical shrinkage results of the large specimen over 1 year.

For completeness, the results using a lower intrinsic permeability are shown in Appendix C for both the medium and large samples. These overestimate the expected shrinkage.

## 6.3 Summary

In this chapter, the experimental tests necessary to calibrate the unknown parameters in the poromechanical equations are shown. Flexural tests are needed to determine the Young's modulus and to compute the bulk modulus, which in turn is used to calculate the Biot parameter. Further experiments to determine the water accessible porosity and dry density by means of weight changes are carried out.

Moreover, experimental tests to determine hygral properties, namely, gravimetric measurements with dynamic vapor sorption analysis are carried out to determine the relationship between moisture content and relative humidity. This relationship is rearranged in terms of pore pressure with the help of the Kelvin-Laplace equation. Then, the obtained curve is used to determine the van Genuchten parameters through best fitting.

Simulations of the RH tests are carried out and compared to the experimental RH evolution along the sample. The ambient RH is imposed as boundary condition for drying the sample. The best fitted range of intrinsic permeabilities is further refined in the free shrinkage simulations.

The either directly or indirectly determined input parameters and boundary condition

(flux) are adopted for the simulations of the drying-shrinkage tests, e.g. tests for the determination of the mass loss for each sample. The best agreement is found for the medium sample with $k_i = 1 \times 10^{-21}$ m$^2$.

Finally, the free shrinkage simulations with input data calibrated up to 28 days are used to predict long term shrinkage and show very good agreement with the experimental results up to 1 year.

# Chapter 7

# Experimental calibration of fracture parameters for cement mortar

In this chapter, the three-point bending tests and the compact tension tests are described. These experiments are carried out to determine the tensile strength of the material. Furthermore, the compact tension test is reproduced numerically such that the fracture energy and length scale parameter in the phase-field fracture model are calibrated.

## 7.1 Experiments

The cement mortar with w/c ratio of 0.5 and 40% aggregates in volume described in the previous chapter is utilized in the preparation of the samples for the bending and compact tension tests.

### 7.1.1 Three-point bending tests

The medium prismatic samples tested under three-point bending in the elastic range as presented in Subsection 6.1.1 are further tested up to failure. The test follows the DIN EN 196 [51]. Here, the prismatic sample is placed on two rolling bars and loaded by one upper rolling bar up to failure. The measured flexural strength is assigned as value for the tensile strength $\sigma_{t_{28d}}$=6.8 $\pm$ 0.7MPa.

### 7.1.2 Compact tension tests

The compact tension test (CTT) described in [48] is chosen for the evaluation of the fracture behavior of the mortar. This test allows for stable crack growth and to obtain

fracture parameters from inverse analysis as in the wedge splitting test [141]. The mix is prepared and cast in a mold, which is removed after one day of hardening. During hardening, the sample is placed in a room with constant $T = 20^o$C and RH= 70%. The specimen dimensions are shown in Fig. 7.1. The sample is held with the help of a pin inserted in the lower hole. Another pin is inserted at the upper hole such that a displacement, in quasi-static conditions, can be applied. The force-displacement curve is plotted during the test. Furthermore, the test is recorded with digital image correlation (DIC) in order to follow the crack evolution during testing.

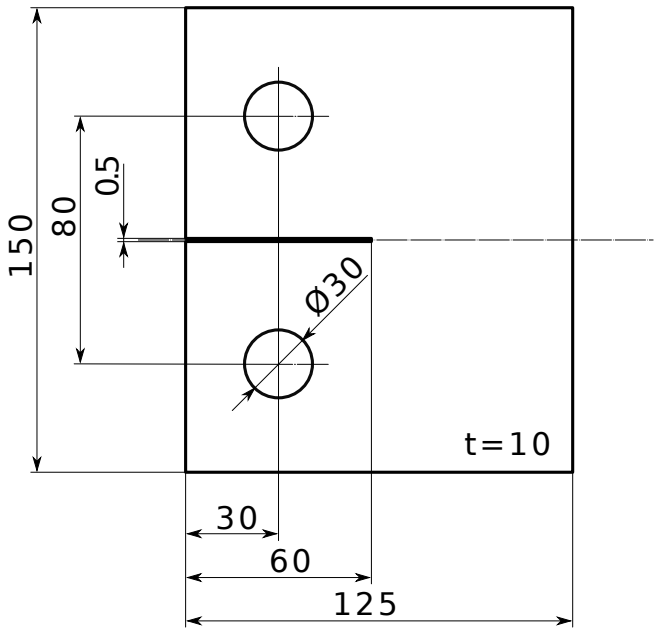


**Figure 7.1:** Compact tension test specimen (dimensions in millimeters) [35].

The experimental results are shown together with the numerical results in Section 7.2. The fracture energy is determined indirectly through calibration with the fracture model in use. More detailed information is provided in the following numerical subsection.

## 7.2 Calibration

The experimental results are used to calibrate the fracture parameters with the help of the homogeneous solution of the phase-field model, equation proposed in [29]. The homogeneous solution, Eq. (3.4.12), is rearranged in terms of the length scale parameter $\ell$

$$\ell = \left(\frac{9}{16\sigma_t}\right)^2 \frac{\mathcal{G}_c E}{6},$$

where only $\mathcal{G}_c$ needs to be calibrated, since $\sigma_t$ and $E$ are already determined experimentally.

For the mechanical simulation a two-dimensional model with local refinement near the region where cracking is expected to occur is prepared. The local refinement contains elements with at least half of the size of the governing length scale. The simulation setup is shown in Fig. 7.2. The lower node of the lower hole is held with $\mathbf{u} = 0$. This is the touching point between pin and hole in the experiment. The mechanical load is applied with displacement increments $\Delta\mathbf{u} = 2 \times 10^{-8}$m per time step to ensure that the process is slow. The displacement-driven load is applied at the upper node of the upper hole.

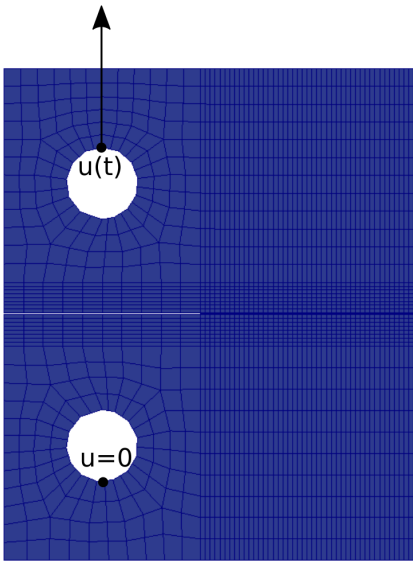


**Figure 7.2:** Simulation setup for compact tension test. The shown mesh is coarse to improve the visualization. The model is further refined to resolve with the computed length scale parameter.

The numerically obtained force-displacement curves are compared with the experimental curves. The fracture energy is adjusted and new simulation sets are carried out until the maximum load shows agreement with the experiments. Table 7.1 shows a range of fracture energies obtained after the calibration. The ranges for the length scale parameter $\ell$ are computed for each estimated $\mathcal{G}_c$. This range results from the combination of the tensile strength and Young's modulus together with their deviations, e.g. $\ell_{min}$ utilizes $\sigma_{t_{max}}$ and $E_{min}$ while $\ell_{max}$ utilizes $\sigma_{t_{min}}$ and $E_{max}$ as values in the equation.

The experimentally and numerically obtained force-displacement curves are shown in Fig. 7.3. The curves from the simulation with each $\mathcal{G}_c$ and $\ell$ lie within the experimental ranges.

**Table 7.1:** Fracture energy calibration.

| $\mathcal{G}_c$ | $\ell_{min}$ | $\ell$ | $\ell_{max}$ |
|---|---|---|---|
| 6 N/m | 0.17mm | 0.18mm | 0.18mm |
| 8 N/m | 0.23mm | 0.23mm | 0.24mm |

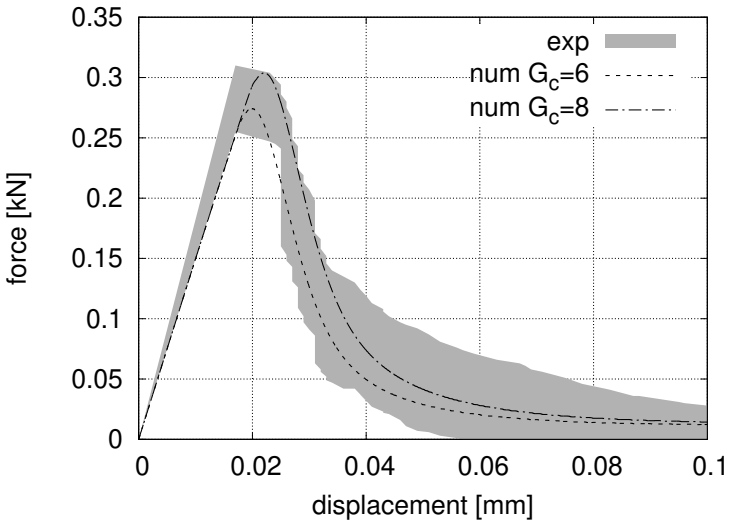


**Figure 7.3:** Experimental and numerical force-displacement curves.

The phase-field results concerning crack initiation and propagation for the setup with $\mathcal{G}_c = 8\text{N/m}$ are shown in Fig. 7.4(a)-7.4(b), respectively. The final pattern shows good agreement with the experimental results provided by DIC in Fig. 7.4(c). Note that the experimental crack is not perfectly straight due to fabrication and cutting of the sample as well as due to the presence of aggregates (heterogeneities). The pattern does not change for $\mathcal{G}_c = 6\text{N/m}$ and the results are not shown for conciseness. Furthermore, the simulation is repeated with 10 staggered iterations, which does not affect the force-displacement curve nor the crack pattern.

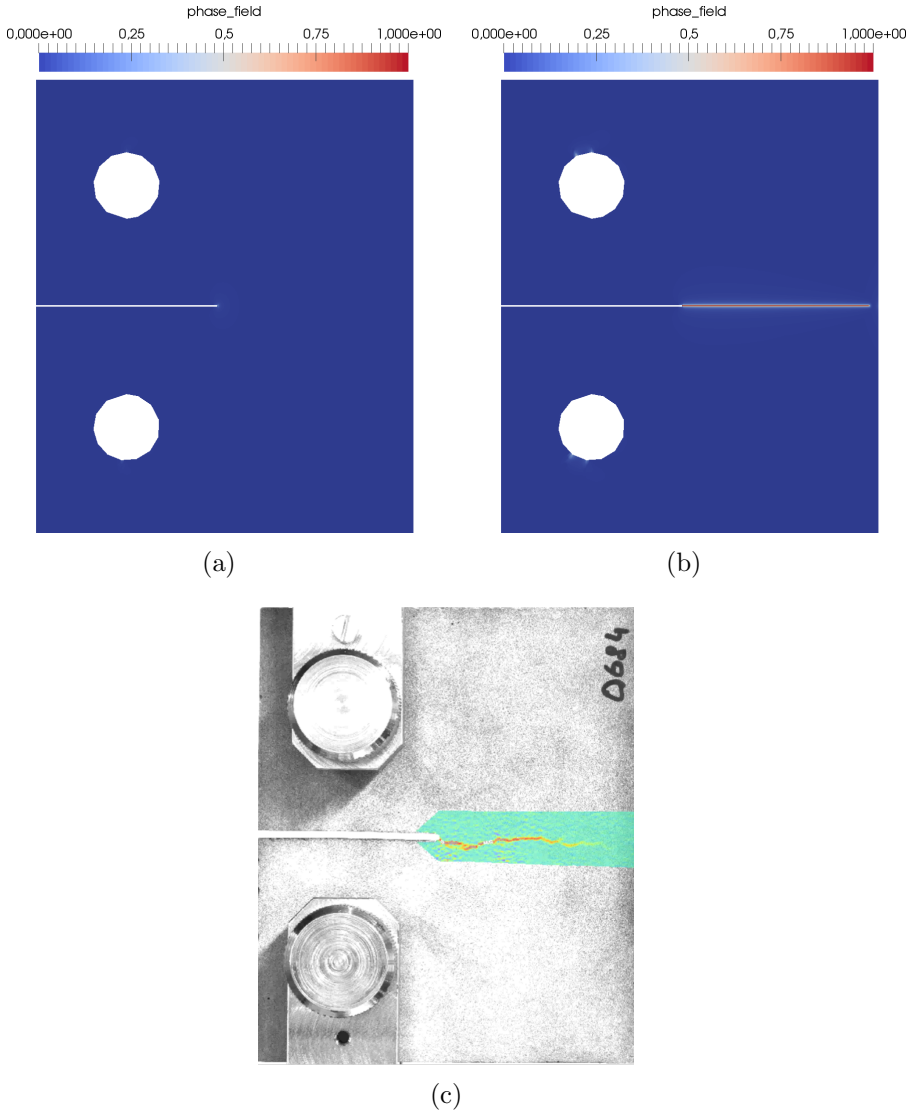


**Figure 7.4:** (a) Crack initiation and (b) final crack pattern using the phase-field model. (c) Final experimentally observed crack pattern from DIC.

The length scale $\ell = 0.23$mm and fracture energy $\mathcal{G}_c = 8$N/m obtained in this study are used as input in the further tests of Chapter 8.

## 7.3 Summary

The experimental campaign initiated in Chapter 6 is complemented with the calibration of the fracture properties. Here, a pure mechanical model composed by the equilibrium and the phase-field evolution equations is adopted.

The tensile strength is obtained from three-point bending tests. The fracture energy

is calibrated from the compact tension tests using the model. Then, the homogeneous solution of the phase-field model for brittle fracture is utilized to obtain the length scale parameter. The compact tension test is modeled with the equilibrium and phase-field evolution equations. Different values of the fracture energy are tested up to agreement between the numerical and experimental force-displacement responses.

# Chapter 8

# Experimental validation of the poromechanical-phase-field model

The poromechanical model was calibrated and validated with the free shrinkage test in Chapter 6. Then, the fracture model was calibrated in Chapter 7. All obtained parameters are now utilized in the validation of the complete poromechanical-phase-field model. For that, the restrained ring test is chosen. This chapter concentrates on the description of this test for a cement mortar with w/c 0.5 and 40% aggregates. The experiment consists on a restrained shrinkage setup which combines the effects of autogenous and drying shrinkage as well as of the mechanical restraint. Two experimental setups are investigated to take into account different drying conditions and their corresponding shrinkage evolution. These setups are reproduced computationally with the model developed in Chapter 3.

## 8.1 Experiments

In engineering constructions, a natural volumetric expansion of cementitious materials is limited due to the presence of restraints such as joints and adjacent structures. At early ages, e.g. during maturing of the material and in the first days after casting, deformation is caused due to the chemical reactions and autogenous shrinkage, changes in temperature as well as drying shrinkage [95, 21]. For this reason, it is important to carry out experimental tests with a restrained setup. These can provide information about the development of residual stresses and assist in predicting the material behavior and cracking risk of the material when its volume change is prevented.

According to [33], restrained tests in cementitious materials can be classified into three groups:

- Shrinkage restrained in one-dimension

- Shrinkage restrained in two-dimensions
- Ring test [150, 133, 111, 154, 167]

In the one-dimensional, or longitudinal, configuration, the restraint is applied at the extremities of the sample in order to hinder its natural length change. This procedure complements free shrinkage analysis and is commonly utilized to assess the cracking risk of cementitious materials [15, 26].

In the case of two-dimensional restraint during drying shrinkage, the sample deformation is hindered both in longitudinal and perpendicular directions, e.g. by a mould or substrate. In this configuration, the developed cracks are perpendicular to the drying surface and can form a network on the drying surface [21, 121, 142, 155].

A variable and more complex degree of restraint can be obtained with the ring test [33, 133]. In this type of test, crack development occurs not only due to the external mechanical restraint, but also due to the geometric setup. Furthermore, different drying conditions and their effect on the deformation and consequently, on the cracking risk can be analyzed. Here, any type of mixture can be tested and the age of the sample can vary. The restrained ring test is cheaper and easier to perform than one-dimensional active setup and passive one. This is due to the fact that it does not require a massive setup to record the strains. Moreover, it can be also used to estimate tensile and viscoelastic properties [66].

Fundamental components of the ring test are the material in study, one internal and/or one external restraining ring made of a material less susceptible to thermal deformation such as steel [76] or Invar [133] and strain gauges. Figure 8.1 shows the generic configuration of the test. The steel or Invar ring is custom made, which increases the costs of the testing setup.

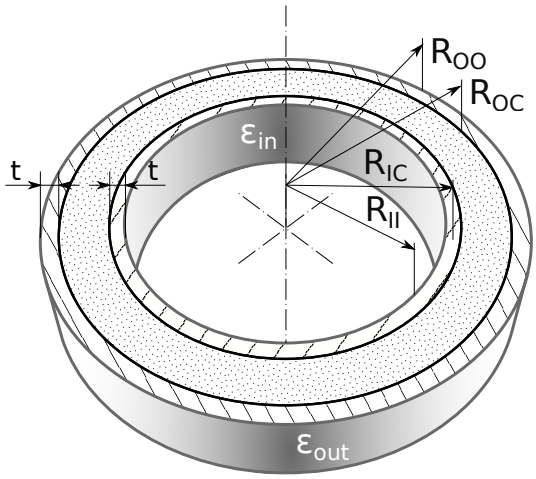


**Figure 8.1:** Geometry and generic experimental setup of the ring test. Adapted from [133].

According to the figure, the outer radius of the restraining ring corresponds to the inner

radius of the mortar ring $R_{IC}$. Four strain gauges measure the current strain $\varepsilon_{IN}$ in circumferential direction and are located at the inner circumference of the restraining ring with radius $R_{II}$.

The geometrical parameters of the test carried out in this work (corresponding to Fig. 8.1) are summarized in Table 8.1.

**Table 8.1:** Geometrical parameters of the ring test and Young's modulus of the restraining ring.

| $R_{II}$ | $R_{IC}$ | $R_{OC}$ | $E_I$ |
|---|---|---|---|
| 0.146m | 0.165m | 0.215m | 141GPa |

In this work, the mortar described in Chapter 6 is cast in a plastic mold with inner ring made of Invar with Young's modulus $E_I = 141$GPa and Poisson's ratio $\nu_I = 0.3$. Invar is chosen since it has lower coefficient of thermal expansion than steel and for this reason, less susceptible to the thermal deformation during hydration of the mortar [133]. The outer restraint is not applied in this work since no expansion of the material expected after the specimen is opened to drying at 28 days.

When cast in the mold, the samples are kept in sealed conditions for 28 days such that restrained autogenous shrinkage strain development is measured, Figs. 8.2(a) and 8.2(b). The geometrical parameters of the test together with the average strain measured during the ring test $\varepsilon(t)$ and $E_I$ are used to compute the circumferential residual stresses $\sigma_\theta$ according to the expression in [133], as

$$\sigma_\theta = -\varepsilon(t) E_I \frac{R_{IC}^2 - R_{II}^2}{2R_{IC}^2} \frac{R_{OC}^2 + R_{IC}^2}{R_{OC}^2 - R_{IC}^2}. \tag{8.1.1}$$

Note that the measured circumferential strain $\varepsilon(t)$ is negative, since it results from the pressure exerted by the sample on the restraining ring [133]. For this reason, a positive circumferential residual stress results during shrinkage of the sample. The computed stress are compared with the values of the tensile strength of the sample in Sections 8.1.1 and 8.1.2.

When the samples are 28 days old, the molds are removed and prepared according to the desired drying test configuration, Fig. 8.2(c). Note that the inner restraint of the rings is neither removed during hardening nor later, during the test, Fig. 8.2(d). During hardening and testing, the samples are kept in a room with monitored and approximately constant $T = 20 \pm 0.5^o$C and $RH = 70 \pm 3\%$.

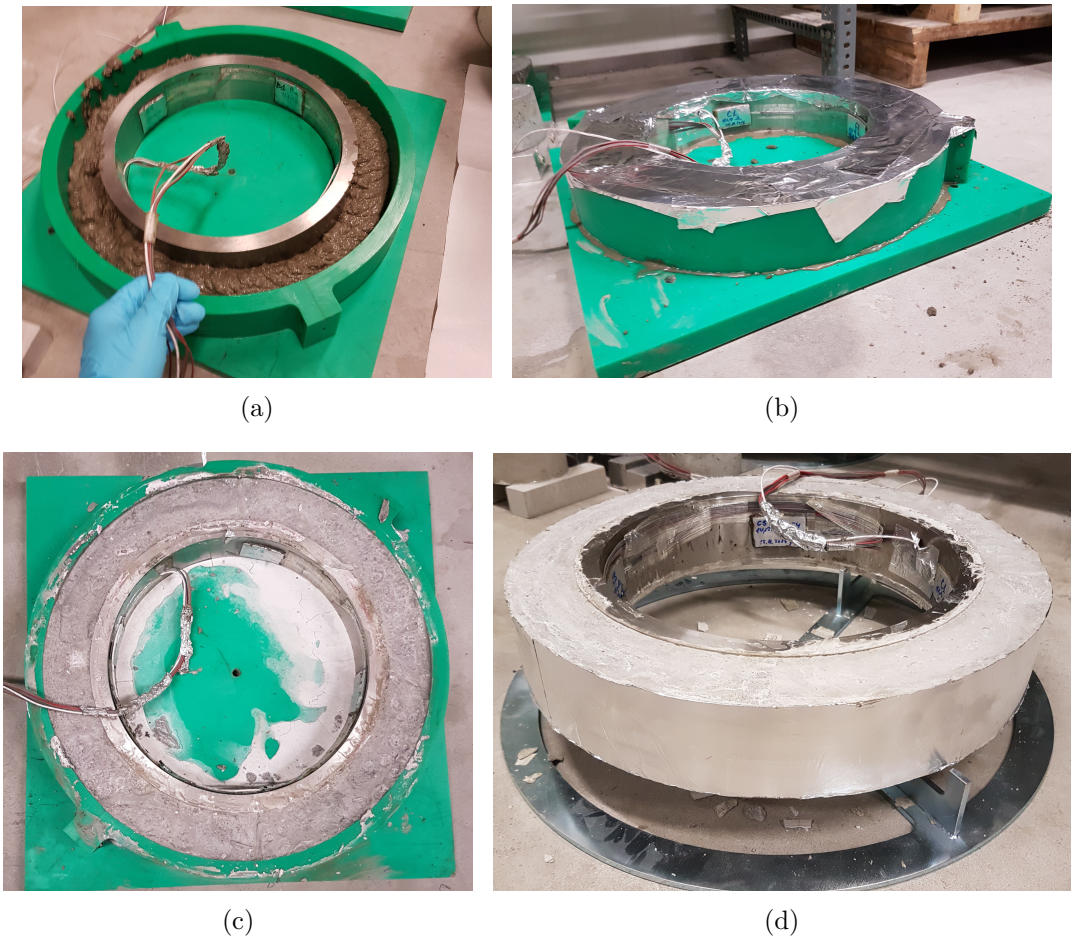

(a) (b)

(c) (d)

**Figure 8.2:** Specimen preparation for the ring test.

In this thesis, two configurations are tested: uniform and non-uniform drying with respect to the radial direction. Two samples are tested per configuration. Both configurations are expected to behave similarly up to 28 days, before the sealing is removed and each setup is prepared. For a direct visualization and comparison of the results, the average strain development measured by the four strain gauges is shown for all tested sample in Fig. 8.3.

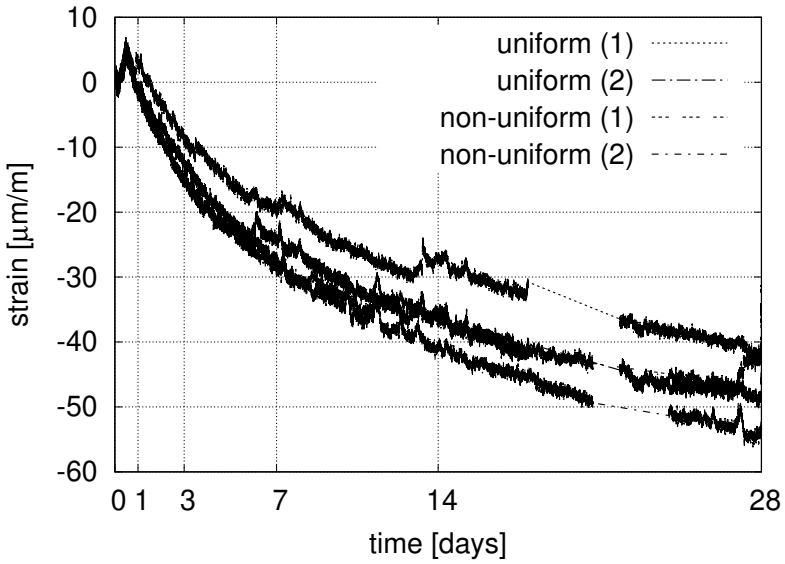


**Figure 8.3:** Strain development in the ring test up to 28 days for uniform and non-uniform drying configurations.

In the first day, the mortar expands slightly. Up to 28 days, the measured strains are due to autogenous shrinkage and due to the mechanical restraint. Cracks are not observed, which is assessed both by the visual examination of the sample during the preparation for the next part of the test and by the strain development curve, which does not present an abrupt change of the measured values. After 28 days, the samples are prepared according to each desired test configuration. Common to both setups is the development of a single crack onset during drying as shown in Fig. 8.4. Particular observations of each test case are described in the following.

**Figure 8.4:** Ring cracked between 26 and 45 hours after opening when drying from the outer circumference.

### 8.1.1 Uniform drying

After 28 days, the mold and aluminum foils are removed. Then, the mortar ring is sealed around its outer circumference such that the drying occurs from the upper and

lower surfaces as shown in Fig. 8.5.

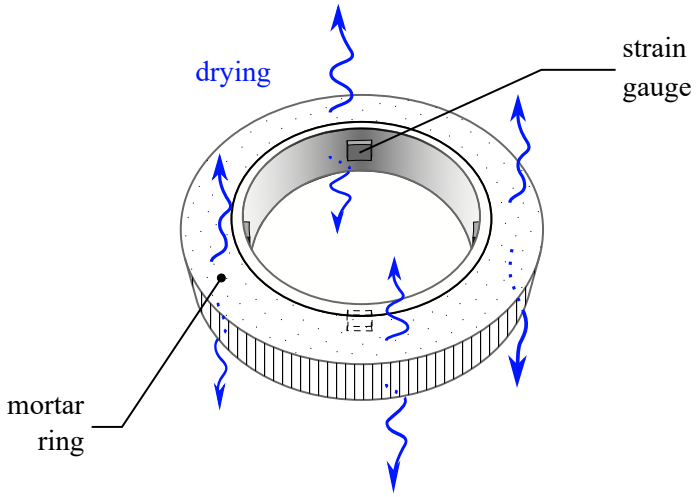


**Figure 8.5:** Experimental setup of ring test drying from the upper and lower surfaces.

This configuration induces uniform drying along the radial direction [76, 154]. The stress development after uniform drying starts is shown schematically in Fig. 8.6. The mortar ring exerts compression around the inner ring which hinders the free movement of the sample. This results in a large tensile stress near the inner circumference. Due to this, cracking is expected to start from the inner circumference and propagate towards the sealed part.

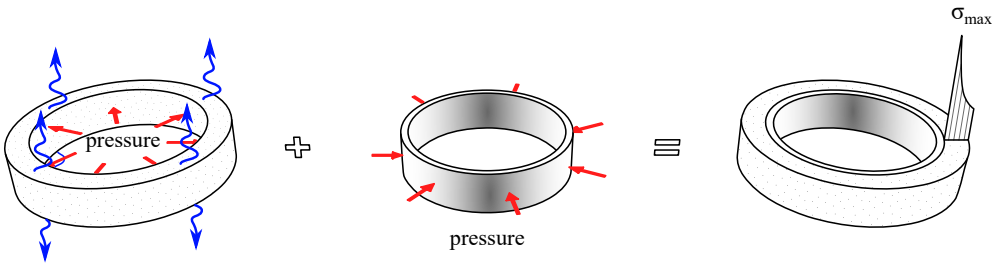


**Figure 8.6:** Stress distribution due to drying from upper and lower surfaces. Adapted from [76].

The measured average strain evolution during uniform drying of the restrained mortar ring is plotted in Fig. 8.7. Due to demolding, sealing and re-positioning of the samples, a slight perturbation of the curve is observed near 28 days. Note that the measured strains do not increase remarkably after drying starts and are approximately uniform after the curve stabilizes. In the uniform drying configuration, cracking occurs at approximately 5 and 8 days in each of the two samples after they are opened, denoted by the sudden drop of the stress in the graph. The residual tensile stress at cracking $\approx 3.25$MPa represents 48% of the tensile stress.

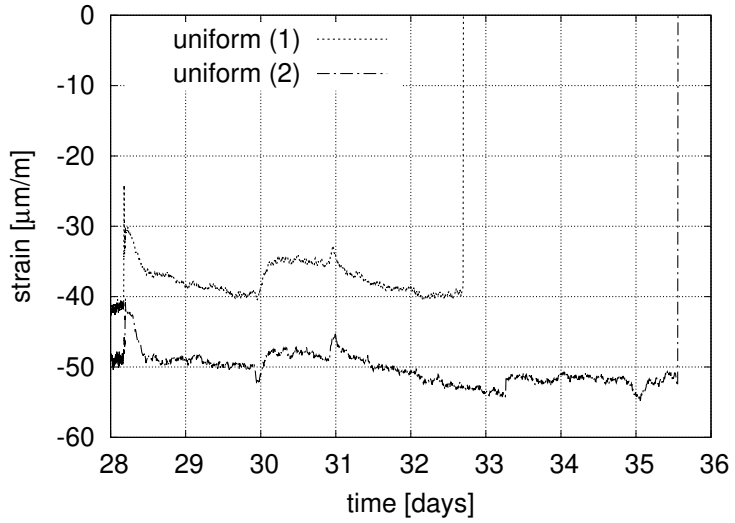


(a)

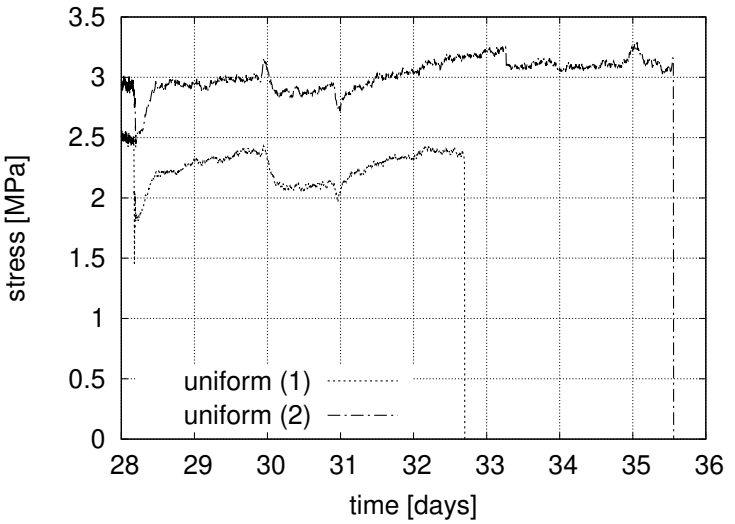


(b)

**Figure 8.7:** Circumferential (a) strain development (average of four strain gages) during ring test with drying from upper and lower surfaces for two mortar samples after drying starts and (b) corresponding residual stress development. The samples remain sealed for 28 days, when they are opened for drying. Cracking occurs between the fifth and eighth day of drying.

### 8.1.2 Circumferential (non-uniform) drying

After the samples are cured for 28 days under sealed conditions, the mold and aluminum foils are removed. Then, the ring is sealed on its upper and lower parts such that drying occurs from the outer circumference as shown in Fig. 8.8.

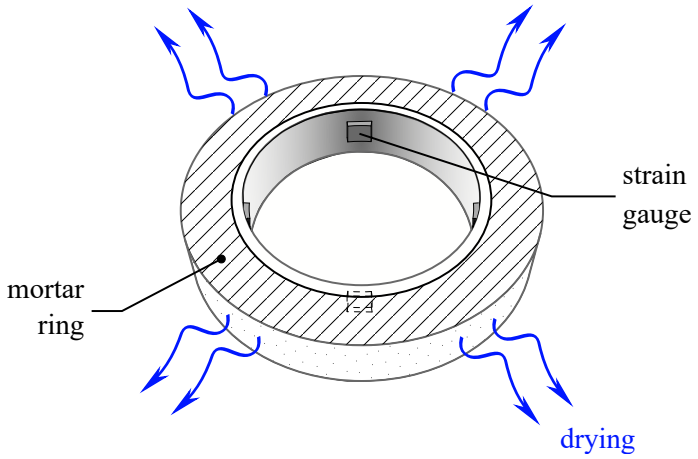


**Figure 8.8:** Experimental setup of ring test drying from the outer circumference.

This test aims at adding the strain contribution of non-uniform drying along the radial direction. Figure 8.9 shows the stress development for this configuration schematically. Similarly to the previous uniform drying configuration, there is the contribution of the mechanical restraint. When the ring starts to dry, moisture gradients develop and generate a tensile stress, which is larger in the region near the drying front. Due to the larger pressure gradient at the outer drying circumference, the crack is expected to start at this region and to propagate inwards.

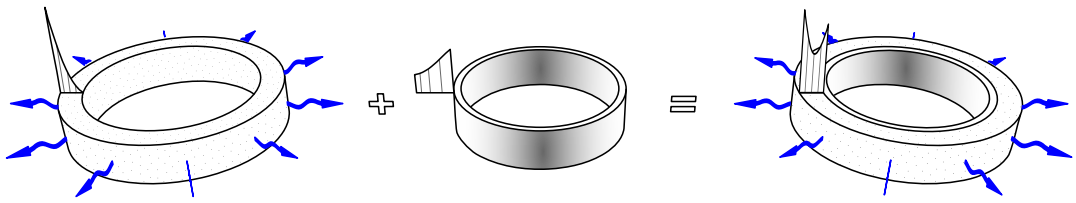

**Figure 8.9:** Stress distribution due to drying from the outer circumference. Adapted from [76].

Figure 8.10 shows the experimental average strain development of the two samples after 28 days. Due to sample preparation, a slight perturbation of the measured strain is observed. The measured strain does not increase remarkably after the sample starts to dry. The large drop of the stress indicates cracking at approximately 1 and 2 days after drying starts for each tested sample. The residual tensile stress at cracking $\approx 3.5$MPa represents 51% of the tensile stress.

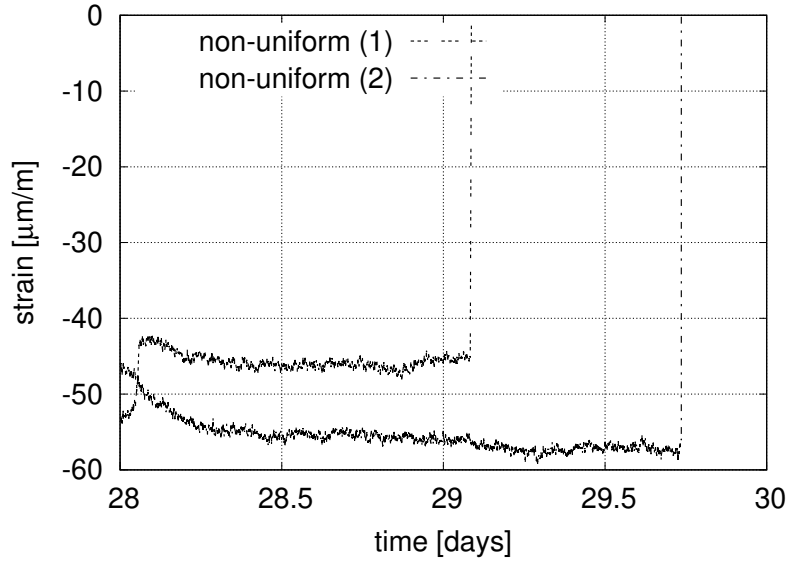


(a)

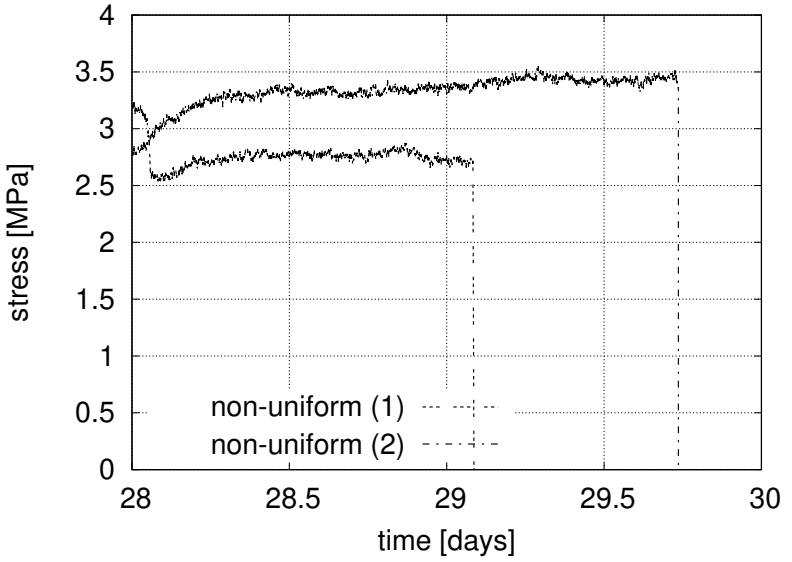


(b)

**Figure 8.10:** Circumferential (a) strain development (average of four strain gages) during ring test with circumferential drying for two mortar samples after drying starts and (b) corresponding residual stress development. The samples remain sealed for 28 days, when they are opened for drying. Cracking occurs between the first and second day of drying.

## *Remarks:*

- The similar strain developments after the samples are allowed to dry imply that the stress due to circumferential drying is not very significant in comparison to

that due to uniform drying.

- This fact may indicate that the largest contribution to the strain development is due to the inner restraint (mechanical) and to autogenous shrinkage (chemical).
- On the other hand, it may also indicate that the samples avail less water for drying after the long period of sealing of 28 days, where the water is consumed. For this reason, the drying front is not contributing to large strain development in the sample. Further experiments are required to evaluate this hypothesis, e.g. by unsealing the samples before 28 days and allowing them to dry.
- The simulations in the following are utilized to identify the contribution of the uniform and non-uniform drying to the strain development and with that, assess the cracking risk.

## 8.2 Simulations

In order to model the ring test, a three-dimensional model consisting of one-eight of the ring is prepared. The colored surfaces in Fig. 8.11 indicate the applied boundary conditions and their location. The inner part of the ring is mechanically restrained. Its sides and bottom nodes, i.e. mid cross-section of the complete sample, are assigned symmetry boundary conditions. The drying boundary condition is applied in terms of the ambient RH=70%. This value is imposed at the upper surface in case of uniform drying and on the outer circumference in case of non-uniform drying.

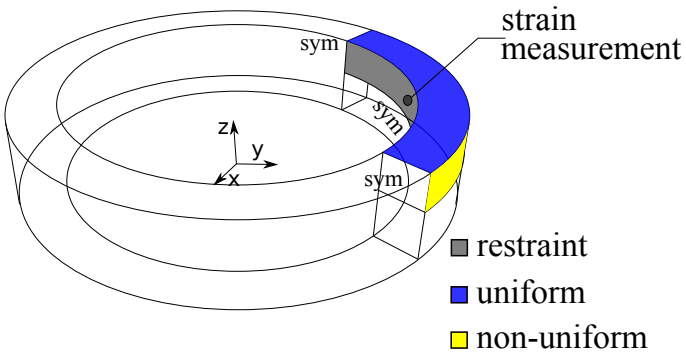


**Figure 8.11:** Three-dimensional simulation setup of the ring test. Symmetry boundary conditions are specified in all symmetry planes. The surface in blue color represents the specified drying surface for the uniform configuration while the surface in yellow specifies the drying surface during non-uniform (circumferential) drying.

Table 8.2 summarizes the input parameters needed in the simulation of the ring test.

**Table 8.2:** Parameters utilized in the modeling of the ring test.

| $E$ | $\nu$ | $\alpha$ | n | $\rho_d$ |
|---|---|---|---|---|
| 25.6 GPa | 0.2 | 0.684 | 0.139 | 2007 kg/m$^3$ |
| $k_i$ | $\alpha_{vG}$ | $n_{vG}$ | $S_r$ | |
| $1 \times 10^{-21}$m$^2$ | $3.5863 \times 10^{-4}$m$^{-1}$ | 2.6293 | 0.67881 | |

In the first part of the simulation, the poromechanical part is uncoupled ($\alpha = 0$) and the pure mechanical case is calculated. Here, a shrink-fit is performed. The restrained surfaces should achieve a total displacement magnitude of 2.4 $\mu$m which corresponds to the experimental strain at 28 days (48 $\mu$m/m) multiplied by the length of the sample (0.05 m) due to mechanical restraint and autogenous shrinkage before allowing the specimen to dry. The total displacement applied to the inner circumference is achieved after 240 load steps. The results are shown in Fig. 8.12.

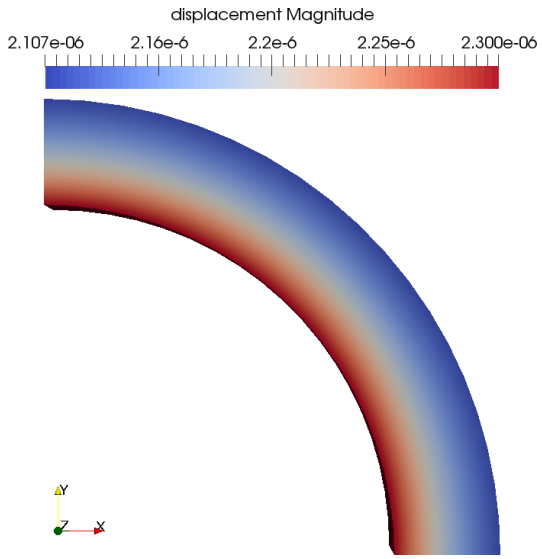


**Figure 8.12:** Magnitude of the displacements in the mechanical simulation.

When the elastic simulation finishes, the simulation is re-coupled, i.e. $\alpha = 0.684$ with $\Delta t = 10$ seconds. Note that the achieved displacement is held constant at the inner restrained surface. This time corresponds to the opening time of 28 days to allow for drying.

As mentioned in Chapter 6, the numerical framework of this thesis does not account for relaxation nor for the effects of autogenous shrinkage. This implies that the mechanical response of the model may overestimate the experimental results. To accurately predict the experimental response, the mathematical framework should also account for the chemical reaction, the relaxation and the thermal behaviors [15, 58, 59, 161].

In both studied cases, the properties of the mix at 28 days are considered as starting point for the simulations.

### 8.2.1 Uniform drying

The pore water pressure obtained through the simulation after six hours of drying is shown in Fig. 8.13. This early time step is chosen due to the approximately uniform strain development observed in the experiments after drying starts. The smallest pressure is found at the boundary, which corresponds to the applied RH=70%. The pressure develops uniformly along the height of the sample.

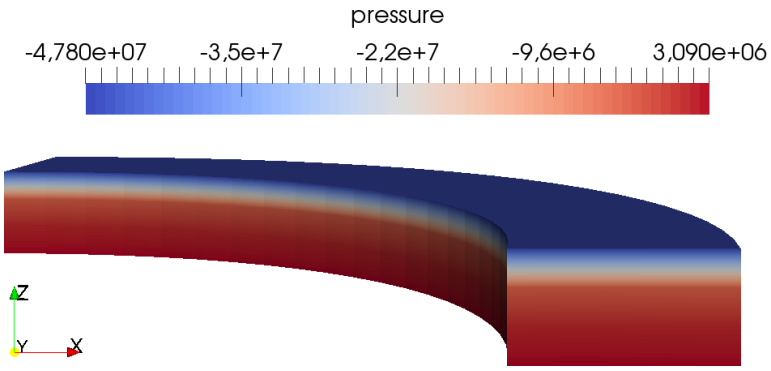


**Figure 8.13:** Water pressure [$\mathrm{N\,m^{-2}}$] distribution after six hours of drying from upper and lower layers.

The total displacement of the sample scaled by a factor of 200, after six hours of drying is shown in Fig. 8.14 denoting shrinkage of the upper layer.

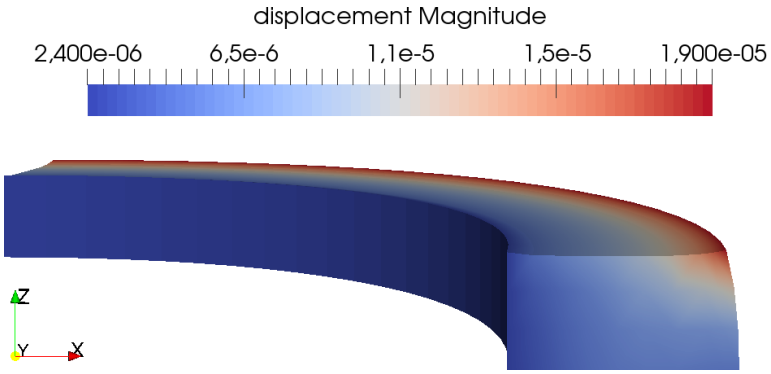


**Figure 8.14:** Displacement magnitude of the uniform ring test. The visualization is scaled by a factor of 200.

The numerical strains at the inner and outer circumference at the center of the sample in the $xy$-plane are shown in Table 8.3.

**Table 8.3:** Numerical strains at the inner and outer circumference during uniform drying at six hours.

| $\varepsilon(\mathrm{R_{IC}})$ | $\varepsilon(\mathrm{R_{OC}})$ |
|---|---|
| $-51\mu\mathrm{m/m}$ | $-12\mu\mathrm{m/m}$ |

Substituting these results in Eq. (8.1.1), the circumferential stress at the inner circumference is larger than that at the outer circumference. The results Table 8.3 indicate that cracking might start from the inner circumference in the uniform case. They will be compared with the response of the non-uniform case.

### 8.2.2 Circumferential (non-uniform) drying

After six hours of drying, the pressure develops as shown in Fig. 8.15.

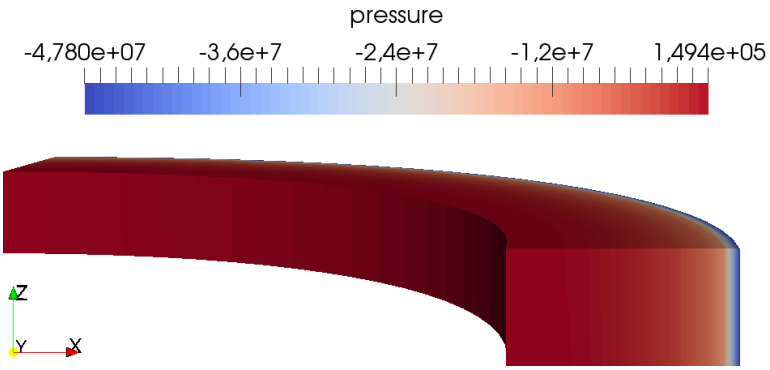


**Figure 8.15:** Water pressure [$\mathrm{N\,m^{-2}}$] distribution after six hours of circumferential drying.

The displacement of the sample after six hours of drying is shown in Fig. 8.16 denoting shrinkage of the external circumferential layer. The magnitude of the displacement is smaller when compared to the top-bottom case.

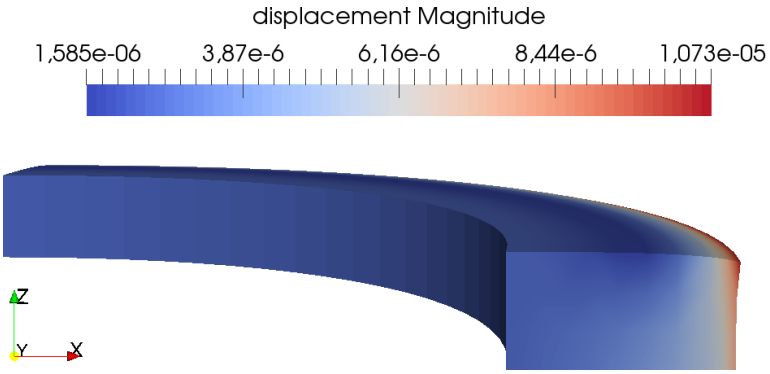


**Figure 8.16:** Displacement magnitude of the circumferential ring test. The visualization is scaled by a factor of 200.

The numerical strains at the inner and outer circumference at the center of the sample in the $xy$-plane are shown in Table 8.4.

**Table 8.4:** Numerical strains at the inner and outer circumference during non-uniform drying at six hours.

| $\varepsilon(\mathrm{R_{IC}})$ | $\varepsilon(\mathrm{R_{OC}})$ |
|---|---|
| $-3.76\mu\mathrm{m/m}$ | $-239\mu\mathrm{m/m}$ |

The substitution of these results in Eq. (8.1.1) indicate that the stress at the outer circumference is much larger than at the inner circumference. These results confirm the contribution of the circumferential drying on the stress response and indicate the possibility of cracking starting at the outer circumference.

### 8.2.3 Preliminary model validation

The small length scale parameter obtained in the calibration (Chapter 7) requires a fine mesh and consequently induces a large number of degrees of freedom. The solution scheme of the algorithm utilizes a direct solver, which has a limitation regarding the number of degrees of freedom. For this reason, a two-dimensional model is prepared. This model is used as a proof-of-concept to evaluate the ability of the framework to predict cracking in the current experimental setup.

The parameters in Table 8.2 are imposed. In order to reduce the number of degrees of freedom of the model, the length scale is multiplied by a factor of 10, i.e. $\ell = 0.002$ m. This reduction influences the fracture energy directly according to Eq. (3.4.12) (also discussed in Chapter 7). In order to allow for earlier cracking, the fracture energy is decreased by a factor of 10, i.e. $\mathcal{G}_c = 0.8$ N/m. The decrease of the fracture energy leads to earlier cracking (as shown in Chapter 5).

The crack phase-field results in Fig. 8.17 show that the model is able to reproduce shrinkage-induced cracking. Up to 10 hours, the phase-field increases uniformly at the outer circumference, Fig. 8.17(a) At 12 hours, cracks propagate at the corner of the symmetric sample due to stress concentration provided by the boundary conditions, Fig. 8.17(b). Then, at 14 hours, a crack initiates at the outer circumference, Fig. 8.17(c). This crack propagates within 5 minutes along half of the thickness of the sample. No new cracks initiate up to 20 hours of drying as shown in Fig. 8.17(d).

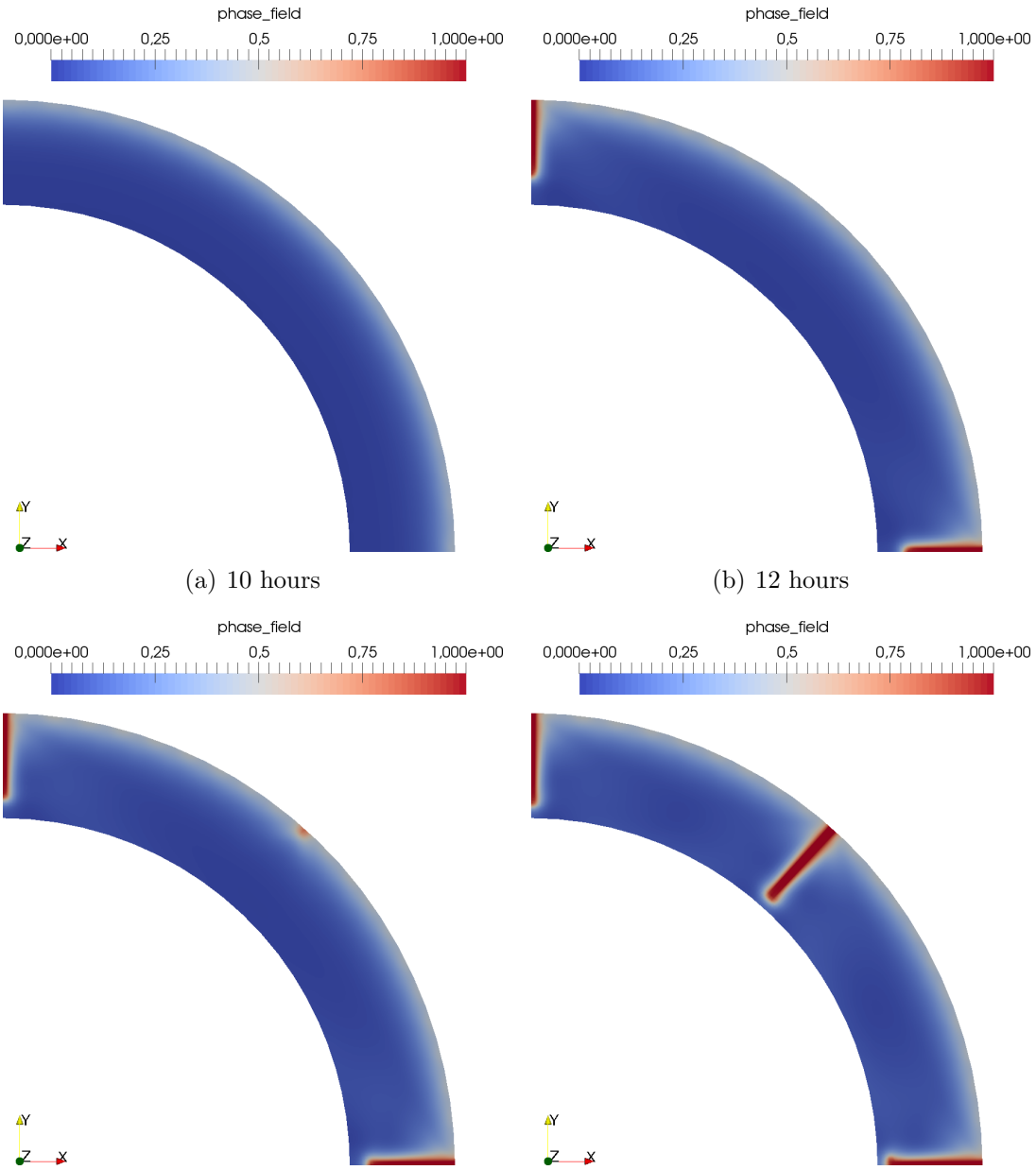


(a) 10 hours (b) 12 hours

(c) 14 hours (d) 20 hours

**Figure 8.17:** Phase-field evolution of the ring sample at (a) 10, (b) 12, (c) 14 and (20) hours of drying.

To be able to predict cracking quantitatively, the model needs to be extended to account for stress relaxation. Furthermore, a simulation with elastic restraint or with a contact formulation to an explicitly described restraining ring would decrease the stress concentrations and thus prevent cracking at the corners. This alternative would be more realistic, since the sample is not perfectly restrained during the experiment (see [133] concerning the degree of restraint). From the numerical point of view, an adaptive remeshing approach needs to be developed and iterative solvers need to be

used.

## 8.3 Summary

The restrained ring test is described in this chapter. An inner ring made of Invar is utilized to mechanically restrain a ring made of the mortar used in this work.

After 28 days of hardening in sealed conditions, the mortar rings are opened and re-sealed according to the desired testing configuration. Two setups are proposed to assess the influence of the drying conditions on crack development. The first configuration deals with uniform drying, where the upper and lower surfaces are allowed to dry and the second configuration with non-uniform, or circumferential drying. The onset of one crack is observed at each setup.

The crack initiates at the inner circumference in the uniform drying case and at the outer circumference in the non-uniform drying case. The mechanical restraint contributes to stress development in both configurations. For the non-uniform setup, the moisture distribution due to drying from the outer circumference contributes additionally to the stress development.

The poromechanical-phase-field framework shows good qualitative agreement with the expected and experimentally observed fracture behavior due to drying. The modeling of the coupled problem of the restrained ring test needs to be complemented with thermal, viscous and chemical related aspects.

# Part V

# Epilogue

# Chapter 9

# Conclusions and future research

## 9.1 Conclusions

This research work has focused on the modeling of the coupled phenomena of drying, shrinkage and cracking in porous media. For that, the poromechanical formulation and the phase-field approach to brittle fracture were combined and adapted to the context of variably saturated porous media. The governing equations, constituted by the equilibrium, the mass balance of pore water and the crack field evolution equations, are completed by kinematic and constitutive relationships. The coupling sources of the model in the present formulation are given by the concept of effective stress and by the relationship between the fracture energy and the water content. First steps were taken to improve the coupling between the crack phase-field and the pressure field. These are based on experiments using the neutron imaging technique and are expected to provide input data for modeling the effect of cracking on the drying process.

The equations of the framework were treated numerically and implemented in the `deal.II` library. The phase-field evolution equation was solved separately, with a staggered scheme. This procedure is expected to always converge, however it can require a large number of iterations. To overcome this issue, small time steps were chosen and the system was solved explicitly. Then, the poromechnical part was solved monolithically. For that, the finite elements need to satisfy the LBB condition, which can lead to an increase of the computational cost due to the polynomial order of the elements.

The first verification of the numerical framework was related to the consolidation and desaturation problems. These results were compared to analytical solutions and numerical benchmark results from the literature and showed very good agreement. More elaborated test cases inspired by experiments from the literature and related to desiccation in soils were simulated and showed good qualitative agreement with experimental observations. To complement the set of the tests and to evaluate the ability of the model in predicting more complex crack patterns and networks, a three-dimensional

setup inspired by experiments from the literature was computed. These steps concluded the verification of the model and desiccation induced-cracking could be reproduced in one-, two- and three-dimensions.

The necessity of using fine meshes to resolve the crack phase-field denoted one downside in the model. Fine meshes are associated with a large number of degrees of freedom, which consequently increases the computational cost. First steps were taken to improve the solution by using an adaptive refinement scheme, which could reduce the computational time and should be developed further.

An original experimental campaign with cement mortar was carried out in order to obtain experimental data for validation. Here, the poromechanical parameters, fracture properties and boundary conditions for the model were either determined directly with the experiments or calibrated with simulations. The restrained ring test was chosen for validation of the framework. The model confirmed the cracking risk of two different drying configurations. Furthermore, it could predict cracking qualitatively in the mortar ring due to circumferential drying. Cracking may be predicted quantitatively when using the complete model once the numerical solution strategy is improved, i.e. by using iterative solvers and adaptive schemes, and the calibrated fracture energy and length scale associated with large number of degrees of freedom can be solved for. This is expected to happen since (i) cracking was predicted quantitatively in the compact tension test and (ii) shrinkage was predicted quantitatively in short- and long-term.

In conclusion, this research project contributed with a modeling framework for shrinkage-induced cracking in variably saturated porous media. The modeling was improved with experimental observations, e.g. dependency of the elastic properties on hydraulic variables, and with experimental data during the calibration and validation. The coupling terms and solution schemes need further improvement. The results indicated a wide applicability of the framework in dealing with different phenomena such as desaturation, desiccation and shrinkage (free and restrained). They also signalized the generality of the framework, since it was applied to model different materials.

## 9.2 Future research

Research into improving the coupling between cracking and pore water flow is underway. For that, the experimental results using neutron radiography technique and partially shown in Appendix A need to be further postprocessed. With these data, a relationship between the crack length and the flow regime should be established. Furthermore, the influence of the crack width and crack tortuosity should be analyzed.

The framework can be extended to account for the effects of the air pressure as well as the temperature, relaxation and chemical processes in the context of autogenous shrinkage. In addition, different mixtures at different ages will be taken into account for continuous validation of the model, e.g. poromechanical and fracture characterization

as well as additional ring tests.

To further the applicability of the framework to more advanced problems, we intend to carry out the technical task of including an adequate adaptive mesh refinement scheme within the approach. This would reduce the limitations related to the solution with fine, fixed meshes governed by the value of the length scale parameter. Furthermore, the improvement of the solution scheme by using iterative solvers together with a block-formulation with the Schur complement is object of study.

The calibration procedure could be combined with an uncertainty quantification approach dealing with stochastic variation of the material properties.

Potential applications of the developed framework are related to other phenomena in porous media such as wetting, curling, desiccation in thin layers and shear loading (shear bands) as well as dynamic problems. Furthermore, an anisotropic formulation of the fracture energy, plastic behavior (specially in the case of soils and nonlinear elastic laws) as well as different constitutive laws for the description of the effective stress can be implemented and evaluated.

# Appendix A

# Experiments using neutron imaging technique

Cracks can affect the moisture profile during drying. In this appendix, we describe some novel experiments performed using the neutron imaging technique. These aim at observing the temporal evolution of the drying front in a cement mortar with water-to-cement ratio 0.5 and 40% aggregates. Furthermore, results of numerical simulations are compared with the experimental results.

## A.1 Experiments

Several factors such as the drying surface can affect the moisture distribution during drying. The increase of the surface drying area due to e.g. cracking can affect the moisture loss profile. In order to evaluate the effect of the crack on the drying behavior, experimental tests using neutron radiography were performed. The neutron imaging technique allows to follow the water distribution in several material types and has been applied to cement-based materials [164]. Measurements were carried out in two-dimensional configuration, i.e. neutron radiography and in three-dimensional configuration, i.e. neutron tomography. The tests discussed in this work were carried out at the ICON beamline [81] at the Paul Scherrer Institute (PSI), in Villigen, Switzerland.

Prismatic samples with dimensions $15 \times 15 \times 6\text{mm}^3$ with a maturing time of 28 days and made of a cement mortar with water-to-cement-ratio 0.5 and 40% aggregates by volume (same proportions as in Chapter 6) are prepared. Due to the size (thickness) of the specimen, the largest aggregates are of 2 mm size. Four types of specimen are prepared: a reference intact sample and three subsequent types with cuts of different depths, as shown in Fig. A.1. The samples are cut carefully with a diamond saw of 0.4 mm thickness.

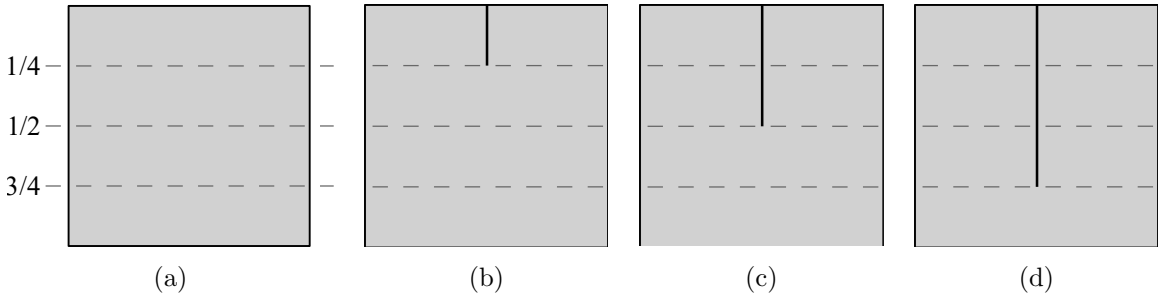


**Figure A.1:** Specimen types: (a) reference intact specimen and specimens with a cut of depth corresponding to (a) one, (b) two and (c) three quarters of the sample height.

Before testing, the samples are sealed with aluminum tape and kept in saturated conditions. Shortly before the test starts, the samples are weighed. Then, they are placed in a small wind tunnel to induce drying during testing. This tunnel is positioned in the beamline and closed. The position of the wind tunnel and the position of each sample is calibrated and the table of the ICON beamline is programmed to shift and hold such that each sample is exposed for 60 seconds to the neutron beam for imaging. The test ends after approximately 13 hours and the weight of the samples is measured again.

The results are postprocessed with the software ImageJ to assess the temporal moisture evolution qualitatively. For conciseness, only part of the obtained results is shown.

The experimental results concerning the half-cut sample are shown in Fig. A.2. In the current qualitative description, darker gray pixels indicate that more water is present, while lighter gray pixels are associated with lower water contents. At the beginning of the test, the sample is practically saturated, Fig. A.2(a). Note that the water content is slightly lower near the upper surface of the sample, at its boundaries and at the edges of the cut. This condition may be related to imperfect sealing. The upper surface dries further and the contribution of the upper half of the cut surface to drying becomes more visible after 135 minutes as shown in Fig. A.2(b). The drying front increases at the cut surfaces as observed at 248 minutes in Fig. A.2(c). The cut surface has dried after 375 minutes, Fig. A.2(d). Note that the upper and lower edges of the sample become more dry within time due to sealing and due to fabrication (cutting). The dried areas become more visible in Figs. A.2(e) and A.2(f).

Additional information is derived from further tests (results not shown), namely:

- The mass loss, computed from the difference between the initial and final mass of the samples, increases with the length of the cut region.
- When the test is repeated with a longer exposure time of 90 seconds to the neutron beam for imaging, the quality of the obtained images is not affected.

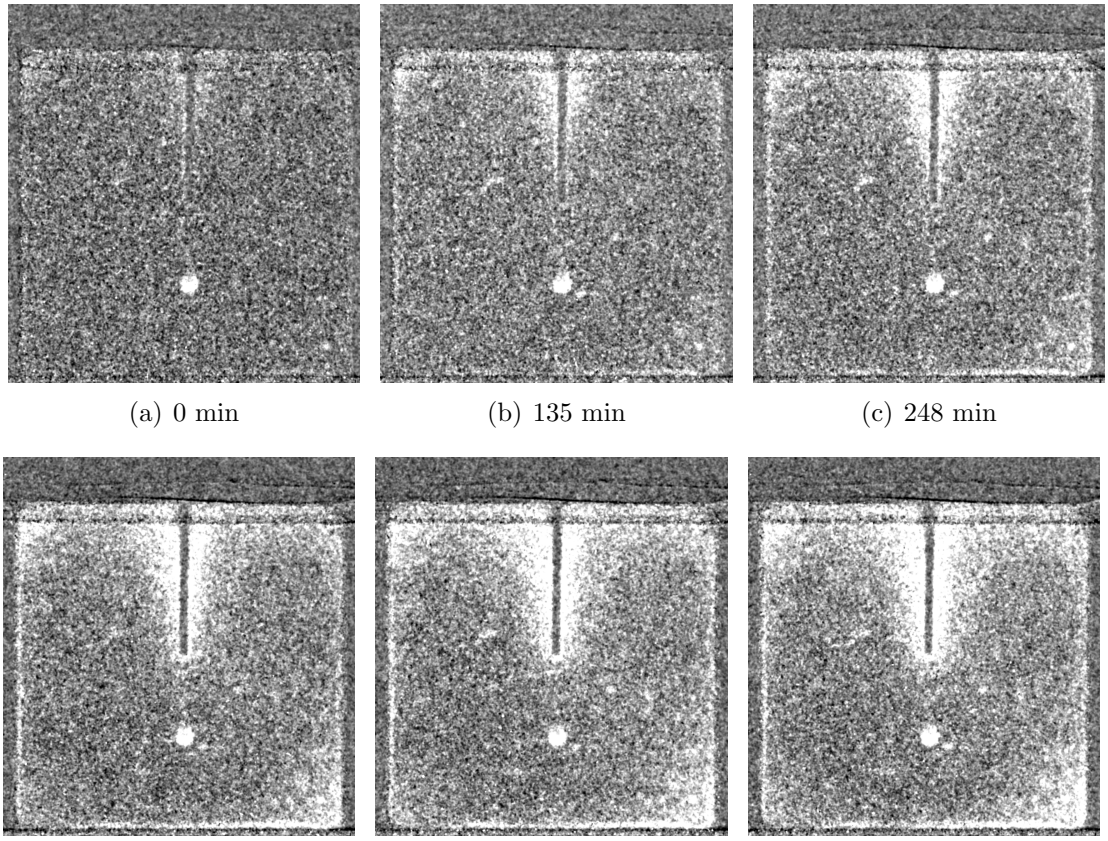

(a) 0 min (b) 135 min (c) 248 min

(d) 375 min (e) 498 min (f) 748 min

**Figure A.2:** Moisture evolution due to drying at different time instants (labels under the figures) up to approximately 13 hours. The lighter pixels indicate lower water content.

## A.2 Simulations

The experimental results indicate that the specimen dries from the outer boundaries as well as from the cut surfaces. The numerical setups in the following aim at assessing the drying front qualitatively. For that, the poromechanical equations disregarding crack evolution are used. The model in study is pure two-dimensional, with dimensions $15 \times 15$ mm$^2$ and half-cut with 0.5 mm width.

Three numerical setups are tested (a) drying from the upper surface, (b) drying from upper surface and internal cut surfaces and (c) drying from upper surface, upper half of lateral surface and internal cut surfaces. In all three configurations, an uniform flux boundary condition is imposed on the drying surfaces, while zero-flux is imposed on the remaining. Furthermore, the sample is fully restrained at the bottom and has zero traction on the remaining surfaces.

The qualitative results of relative humidity, which relates to the water pressure by

means of the Kelvin-Laplace relationship are shown in Fig. A.3. The blue color indicates lower relative humidity, while red stands for higher humidity values. In Fig. A.3(a), a gradual moisture distribution is obtained at the end of the simulation. In Fig. A.3(b), the uniform gradient is re-shaped due to the influence of the cut on the drying process. This result is similar to that shown in Fig. A.2(c). Figure A.3(c) is very similar to the final pattern of the experimental result in Fig. A.2(f).

The last two numerical configurations corroborate the importance to take into account the influence of a crack on the drying behavior. These results motivate future studies regarding the coupling between cracking and moisture variables, i.e. pore water pressure. Furthermore, the results indicate that sealing needs to be improved in future experiments.

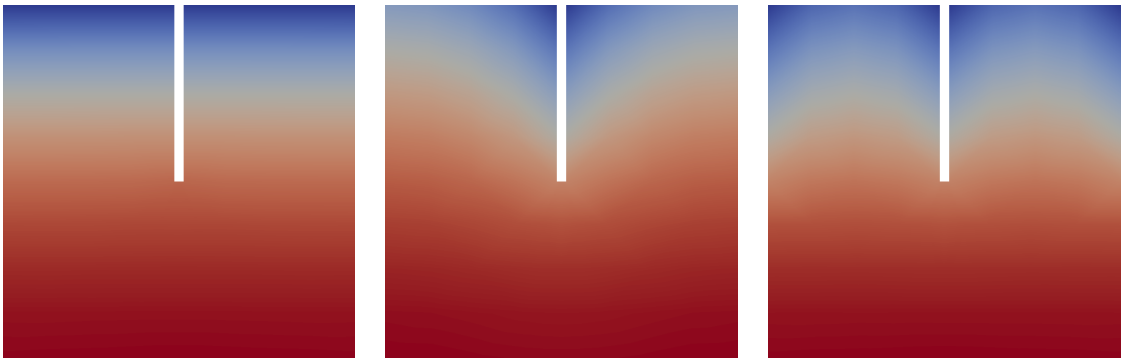

(a) (b) (c)

**Figure A.3:** Relative humidity results of the numerical simulations using the poromechanical equations. The drying flux is applied on (a) upper surface, (b) upper and internal cut surfaces and (c) upper, internal cut surfaces and sides.

## A.3 Summary

In this appendix, experimental tests utilizing neutron imaging radiography are described. Several specimens were tested and for conciseness only the results for the half-cut sample are discussed. The experimental results indicate that the cut surfaces affect the moisture profile.

Simulations of the drying process neglecting and taking into account drying at the cut surfaces are performed. When the drying at the cut surfaces is considered, the numerical results show good agreement with the experimental results. This motivates the study of the coupling between cracking and drying. A further, quantitative postprocessing of the results can provide input data to be used in the modeling of the effect of cracking on the drying process.

# Appendix B

# Linearization

## B.1 Linearization

### B.1.1 Equilibrium equation

The derivatives of the residual of the equilibrium equation, Eq. (4.2.7), with respect to each discretized unknown $\hat{\mathbf{u}}_{n+1}$, $\hat{p}_{w_{n+1}}$ and $\hat{d}_{n+1}$ are reported in the following.

$$\begin{aligned}\frac{\partial R^{uh}}{\partial \hat{\mathbf{u}}_{n+1}} &= -\hat{\mathbf{w}}^{u\,T}\int_{\Omega}\mathbf{B}^{uT} : \left(g(d)\,\mathcal{D}^{+} : \mathbf{B}^{u} - \mathcal{D}^{-} : \mathbf{B}^{u}\right. \\ &\quad +\hat{\mathbf{w}}^{u\,T}\int_{\Gamma_t}\boldsymbol{\phi}^{u}\cdot\frac{\partial\bar{\mathbf{t}}}{\partial\hat{\mathbf{u}}_{n+1}}\,\mathrm{d}\Gamma_t \end{aligned} \tag{B.1.1}$$

$$\begin{aligned}\frac{\partial R^{uh}}{\partial \hat{\mathbf{p}}_{w_{n+1}}} &= -\hat{\mathbf{w}}^{u\,T}\int_{\Omega}\mathbf{B}^{uT} : \left(g(d)\,\frac{\partial\mathcal{D}^{+}}{\partial\hat{\mathbf{p}}_{w_{n+1}}} : \mathbf{B}^{u} + \frac{\partial\mathcal{D}^{-}}{\partial\hat{\mathbf{p}}_{w_{n+1}}} : \mathbf{B}^{u}\right)\mathrm{d}\Omega\,\hat{\mathbf{u}}_{n+1} \\ &\quad +\hat{\mathbf{w}}^{u\,T}\int_{\Omega}\mathbf{B}^{uT} : \left(\alpha\frac{\partial S_w}{\partial\hat{\mathbf{p}}_{w_{n+1}}}\boldsymbol{\phi}^{p\,T}\hat{\mathbf{p}}_{w_{n+1}}\mathbf{I} + \alpha S_w\boldsymbol{\phi}^{p\,T}\mathbf{I}\right)\mathrm{d}\Omega \\ &\quad +\hat{\mathbf{w}}^{u\,T}\int_{\Omega}\boldsymbol{\phi}^{u}\cdot n\frac{\partial S_w}{\partial\hat{\mathbf{p}}_{w_{n+1}}}\rho_w\mathbf{g}\,\mathrm{d}\Omega + \hat{\mathbf{w}}^{u\,T}\int_{\Gamma_t}\boldsymbol{\phi}^{u}\cdot\frac{\partial\bar{\mathbf{t}}}{\partial\hat{\mathbf{p}}_{w_{n+1}}}\,\mathrm{d}\Gamma_t \end{aligned} \tag{B.1.2}$$

$$\begin{aligned}\frac{\partial R^{uh}}{\partial \hat{\mathbf{d}}_{n+1}} &= -\hat{\mathbf{w}}^{u\,T}\int_{\Omega}\mathbf{B}^{uT} : \left(\frac{\partial g(d)}{\partial\hat{\mathbf{d}}_{n+1}}\,\mathcal{D}^{+} : \mathbf{B}^{u}\right)\mathrm{d}\Omega\,\hat{\mathbf{u}}_{n+1} \\ &\quad +\hat{\mathbf{w}}^{u\,T}\int_{\Gamma_t}\boldsymbol{\phi}^{u}\cdot\frac{\partial\bar{\mathbf{t}}}{\partial\hat{\mathbf{d}}_{n+1}}\,\mathrm{d}\Gamma_t \end{aligned} \tag{B.1.3}$$

### B.1.2 Mass balance equation of the pore water

The derivatives of the residual of the mass balance equation of the pore water, Eq. (4.2.8), with respect to each discretized unknown $\hat{\mathbf{u}}_{n+1}$, $\hat{p}_{w_{n+1}}$ and $\hat{d}_{n+1}$ are reported in the following.

$$\frac{\partial R^{ph}}{\partial \hat{\mathbf{u}}_{n+1}} = \hat{\mathbf{w}}^{pT} \int_\Omega \boldsymbol{\phi}^p \, S_w \alpha \frac{\partial \mathrm{tr}(\mathbf{B}^u)}{\partial t} \, \mathrm{d}\Omega \tag{B.1.4}$$

$$\begin{aligned}
\frac{\partial R^{ph}}{\partial \hat{\mathbf{p}}_{w_{n+1}}} = \; & \hat{\mathbf{w}}^{pT} \int_\Omega \mathbf{B}^{pT} \left[ \frac{\partial k_{rw}}{\partial \hat{\mathbf{p}}_{w_{n+1}}} \frac{k_i \mathbf{I}}{\mu_w} (\mathbf{B}^p \, \hat{\mathbf{p}}_w + \rho_w \mathbf{g}) + k_{rw} \frac{k_i \mathbf{I}}{\mu_w} \mathbf{B}^{pT} \right] \mathrm{d}\Omega \\
& + \hat{\mathbf{w}}^{pT} \int_\Omega \mathbf{B}^{pT} \left[ n \frac{\partial S_w}{\partial \hat{\mathbf{p}}_{w_{n+1}}} \frac{1}{K_w} + \frac{\partial C_s}{\partial \hat{\mathbf{p}}_{w_{n+1}}} \right] \boldsymbol{\phi}^{pT} \, \mathrm{d}\Omega \, \frac{\hat{\mathbf{p}}_{w_{n+1}} - \hat{\mathbf{p}}_{w_n}}{\Delta t} \\
& + \hat{\mathbf{w}}^{pT} \int_\Omega \mathbf{B}^{pT} \left[ n \frac{S_w}{K_w} + C_s \right] \boldsymbol{\phi}^{pT} \, \mathrm{d}\Omega \, \frac{1}{\Delta t} \\
& + \hat{\mathbf{w}}^{pT} \int_\Omega \boldsymbol{\phi}^p \, S_w \frac{\alpha - n}{K_s} \left( S_w + \frac{C_s}{n} \boldsymbol{\phi}^p \hat{\mathbf{p}}_{w_{n+1}} \right) \mathrm{d}\Omega \, \frac{1}{\Delta t} \\
& + \hat{\mathbf{w}}^{pT} \int_\Omega \boldsymbol{\phi}^p \, S_w \frac{\alpha - n}{K_s} \left( \frac{\partial S_w}{\partial \hat{\mathbf{p}}_{w_{n+1}}} \right) \boldsymbol{\phi}^{pT} \, \mathrm{d}\Omega \, \frac{\hat{\mathbf{p}}_{w_{n+1}} - \hat{\mathbf{p}}_{w_n}}{\Delta t} \\
& + \hat{\mathbf{w}}^{pT} \int_\Omega \boldsymbol{\phi}^p \, S_w \frac{\alpha - n}{K_s} \left( \frac{\partial C_s}{\partial \hat{\mathbf{p}}_{w_{n+1}}} \frac{1}{n} \boldsymbol{\phi}^p \hat{\mathbf{p}}_{w_{n+1}} + \frac{C_s}{n} \right) \boldsymbol{\phi}^{pT} \, \mathrm{d}\Omega \, \frac{\hat{\mathbf{p}}_{w_{n+1}} - \hat{\mathbf{p}}_{w_n}}{\Delta t} \\
& + \hat{\mathbf{w}}^{pT} \int_\Omega \boldsymbol{\phi}^p \, \frac{\partial S_w}{\partial \hat{\mathbf{p}}_{w_{n+1}}} \frac{\alpha - n}{K_s} \left( S_w + \frac{C_s}{n} \boldsymbol{\phi}^p \hat{\mathbf{p}}_{w_{n+1}} \right) \boldsymbol{\phi}^{pT} \, \mathrm{d}\Omega \, \frac{\hat{\mathbf{p}}_{w_{n+1}} - \hat{\mathbf{p}}_{w_n}}{\Delta t} \\
& + \hat{\mathbf{w}}^{pT} \int_\Omega \boldsymbol{\phi}^p \, S_w (\alpha - n) \frac{\partial K_s^{-1}}{\partial \hat{\mathbf{p}}_{w_{n+1}}} \left( S_w + \frac{C_s}{n} \boldsymbol{\phi}^p \hat{\mathbf{p}}_{w_{n+1}} \right) \boldsymbol{\phi}^{pT} \, \mathrm{d}\Omega \, \frac{\hat{\mathbf{p}}_{w_{n+1}} - \hat{\mathbf{p}}_{w_n}}{\Delta t} \\
& + \hat{\mathbf{w}}^{pT} \int_\Omega \boldsymbol{\phi}^p \, \frac{\partial S_w}{\partial \hat{\mathbf{p}}_{w_{n+1}}} \alpha \frac{\partial \mathrm{tr}(\mathbf{B}^u \hat{\mathbf{u}}_{n+1})}{\partial t} \, \mathrm{d}\Omega \\
& - \hat{\mathbf{w}}^{pT} \int_{\Gamma_q} \frac{\partial \bar{q}}{\partial \hat{\mathbf{p}}_{w_{n+1}}} \mathrm{d}\Gamma_q
\end{aligned} \tag{B.1.5}$$

$$\frac{\partial R^{ph}}{\partial \hat{\mathbf{d}}_{n+1}} = 0 \tag{B.1.6}$$

Note that the elastic constants are also considered in the derivation due to the dependency on the water content. The further necessary numerical treatment of the constitutive relations can be found in Section B.2.

### B.1.3 Phase-field evolution equation

Due to the solution strategy highlighted in Section 4.4, the residual of the phase-field evolution equation, Eq. (4.2.9), is only derived with respect to the crack phase-field.

$$\frac{\partial R^{d^h}}{\partial \hat{\mathbf{d}}_{n+1}} = \hat{\mathbf{w}}^{dT} \int_\Omega \frac{\mathcal{G}_c}{\ell} \left[ \boldsymbol{\phi}^d \boldsymbol{\phi}^{dT} + \ell^2 \mathbf{B}^{dT} \mathbf{B}^d \right] \mathrm{d}\Omega + \hat{\mathbf{w}}^{dT} \int_\Omega \boldsymbol{\phi}^d \boldsymbol{\phi}^{dT} 2\mathcal{H} \, \mathrm{d}\Omega \tag{B.1.7}$$

## B.2 Treatment of constitutive relations

The derivatives of the constitutive relations with respect to the liquid water pressure are needed in the context of variable saturation.

The derivative of the water degree of saturation, $S_w$ given by Eq. (3.3.1), with respect to the water pressure is expressed by

$$\frac{\partial S_w}{\partial p_w} = \frac{\partial S_w}{\partial S_e} \frac{\partial S_e}{\partial \varphi} \frac{\partial \varphi}{\partial p_w}$$

with

$$\frac{\partial S_w}{\partial S_e} = (1 - S_r),$$

$$\frac{\partial S_e}{\partial \varphi} = -m_{vG}(1 + (\alpha_{vG}\,\varphi)^{n_{vG}})^{-m_{vG}-1} n_{vG} (\alpha_{vG}\,\varphi)^{n_{vG}-1} \alpha_{vG}$$

and

$$\frac{\partial \varphi}{\partial p_w} = \frac{-1}{\rho_w g}.$$

The derivative of the relative permeability, $k_{rw}$ from Eq. (3.3.3), with respect to the water pressure is given by

$$\frac{\partial k_{rw}}{\partial p_w} = \frac{\partial k_{rw}}{\partial S_e} \frac{\partial S_e}{\partial \varphi} \frac{\partial \varphi}{\partial p_w}$$

with

$$\frac{\partial k_{rw}}{\partial S_e} = 0.5 S_e^{-0.5} \left( \left( 1 - S_e^{\frac{1}{m_{vG}}} \right)^{m_{vG}} - 1 \right)^2 - 2 S_e^{-0.5+\frac{1}{m_{vG}}} \left( 1 - S_e^{\frac{1}{m_{vG}}} \right)^{m_{vG}-1} \left( \left( 1 - S_e^{\frac{1}{m_{vG}}} \right)^{m_{vG}} - 1 \right).$$

The moisture content $C_s = n\frac{\partial S_w}{\partial p_w}$ is also derived with respect to the water pressure as follows

$$\begin{aligned}\frac{\partial C_s}{\partial p_w} &= n\frac{\partial}{\partial p_w}\left(\frac{\partial S_w}{\partial S_e}\frac{\partial S_e}{\partial \varphi}\frac{\partial \varphi}{\partial p_w}\right) \\ &= n\underbrace{\frac{\partial^2 S_w}{\partial p_w \partial S_e}}_{=0}\frac{\partial S_e}{\partial \varphi}\frac{\partial \varphi}{\partial p_w} + n\frac{\partial S_w}{\partial S_e}\frac{\partial^2 S_e}{\partial p_w \partial \varphi}\frac{\partial \varphi}{\partial p_w} + n\frac{\partial S_w}{\partial S_e}\frac{\partial S_e}{\partial \varphi}\underbrace{\frac{\partial^2 \varphi}{\partial p_w^2}}_{=0}.\end{aligned}$$

For completeness,

$$\frac{\partial^2 S_e}{\partial p_w \partial \varphi} = \frac{\frac{\partial S_e}{\partial \varphi}}{\partial \varphi}\frac{\partial \varphi}{\partial p_w} = \frac{\partial^2 S_e}{\partial \varphi^2}\frac{\partial \varphi}{\partial p_w}$$

with

$$\frac{\partial^2 S_e}{\partial \varphi^2} = \frac{m_{vG} n_{vG} \left(\alpha_{vG}\,\varphi\right)^{n_{vG}} \left(\left(\alpha_{vG}\,\varphi\right)^{n_{vG}} + 1\right)^{-m_{vG}-2} \left(\left(m_{vG} n_{vG} + 1\right)\left(\alpha_{vG}\,\varphi\right)^{n_{vG}} - n_{vG} + 1\right)}{\varphi^2}.$$

Note that if the Young's modulus also depends on the water content $w$, its derivative with respect to the water pressure needs to be computed and is given by

$$\frac{\partial E}{\partial p_w} = \frac{\partial E}{\partial w}\frac{\partial w}{\partial S_w}\frac{\partial S_w}{\partial S_e}\frac{\partial S_e}{\partial \varphi}\frac{\partial \varphi}{\partial p_w}$$

with

$$\frac{\partial w}{\partial S_w} = n\frac{\rho_w}{\rho_d} \times 100.$$

# Appendix C

# Complementary free shrinkage tests

To complement the results from Chapter 6, Section 6.2, the medium and large samples are simulated with $k_i = 5 \times 10^{-22}$ m$^2$. In both sample types, the numerical results overestimate the expected shrinkage.

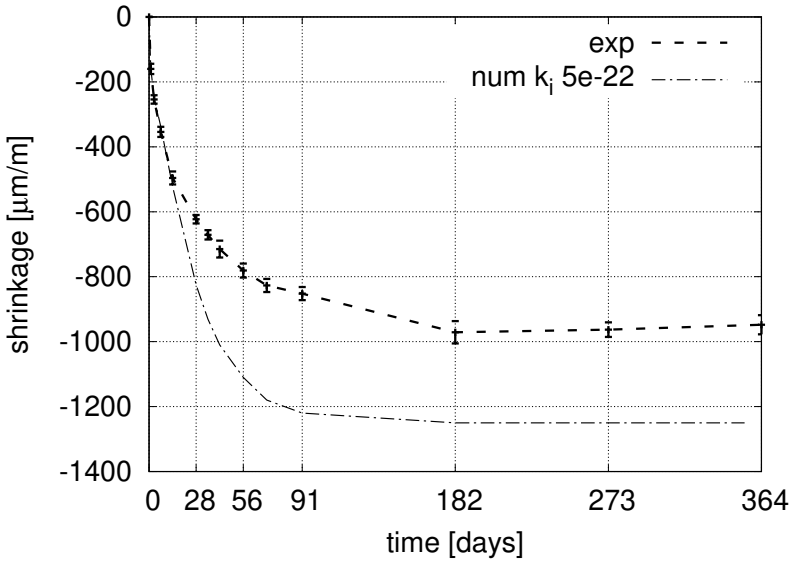


**Figure C.1:** Experimental and numerical shrinkage results of the medium specimen over 1 year.

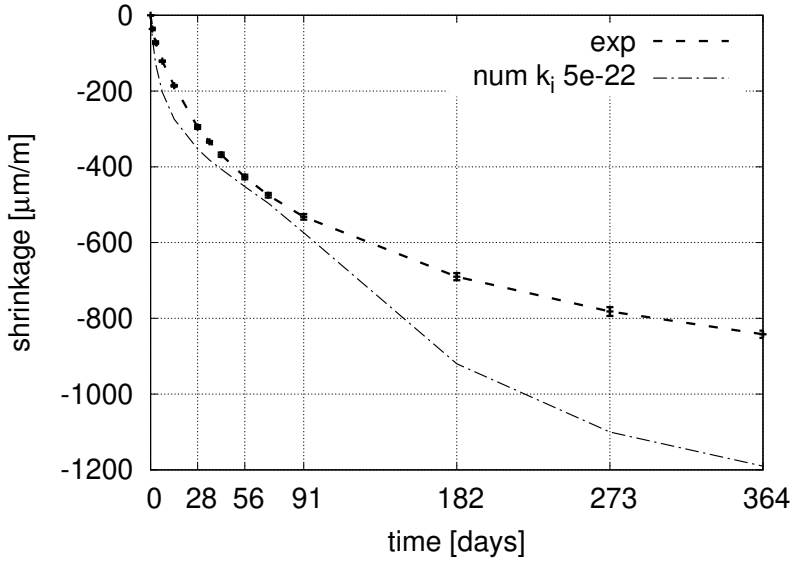


**Figure C.2:** Experimental and numerical shrinkage results of the large specimen over 1 year.

# Bibliography


[1] Betonbau Ergänzende Festlegungen: SIA 262/1(2013) Bauwesen.

[2] C. Alboin, J. Jaffre, J. Robert, and C. Serres. Modeling fractures for flow and transport in porous media. In *Proc. of Joint AMS-IMS-SIAM Summer Research Conference*, 2001.

[3] R. Alessi, M. Ambati, T. Gerasimov, S. Vidoli, and L. De Lorenzis. Comparison of phase-field models of fracture coupled with plasticity. In *Advances in Computational Plasticity*, pages 1–21. Springer, 2018.

[4] R. Alessi, J.-J. Marigo, and S. Vidoli. Gradient damage models coupled with plasticity: variational formulation and main properties. *Mechanics of Materials*, 80:351–367, 2015.

[5] R. Alessi, S. Vidoli, and L. De Lorenzis. A phenomenological approach to fatigue with a variational phase-field model: The one-dimensional case. *Engineering Fracture Mechanics*, 190:53–73, 2018.

[6] M. Ambati and L. De Lorenzis. Phase-field modeling of brittle and ductile fracture in shells with isogeometric nurbs-based solid-shell elements. *Computer Methods in Applied Mechanics and Engineering*, 312:351–373, 2016.

[7] M. Ambati, T. Gerasimov, and L. De Lorenzis. A review on phase-field models of brittle fracture and a new fast hybrid formulation. *Computational Mechanics*, 55:383–405, 2014.

[8] M. Ambati, T. Gerasimov, and L. De Lorenzis. Phase-field modeling of ductile fracture. *Computational Mechanics*, 55(5):1017–1040, 2015.

[9] H. Amor, J.-J. Marigo, and C. Maurini. Regularized formulation of the variational brittle fracture with unilateral contact: Numerical experiments. *Journal of the Mechanics and Physics of Solids*, 2009.

[10] R. Ayada, J.-M. Konrad, and M. Soulié. Desiccation of a sensitive clay: application of the model CRACK. *Canadian Geotechnical Journal*, 34:943–951, 1997.

[11] E. Azinpour, J. Ferreira, M. Parente, and J. Sa. A simple and unified implementation of phase field and gradient damage models. *Advanced Modeling and Simulation in Engineering Sciences*, 5(1):15, 2018.

[12] W. Bangerth, D. Davydov, T. Heister, L. Heltai, G. Kanschat, M. Kronbichler, M. Maier, B. Turcksin, and D. Wells. The `deal.II` library, version 8.4. *Journal of Numerical Mathematics*, 24, 2016.

[13] K.-J. Bathe. *Finite-Elemente-Methoden*, volume 2. Springer Berlin, 2002.

[14] A. Benallal and J.-J. Marigo. Bifurcation and stability issues in gradient theories with softening. *Modelling and Simulation in Materials Science and Engineering*, 15(1):S283, 2006.

[15] A. Bentur and K. Kovler. Evaluation of early age cracking characteristics in cementitious systems. *Materials and Structures*, 36(3):183, 2003.

[16] M. Benzi and A. Wathen. *Some Preconditioning Techniques for Saddle Point Problems*, pages 195–211. Springer Berlin Heidelberg, Berlin, Heidelberg, 2008.

[17] L. Bergamaschi, M. Ferronato, and G. Gambolati. Novel preconditioners for the iterative solution to fe-discretized coupled consolidation equations. *Computer Methods in Applied Mechanics and Engineering*, 196(25):2647 – 2656, 2007.

[18] P. Bernard, N. Moës, and N. Chevaugeon. Damage growth modeling using the thick level set (tls) approach: Efficient discretization for quasi-static loadings. *Computer Methods in Applied Mechanics and Engineering*, 233:11–27, 2012.

[19] A. Bishop. The principle of effective stress. *Norwegian Geotechnical Institute*, 32:1–5, 1960.

[20] A. Bishop and G. Blight. Some aspects of effective stress in saturated and partly saturated soils. *Geotechnique*, 13(3):177–197, 1963.

[21] J. Bisschop. *Drying shrinkage microcracking in cement-based materials*. TU Delft, Delft University of Technology, 2002.

[22] J. Bisschop. Size and boundary effects on desiccation cracking in hardened cement paste. *International Journal of Fracture*, 154(1-2):211–224, 2008.

[23] J. Bisschop and J. van Mier. Effect of aggregates and microcracks on the drying rate of cementitious composites. *Cement and Concrete Research*, 38(10):1190–1196, 2008.

[24] J. Bisschop and F. Wittel. Contraction gradient induced microcracking in hardened cement paste. *Cement and Concrete Composites*, 33(4):466–473, 2011.

[25] J. Bleyer and R. Alessi. Phase-field modeling of anisotropic brittle fracture including several damage mechanisms. *Computer Methods in Applied Mechanics and Engineering*, 336:213–236, 2018.

[26] R. Bloom and A. Bentur. Free and restrained shrinkage of normal and high-strength concretes. *Materials Journal*, 92(2):211–217, 1995.

[27] M. Blunt, B. Bijeljic, H. Dong, O. Gharbi, S. Iglauer, P. Mostaghimi, A. Paluszny, and C. Pentland. Pore-scale imaging and modelling. *Advances in Water Resources*, 51:197 – 216, 2013. 35th Year Anniversary Issue.

[28] M. J. Borden, T. J. Hughes, C. M. Landis, A. Anvari, and I. J. Lee. A phase-field formulation for fracture in ductile materials: Finite deformation balance law derivation, plastic degradation, and stress triaxiality effects. *Computer Methods in Applied Mechanics and Engineering*, 312:130–166, 2016.

[29] M. J. Borden, C. V. Verhoosel, M. A. Scott, T. J. Hughes, and C. M. Landis. A phase-field description of dynamic brittle fracture. *Computer Methods in Applied Mechanics and Engineering*, pages 77–95, 2012.

[30] B. Bourdin. Numerical implementation of the variational formulation for quasi-static brittle fracture. *Interfaces and Free Boundaries*, 9(3):411–430, 2007.

[31] B. Bourdin, G. Francfort, and J.-J. Marigo. Numerical experiments in revisited brittle fracture. *Journal of the Mechanics and Physics of Solids*, 48(4):797–826, 2000.

[32] B. Bourdin, C. Larsen, and C. Richardson. A time-discrete model for dynamic fracture based on crack regularization. *International Journal of Fracture*, 168(2):133–143, 2011.

[33] M. Briffaut, F. Benboudjema, J. Torrenti, and G. Nahas. A thermal active restrained shrinkage ring test to study the early age concrete behaviour of massive structures. *Cement and Concrete Research*, 41(1):56–63, 2011.

[34] H. Bui, G. Nguyen, J. Kodikara, and M. Sanchez. Soil cracking modelling using the mesh-free sph method. In *12th Australia New Zealand Conference on Geomechanics (ANZ 2015)*, 2015.

[35] T. Cajuhi, P. Lura, and L. De Lorenzis. Preliminary calibration of a phase-field model for cracks due to shrinkage in cement-based materials. In *7th GACM Colloquium on Computational Mechanics*, 2017.

[36] T. Cajuhi, L. Sanavia, and L. De Lorenzis. Phase-field modeling of fracture in variably saturated porous media. *Computational Mechanics*, 61(3):299–318, 2018.

[37] T. Cao, E. Milanese, E. Remij, P. Rizzato, J. Remmers, L. Simoni, J. Huyghe, F. Hussain, and B. Schrefler. Interaction between crack tip advancement and fluid flow in fracturing saturated porous media. *Mechanics Research Communications*, 80:24–37, 2017.

[38] N. Castelletto, J. White, and H. Tchelepi. Accuracy and convergence properties of the fixed-stress iterative solution of two-way coupled poromechanics. *International Journal for Numerical and Analytical Methods in Geomechanics*, 39(14):1593–1618, 2015.

[39] E. Cenzon. Coupling a variably saturated porous media model with a phase field model for fracture. Master's thesis, University of Padova, sas, 1 2015.

[40] J. Clayton and J. Knap. Phase field modeling of directional fracture in anisotropic polycrystals. *Computational Materials Science*, 98:158–169, 2015.

[41] O. Coussy. *Poromechanics*. John Wiley & Sons, 2004.

[42] S. Dana, B. Ganis, and M. F. Wheeler. A multiscale fixed stress split iterative scheme for coupled flow and poromechanics in deep subsurface reservoirs. *Journal of Computational Physics*, 352:1–22, 2018.

[43] R. De Boer. *Theory of porous media: highlights in historical development and current state*. Springer Science & Business Media, 2012.

[44] R. de Boer and W. Ehlers. The development of the concept of effective stresses. *Acta Mechanica*, 83(1):77–92, Mar 1990.

[45] R. de Borst and C. Verhoosel. Gradient damage vs phase-field approaches for fracture: Similarities and differences. *Computer Methods in Applied Mechanics and Engineering*, 312:78 – 94, 2016. Phase Field Approaches to Fracture.

[46] L. De Lorenzis, A. McBride, and B. Reddy. Phase-field modelling of fracture in single crystal plasticity. *GAMM-Mitteilungen*, 39(1):7–34, 2016.

[47] J. de S.R. Gago, D. K. O.C., Zienkiewicz, and I. Babuška. A posteriori error analysis and adaptive processes in the finite element method: Part II — Adaptive mesh refinement. *International Journal for Numerical Methods in Engineering*, 19:1621–1656, 1983.

[48] C. Di Bella, A. Michel, H. Stang, and P. Lura. Early age fracture properties of microstructurally-designed mortars. *Cement and Concrete Composites*, 75:62 – 73, 2017.

[49] C. Di Bella, M. Wyrzykowski, and P. Lura. Evaluation of the ultimate drying shrinkage of cement-based mortars with poroelastic models. *Materials and Structures*, 50(1):52, 2017.

[50] Bestimmung des Elastizitätsmoduls unter Druckbelastung(Sekantenmodul):DIN EN 12390-13:2013, 2013.

[51] Prüfverfahren für Zement. Teil 1: Bestimmung der Festigkeit: DIN EN 196-1:2016, 2016.

[52] F. Duda, A. Ciarbonetti, P. Sánchez, and A. Huespe. A phase-field/gradient damage model for brittle fracture in elastic–plastic solids. *International Journal of Plasticity*, 65:269–296, 2015.

[53] W. Ehlers and C. Luo. A phase-field approach embedded in the theory of porous media for the description of dynamic hydraulic fracturing,part ii: The crack-opening indicator. *Computer Methods in Applied Mechanics and Engineering*, 341:429 – 442, 2018.

[54] M. Ferronato, N. Castelletto, and G. Gambolati. A fully coupled 3-d mixed finite element model of biot consolidation. *Journal of Computational Physics*, 229(12):4813 – 4830, 2010.

[55] A. Franceschini, V. Magri, M. Ferronato, and C. Jana. A robust multilevel approximate inverse preconditioner for symmetric positive definite matrices. *SIAM Journal on Matrix Analysis and Applications*, 2018.

[56] G. Francfort and J.-J. Marigo. Revisiting brittle fracture as an energy minimization problem. *Journal of the Mechanics and Physics of Solids*, 46(8):1319–1342, 1998.

[57] F. Freddi and G. Royer-Carfagni. Regularized variational theories of fracture: a unified approach. *Journal of the Mechanics and Physics of Solids*, 58(8):1154–1174, 2010.

[58] D. Gawin, F. Pesavento, and B. Schrefler. Hygro-thermo-chemo-mechanical modelling of concrete at early ages and beyond. part i: hydration and hygro-thermal phenomena. *International Journal for Numerical Methods in Engineering*, 67(3):299–331, 2006.

[59] D. Gawin, F. Pesavento, and B. Schrefler. Hygro-thermo-chemo-mechanical modelling of concrete at early ages and beyond. part ii: shrinkage and creep of concrete. *International Journal for Numerical Methods in Engineering*, 67(3):332–363, 2006.

[60] D. Gawin and L. Sanavia. A unified approach to numerical modeling of fully and partially saturated porous materials by considering air dissolved in water. *Computer Modeling in Engineering and Sciences (CMES)*, 53(3):255, 2009.

[61] D. Gawin and B. Schrefler. Thermo-hydro-mechanical analysis of partially saturated porous materials. *Engineering Computations*, 13(7):113–143, 1996.

[62] P. Gérard, I. Murray, A. Tarantino, and F. Francescon. On the mechanism for desiccation cracks initiation in clayey materials. *Computer Methods and Recent Advances in Geomechanics*, 2014.

[63] T. Gerasimov and L. D. Lorenzis. A line search assisted monolithic approach for phase-field computing of brittle fracture. *Computer Methods in Applied Mechanics and Engineering*, 312:276 – 303, 2016. Phase Field Approaches to Fracture.

[64] T. Gerasimov, E. Stein, and P. Wriggers. Constant-free explicit error estimator with sharp upper error bound property for adaptive fe analysis in elasticity and

fracture. *International Journal for Numerical Methods in Engineering*, 101(2):79–126, 2015.

[65] L. Goehring, A. Nakahara, T. Dutta, S. Tarafdar, and S. Kitsunezaki. *Desiccation cracks and their patterns: Formation and Modelling in Science and Nature*. John Wiley & Sons, 2015.

[66] Z. Grasley and D. Matthew. Viscoelastic properties and drying stress extracted from concrete ring tests. *Cement and Concrete Composites*, 33(2):171–178, 2011.

[67] W. Gray and S. Hassanizadeh. Unsaturated flow theory including interfacial phenomena. *Water Resources Research*, 27(8):1855–1863, 1991.

[68] A. Griffith and M. Eng. Vi. the phenomena of rupture and flow in solids. *Philosophical Transactions of the Royal Society of London A*, 221(582-593):163–198, 1921.

[69] S. Gross and A. Reusken. *Numerical methods for two-phase incompressible flows*, volume 40. Springer Science & Business Media, 2011.

[70] O. Gültekin, H. Dal, and G. Holzapfel. A phase-field approach to model fracture of arterial walls: theory and finite element analysis. *Computer Methods in Applied Mechanics and Engineering*, 312:542–566, 2016.

[71] O. Gültekin, H. Dal, and G. Holzapfel. Numerical aspects of anisotropic failure in soft biological tissues favor energy-based criteria: a rate-dependent anisotropic crack phase-field model. *Computer Methods in Applied Mechanics and Engineering*, 331:23–52, 2018.

[72] Y. Heider and B. Markert. A phase-field modeling approach of hydraulic fracture in saturated porous media. *Mechanics Research Communications*, 2016.

[73] T. Heister and T. Wick. Parallel solution, adaptivity, computational convergence, and open-source code of 2d and 3d pressurized phase-field fracture problems. *PAMM*, 18(1):e201800353, 2018.

[74] S. Hirobe and K. Oguni. Coupling analysis of pattern formation in desiccation cracks. *Computer Methods in Applied Mechanics and Engineering*, 307:470–488, 2016.

[75] M. Hofacker and C. Miehe. A phase field model of dynamic fracture: Robust field updates for the analysis of complex crack patterns. *International Journal for Numerical Methods in Engineering*, 93(3):276–301, 2013.

[76] A. Hossain and J. Weiss. Assessing residual stress development and stress relaxation in restrained concrete ring specimens. *Cement and Concrete Composites*, 26(5):531–540, 2004.

[77] A. Idiart, J. Bisschop, A. Caballero, and P. Lura. A numerical and experimental study of aggregate-induced shrinkage cracking in cementitious composites. *Cement and Concrete Research*, 42(2):272–281, 2012.

[78] O. M. Jensen and P. F. Hansen. Autogenous deformation and rh-change in perspective. *Cement and Concrete Research*, 31(12):1859–1865, 2001.

[79] M. Jirasek. Nonlocal models for damage and fracture: comparison of approaches. *International Journal of Solids and Structures*, 35(31-32):4133–4145, 1998.

[80] C. Jommi, J. Vaunat, A. G. D. Gawin, and B. Schrefler. Multiphase flow in porous media: a numerical benchmark. In *Proceedings of NAFEMS World Congress*, volume 97, pages 1338–1349, 1997.

[81] A. Kaestner, S. Hartmann, G. Kühne, G. Frei, C. Grünzweig, L. Josic, F. Schmid, and E. Lehmann. The icon beamline - a facility for cold neutron imaging at sinq. *Nuclear Instruments and Methods in Physics Research Section A: Accelerators, Spectrometers, Detectors and Associated Equipment*, 659(1):387 – 393, 2011.

[82] J. Kiendl, M. Ambati, L. De Lorenzis, H. Gomez, and A. Reali. Phase-field description of brittle fracture in plates and shells. *Computer Methods in Applied Mechanics and Engineering*, 312:374–394, 2016.

[83] J. Kim, H. Tchelepi, and R. Juanes. Rigorous coupling of geomechanics and multiphase flow with strong capillarity. *SPE journal*, 18(06):1–123, 2013.

[84] J. Kodikara and S. Costa. Desiccation cracking in clayey soils: Mechanisms and modelling. In *Multiphysical Testing of Soils and Shales*, pages 21–32. Springer, 2013.

[85] J. Kodikara, H. Nahlawi, and A. Bouazza. Modelling of curling in desiccating clay. *Canadian Geotechnical Journal*, 41(3):560–566, 2004.

[86] C. Kuhn, T. Noll, and R. Müller. On phase field modeling of ductile fracture. *GAMM-Mitteilungen*, 39(1):35–54, 2016.

[87] M. Lakshmikantha. *Experimental and theoretical Analysis of cracking in drying soils*. PhD thesis, Universitat Politecnica de Catalunia, February 2009.

[88] M. Lakshmikantha, P. Prat, and A. Ledesma. Experimental evidence of size effect in soil cracking. *Canadian Geotechnical Journal*, 49(3):264–284, 2012.

[89] G. Lancioni and G. Royer Carfagni. The variational approach to fracture mechanics. a practical application to the french panthéon in paris. *Journal of Elasticity*, 95(1-2):1–30, 2009.

[90] S. Lee, J. Reber, N. Hayman, and M. Wheeler. Investigation of wing crack formation with a combined phase-field and experimental approach. *Geophysical Research Letters*, 43(15):7946–7952, 2016.

[91] R. Lewis and B. Schrefler. *The finite element method in the static and dynamic deformation and consolidation of porous media*. 1998.

[92] B. Li, C. Peco, D. Millán, I. Arias, and M. Arroyo. Phase-field modeling and simulation of fracture in brittle materials with strongly anisotropic surface energy. *International Journal for Numerical Methods in Engineering*, 102(3-4):711–727, 2015.

[93] A. Liakopoulos. *Transient flow through unsaturated porous media*. PhD thesis, University of California, Berkeley, 1964.

[94] G. Liu, Q. Li, M. Msekh, and Z. Zuo. Abaqus implementation of monolithic and staggered schemes for quasi-static and dynamic fracture phase-field model. *Computational Materials Science*, 121:35–47, 2016.

[95] P. Lura. *Autogenous deformation and internal curing of concrete*. PhD thesis, TU Delft, Delft University of Technology, 2003.

[96] P. Lura. Lecture notes in shrinkage and cracking of concrete: Mechanisms and impact on durability, ethz, 1.11.17, November 2017.

[97] P. Lura, O. M. Jensen, and J. Weiss. Cracking in cement paste induced by autogenous shrinkage. *Materials and Structures*, 42(8):1089–1099, 2009.

[98] V. Magri, A. Franceschini, M. Ferronato, and C. Jana. Multilevel approaches for fsai preconditioning. *Numer Linear Algebra Appl*, 2018.

[99] B. Markert, Y. Heider, and W. Ehlers. Comparison of monolithic and splitting solution schemes for dynamic porous media problems. *International Journal for Numerical Methods in Engineering*, 82(11):1341–1383, 2010.

[100] S. May, J. Vignollet, and R. D. Borst. A numerical assessment of phase-field models for brittle and cohesive fracture: $\gamma$-convergence and stress oscillations. *European Journal of Mechanics-A/Solids*, 52:72–84, 2015.

[101] A. Mesgarnejad, B. Bourdin, and M. Khonsari. A variational approach to the fracture of brittle thin films subject to out-of-plane loading. *Journal of the Mechanics and Physics of Solids*, 61(11):2360–2379, 2013.

[102] C. Miehe, M. Hofacker, L. Schänzel, and F. Aldakheel. Phase field modeling of fracture in multi-physics problems. part ii. coupled brittle-to-ductile failure criteria and crack propagation in thermo-elastic–plastic solids. *Computer Methods in Applied Mechanics and Engineering*, 294:486–522, 2015.

[103] C. Miehe, M. Hofacker, and F. Welschinger. A phase field model for rate-independent crack propagation: Robust algorithmic implementation based on operator splits. *Computer Methods in Applied Mechanics and Engineering*, 199(45):2765–2778, 2010.

[104] C. Miehe, S. Mauthe, and S. Teichtmeister. Minimization principles for the coupled problem of darcy–biot-type fluid transport in porous media linked to phase field modeling of fracture. *Journal of the Mechanics and Physics of Solids*, 82:186–217, 2015.

[105] C. Miehe, F. Welschinger, and M. Hofacker. Thermodynamically consistent phase-field models of fracture: variational principles and multi-field fe implementations. *International Journal for Numerical Methods in Engineering*, 83:1273–1311, 2010.

[106] A. Mikelić, M. Wheeler, and T. Wick. A phase-field method for propagating fluid-filled fractures coupled to a surrounding porous medium. *SIAM Multiscale Modeling and Simulation*, 13(1):367–398, 2014.

[107] A. Mikelić, M. Wheeler, and T. Wick. Phase-field modeling of a fluid-driven fracture in a poroelastic medium. *Computational Geosciences*, pages 1–25, 2015.

[108] A. Mikelić, M. Wheeler, and T. Wick. Phase-field modeling through iterative splitting of hydraulic fractures in a poroelastic medium. *GEM - International Journal on Geomathematics*, 13(1):367–398, 2018.

[109] N. Moës, C. Stolz, P. Bernard, and N. Chevaugeon. A level set based model for damage growth: the thick level set approach. *International Journal for Numerical Methods in Engineering*, 86(3):358–380, 2011.

[110] G. Molnár and A. Gravouil. 2D and 3D abaqus implementation of a robust staggered phase-field solution for modeling brittle fracture. *Finite Elements in Analysis and Design*, 130:27 – 38, 2017.

[111] J. Moon and J. Weiss. Estimating residual stress in the restrained ring test under circumferential drying. *Cement and Concrete Composites*, 28(5):486–496, 2006.

[112] M. Msekh, J. Sargado, M. Jamshidian, P. Areias, and T. Rabczuk. Abaqus implementation of phase-field model for brittle fracture. *Computational Materials Science*, 96:472 – 484, 2015. Special Issue Polymeric Composites.

[113] D. Mumford and J. Shah. Optimal approximations by piecewise smooth functions and associated variational problems. *Communications on Pure and Applied Mathematics*, 42(5):577–685, 1989.

[114] G. Musielak and T. Śliwa. Fracturing of clay during drying: modelling and numerical simulation. *Transport in Porous Media*, 95(2):465–481, 2012.

[115] S. Nagaraja, M. Elhaddad, M. Ambati, S. Kollmannsberger, L. De Lorenzis, and E. Rank. Phase-field modeling of brittle fracture with multi-level hp-fem and the finite cell method. *Computational Mechanics*, pages 1–18, 2017.

[116] T. Nguyen, J. Yvonnet, M. Bornert, C. Chateau, K. Sab, R. Romani, and R. L. Roy. On the choice of parameters in the phase field method for simulating crack initiation with experimental validation. *International Journal of Fracture*, 197(2):213–226, 2016.

[117] T. Nguyen, J. Yvonnet, Q. Zhu, M. Bornert, and C. Chateau. A phase field method to simulate crack nucleation and propagation in strongly heterogeneous materials from direct imaging of their microstructure. *Engineering Fracture Mechanics*, 139:18–39, 2015.

[118] M. Nuth and L. Laloui. Effective stress concept in unsaturated soils: clarification and validation of a unified framework. *International journal for numerical and analytical methods in Geomechanics*, 32(7):771–801, 2008.

[119] K. Park and G. Paulino. Cohesive zone models: a critical review of traction-separation relationships across fracture surfaces. *Applied Mechanics Reviews*, 64(6):060802, 2011.

[120] B. Paul, M. Faivre, P. Massin, R. Giot, D. Colombo, F. Golfier, and A. Martin. 3d coupled HM-XFEM modeling with cohesive zone model and applications to non planar hydraulic fracture propagation and multiple hydraulic fractures interference. *Computer Methods in Applied Mechanics and Engineering*, 342:321 – 353, 2018.

[121] H. Péron. *Desiccation cracking of soils*. PhD thesis, École Polytechnique Fédérale de Lausanne, February 2009.

[122] H. Péron, T. Hueckel, L. Laloui, and L.-B. Hu. Fundamentals of desiccation cracking of fine-grained soils: experimental characterisation and mechanisms identification. *Canadian Geotechnical Journal*, 46(10):1177–1201, 2009.

[123] H. Peron, L. Laloui, L.-B. Hu, and T. Hueckel. Formation of drying crack patterns in soils: a deterministic approach. *Acta Geotechnica*, 8(2):215–221, 2013.

[124] F. Pesavento, D. Gawin, M. Wyrzykowski, B. Schrefler, and L. Simoni. Modeling alkali–silica reaction in non-isothermal, partially saturated cement based materials. *Computer Methods in Applied Mechanics and Engineering*, 225:95–115, 2012.

[125] K. Pham, H. Amor, J.-J. Marigo, and C. Maurini. Gradient damage models and their use to approximate brittle fracture. *International Journal of Damage Mechanics*, 20(4):618–652, 2011.

[126] R. Pignatelli. *Modeling of degradation induced by alkali-silica reaction in concrete structures*. PhD thesis, Italy, 2012.

[127] U. Pillai, Y. Heider, and B. Markert. A diffusive dynamic brittle fracture model for heterogeneous solids and porous materials with implementation using a user-element subroutine. *Computational Materials Science*, 153:36 – 47, 2018.

[128] P. Prat, A. Ledesma, and L. Cabeza. Drying and cracking of soils: numerical modeling. *Numerical Models in Geomechanics*, 2002.

[129] A. Raina and C. Miehe. A phase-field model for fracture in biological tissues. *Biomechanics and Modeling in Mechanobiology*, 15(3):479–496, 2016.

[130] E. Remij, J. Remmers, J. Huyghe, and D. Smeulders. An investigation of the step-wise propagation of a mode-ii fracture in a poroelastic medium. *Mechanics Research Communications*, 80:10–15, 2017.

[131] L. Sanavia, F. Pesavento, and B. Schrefler. Finite element analysis of non-isothermal multiphase geomaterials with application to strain localization simulation. *Computational Mechanics*, 37(4):331–348, 2006.

[132] D. Santillán, R. Juanes, and L. Cueto-Felgueroso. Phase field model of hydraulic fracturing in poroelastic media: Fracture propagation, arrest, and branching under fluid injection and extraction. *Journal of Geophysical Research: Solid Earth*, 2018.

[133] J. Schlitter, A. Senter, D. Bentz, T. Nantung, and W. Weiss. A dual concentric ring test for evaluating residual stress development due to restrained volume change. *Journal of ASTM international*, 2010.

[134] A. Schlüter, A. Willenbücher, C. Kuhn, and R. Müller. Phase-field approximation of dynamic brittle fracture. *Computational Mechanics*, 54(5):1141–1161, 2014.

[135] B. Schrefler. *The finite element method in soil consolidation (with applications to surface subsidence)*. PhD thesis, University College of Swansea, 1984.

[136] B. Schrefler, L. Sanavia, and C. Majorana. A multiphase medium model for localisation and postlocalisation simulation in geomaterials. *Mechanics of Cohesive-frictional Materials*, 1(1):95–114, 1996.

[137] K. Seki. SWRC fit–a nonlinear fitting program with a water retention curve for soils having unimodal and bimodal pore structure. *Hydrology and Earth System Sciences Discussions*, 4(1):407–437, 2007.

[138] Y. Shen, M. Mollaali, Y. Li, W. Ma, and J. Jiang. Implementation details for the phase field approaches to fracture. *Journal of Shanghai Jiaotong University (Science)*, 2018.

[139] N. Shokri, P. Zhou, and A. Keshmiri. Patterns of desiccation cracks in saline bentonite layers. *Transport in Porous Media*, 110(2):333–344, 2015.

[140] L. Simoni and B. Schrefler. Multi-field simulation of fracture. *Advances in Applied Mechanics*, 47(C):367–519, 2014.

[141] J. Skoček and H. Stang. Inverse analysis of the wedge-splitting test. *Engineering Fracture Mechanics*, 75(10):3173 – 3188, 2008.

[142] R. Stirling, C. Davie, and S. Glendinning. Multiphase modelling of desiccation cracking in the near-surface of compacted soils. In *Proc. of the 16 th Europ. Conf. on Soil Mechanics and Geotechnical Engineering.–Edinburgh*, pages 2311–2316, 2015.

[143] R. Stirling, D. Simpson, and C. Davie. The application of digital image correlation to brazilian testing of sandstone. *International Journal of Rock Mechanics and Mining Sciences*, 60:1–11, 2013.

[144] R. A. Stirling. *Multiphase modelling of desiccation cracking in compacted Soil*. PhD thesis, Newcastle University, May 2014.

[145] M. Strobl and T. Seelig. A novel treatment of crack boundary conditions in phase field models of fracture. *PAMM*, 15(1):155–156, 2015.

[146] M. Strobl and T. Seelig. On constitutive assumptions in phase field approaches to brittle fracture. *Procedia Structural Integrity*, 2:3705–3712, 2016.

[147] S. Teichtmeister, D. Kienle, F. Aldakheel, and M. Keip. Phase field modeling of fracture in anisotropic brittle solids. *International Journal of Non-Linear Mechanics*, 97:1–21, 2017.

[148] K. Terzaghi. *Erdbaumechanik auf Bodenphysikalischer Grundlage*. Franz Deuticke, Liepzig-Vienna, 1925.

[149] H. Trabelsi, M. Jamei, H. Zenzri, and S. Olivella. Crack patterns in clayey soils: experiments and modeling. *International Journal for Numerical and Analytical Methods in Geomechanics*, 36:1410–1433, 2012.

[150] N. Tritsch, D. Darwin, and J. Browning. Evaluating shrinkage and cracking behavior of concrete using restrained ring and free shrinkage tests. Technical report, University of Kansas Center for Research, Inc., 2005.

[151] C. van Duijn, A. Mikelic, and T. Wick. A monolithic phase-field model of a fluid-driven fracture in a nonlinear poroelastic medium. *Mathematics and Mechanics of Solids*, page 1081286518801050, 2018.

[152] M. van Genuchten. A closed-form equation for predicting the hydraulic conductivity of unsaturated soils. *Soil Science Society*, 44:892–898, 1980.

[153] C. Verhoosel and R. Borst. A phase-field model for cohesive fracture. *International Journal for Numerical Methods in Engineering*, 96(1):43–62, 2013.

[154] J. Weiss, W. Yang, and S. Shah. Influence of specimen size/geometry on shrinkage cracking of rings. *Journal of Engineering Mechanics*, 126(1):93–101, 2000.

[155] W. Weiss, W. Yang, and S. Shah. Shrinkage cracking of restrained concrete slabs. *Journal of Engineering Mechanics*, 124(7):765–774, 1998.

[156] J. White and R. Borja. Block-preconditioned newton–krylov solvers for fully coupled flow and geomechanics. *Computational Geosciences*, 15(4):647, Apr 2011.

[157] J. White, N. Castelletto, and H. Tchelepi. Block-partitioned solvers for coupled poromechanics: A unified framework. *Computer Methods in Applied Mechanics and Engineering*, 303:55 – 74, 2016.

[158] T. Wu, A. Carpiuc-Prisacari, M. Poncelet, and L. De Lorenzis. Phase-field simulation of interactive mixed-mode fracture tests on cement mortar with full-field displacement boundary conditions. *Engineering Fracture Mechanics*, 2017.

[159] T. Wu and L. De Lorenzis. A phase-field approach to fracture coupled with diffusion. *Computer Methods in Applied Mechanics and Engineering*, 312:196–223, 2016.

[160] M. Wyrzykowski, C. Di Bella, and P. Lura. Prediction of drying shrinkage of cement-based mortars with poroelastic approaches: a critical review. In *Poromechanics VI*, pages 579–586. 2017.

[161] M. Wyrzykowski, P. Lura, F. Pesavento, and D. Gawin. Modeling of internal curing in maturing mortar. *Cement and Concrete Research*, 41(12):1349–1356, 2011.

[162] X. Yang, Y. Mehmani, W. Perkins, A. Pasquali, M. Schonherr, K. Kim, M. Perego, M. Parks, N. Trask, M. Balhoff, M. Richmond, M. Geier, M. Krafczyk, L.-S. Luo, A. Tartakovsky, and T. Scheibe. Intercomparison of 3d pore-scale flow and solute transport simulation methods. *Advances in Water Resources*, September 2015.

[163] K. Yoshioka and B. Bourdin. A variational hydraulic fracturing model coupled to a reservoir simulator. *International Journal of Rock Mechanics and Mining Sciences*, 88:137 – 150, 2016.

[164] P. Zhang, F. Wittmann, P. Lura, S. Müller, and S. Han. Application of neutron imaging to investigate fundamental aspects of durability of cement-based-materials: a review. *Cement and Concrete Research*, 108:152–166, 2018.

[165] S. Zhou, T. Rabczuk, and X. Zhuang. Phase field modeling of quasi-static and dynamic crack propagation:COMSOL implementation and case studies. *Advances in Engineering Software*, 122:31–49, 2018.

[166] S. Zhou, X. Zhuang, and T. Rabczuk. A phase-field modeling approach of fracture propagation in poroelastic media. *Engineering Geology*, 2018.

[167] X. Zhou, W. Dong, and O. Oladiran. Assessment of restrained shrinkage cracking of concrete using elliptical ring specimens: experimental and numerical. *Journal of Materials in Civil Engineering*, 26(11), 2014.

[168] O. Zienkiewicz, A. Chan, M. Pastor, B. Schrefler, and T. Shiomi. *Computational geomechanics - with special reference to earthquake engineering.* John Wiley & Sons, 1999.